

Ultracold $^{23}\text{Na}^6\text{Li}$ Molecules in the Triplet Ground State

by

Timur Michael Rvachov

B.A.Sc., University of Toronto (2010)

Submitted to the Department of Physics
in partial fulfillment of the requirements for the degree of
Doctor of Philosophy

at the

MASSACHUSETTS INSTITUTE OF TECHNOLOGY

June 2018

© Massachusetts Institute of Technology 2018. All rights reserved.

Author
Department of Physics
February 9, 2018

Certified by
Wolfgang Ketterle
John D. MacArthur Professor of Physics
Thesis Supervisor

Accepted by
Scott A. Hughes
Professor of Physics
Interim Associate Department Head

Ultracold $^{23}\text{Na}^6\text{Li}$ Molecules in the Triplet Ground State

by

Timur Michael Rvachov

Submitted to the Department of Physics
on February 9, 2018, in partial fulfillment of the
requirements for the degree of
Doctor of Philosophy

Abstract

This thesis describes experiments in spectroscopy and formation of triplet $^{23}\text{Na}^6\text{Li}$ molecules from an initial mixture of ultracold ^{23}Na and ^6Li . The production of quantum degenerate molecules with long-range dipolar interactions is a long-standing goal in low temperature physics. NaLi is a fermionic molecule with an electric dipole moment of 0.2 Debye and a magnetic dipole moment of $2 \mu_B$ in its triplet ro-vibrational ground state. The formation of an ultracold molecule with both electric and magnetic dipole moments allows for novel opportunities in control of ultracold molecular reactions and studies of quantum many-body systems with dipolar interactions.

This experimental work consists of two parts. The first is a thorough spectroscopic study of the excited and ground triplet potentials of NaLi using one- and two-photon photoassociation spectroscopy. We present the spectroscopic positions and strengths of transitions to nearly all vibrational states in the excited $c^3\Sigma^+$ and ground $a^3\Sigma^+$ potentials of NaLi. This is the first spectroscopic observation of triplet potentials in NaLi and the first demonstration of photoassociation in the Na-Li system.

The second part utilizes our spectroscopic results to coherently form an ultracold gas of NaLi molecules. Starting with an ultracold Na-Li mixture, we use magneto-association to form weakly bound Feshbach molecules. The Feshbach molecules are then transferred to the ro-vibrational triplet ground state using a two-photon stimulated Raman adiabatic passage (STIRAP) technique, forming 3×10^4 molecules at a density of $5 \times 10^{10} \text{ cm}^{-3}$ and temperature of $3 \mu\text{K}$. The molecules are long-lived with a measured lifetime of 5 seconds, which highlights their fermionic nature and low universal inelastic loss rate. The utility of the molecule's magnetic moment is demonstrated by performing electron spin resonance spectroscopy to measure the hyperfine structure of the molecule.

Thesis Supervisor: Wolfgang Ketterle
Title: John D. MacArthur Professor of Physics

To my family

Acknowledgments

It is impossible to adequately express in writing my gratitude to those who have supported me during my PhD. My MIT experience has at times pushed me to my intellectual, physical, and emotional limits, which I would not have been able to overcome alone. Looking back, I can remember moments of joy and moments of pain, all of them encased in an enormous wreath of personal growth.

Prof. Wolfgang Ketterle, thank you for your mentorship. I came to MIT wholly unaware of what it takes to be an experimental physicist, and I leave with an understanding and deep-rooted respect for scientific progress. I thank you not only for your lessons in physics, but also for your great patience that has allowed me to learn lessons that can not be taught with words, but only with experience. With you, I have learned how to face failure, fall down, get back up, and to repeat this process as many times as necessary. Your ability to simply connect ideas as a physicist and your stalwart personality have set an example I will continue to follow.

Prof. Martin Zwierlein, thank you for dealing with my playful nature in a positive manner and always encouraging me to grab physics by the horns. Discussions with you have always left me inspired.

I would like to thank the BEC3 team, both past and present. You have been with me nearly every working day, and each of you has personally shaped my growth as a scientist. Caleb Christensen, Ye-Ryoung Lee, Jae-Hoon Choi (Go Michigan!), Myoung-Sun Heo and Tout Wang—your welcoming guidance during my early years in graduate school put me in a position to succeed. Dylan Cotta, thank you for giving me, Tout, and Colin Kennedy a warm welcome to Los Angeles during my first trip to DAMOP. Derek Kita, Chenchen Luo, Yijun Jiang and Li Jing—thank you for your agency in repairing the ever-evolving machine and plugging the holes whenever there were leaks, both physically and metaphorically. I want to particularly thank Pascal Notz for his friendship during a difficult year in BEC3 when the oven chamber had a “meltdown”. It was an experimentally frustrating period filled with setbacks and repairs, and I do not know how we would have managed without your tireless work

ethic and optimism.

Of the more recent team members, I would like to thank Hyungmok Son, Sepehr Ebadi, Juliana Park, Ariel Sommer, and Alan Jamison. This thesis would be two chapters shorter were it not for your hard work and support. Sepehr, thank you not only for building lasers, but for coming to our group with an alacrity and energy that made working with you an absolute pleasure. Hyungmok, countless times I have relied on your companionship as we ran the experiment into the early morning. Many nights would have ended short of success without your persistence. Alan, you've been on the journey from the first signal of photoassociation to the last click of the "Submit" button. You've ignited a flame of progress in BEC3 which has lit the way for our success. Julie, thank you for asking me questions, because as tired as I looked all the time I actually really enjoyed the conversation. And Ariel, thank for coming back to make sure I was okay. I am grateful to all of BEC3 for your friendship and support.

I would like to thank the Ketterle and Zwierlein groups, the entire 2nd floor of building 26 and the greater MIT-Harvard CUA community. You have provided a warm environment for scientific and personal growth. Aviv Keshet, thank you for welcoming me to the Cicero club, an influence that cannot be understated given my immediate future in the tech industry. Will Lunden and Li Du, thank you for joining the Cicero club. Tarik Yefsah and Julian Struck, thank you for keeping the curtain border more loving and less aggressive than it could have been. Peter Park and Sebastian Will, thank you for letting us copy your experiment. Colin Kennedy, Cody Burton, Woo Chang Chung and Wenlan Chen, thank you for letting us steal near-IR optics and a 1319 nm laser. Junru Li, Boris Shteynas, Furkan Top, and Chris Lee, thank you for letting us steal everything else. Boris, somehow you and I would always find each other in the hallway at 3am; I'm not sure why I'm thankful for this, but I am. My Canadian brothers, Alexei Bylinskii, Dorian Gangloff and Boris Braverman, thank you for helping me navigate US tax regulations (oh and Boris thanks for the op-amps too). I would like to thank Lee Liu, Alex Lukin, Prof. John Doyle and Prof. Mikhail Lukin for organizing and participating in various kinds of chaos during the CUA retreats.

I want to thank my classmates, with whom I started the ultracold atoms journey, Ivana Dimitrova, Jesse Amato-Grill, and Lawrence Cheuk. From studying for the qualifying exams, late nights in the hallway, to lab-skipping ski trips and more, we have compassionately shared struggles and successes since day one.

Though at times there was heavy lifting to do in the lab, my physical limit was truly pushed while playing with the MIT Men's Club Hockey Team. I thank all of the team members past and present for an unforgettable experience both as athletes and as friends. The coaches—Dave Hunter, Brad Holschuh, Tom Hopkins, and Nick Sisler—thanks for sticking with me while I stared at my feet and ate it at the red line. MIT Hockey has had such a positive impact on me both on and off the ice that it is difficult for me to imagine who I would be without it.

I have been fortunate to have made great new friends at MIT, and to be supported by many old ones. I would like to thank Andy and Dave Pritchard not only for the sailing in Rhode Island, but even more so for your caring and guidance. Your concise and honest advice was like a lighthouse in the darkness. Maddy Aby, thank you for the adventures in the snow and the sea. Jannik Beusse, thank you for at times literally carrying me. Phil Russ, Sean Yamana, and Mladen Cricic: we have known one another since highschool, but no matter how long we are apart I find we still understand each other just the same.

I would like to especially thank my two best friends, Niklas Jepsen and Nikolay Perunov. Russian Nick—from Tang Hall to Baystate Road to NYC—through the good times and the bad your honesty and goodwill were always appreciated. I want to thank the entire Jepsen family: Niki, Maui, Karin, and Søren. You have welcomed me into your family with warmth and love. Thank you for the adventures and the uplifting pull so many times when I needed it most.

This thesis is dedicated to my family: my two brothers, Alesha and Marat, and my parents, Lila and Misha. I was born in Vinnitsa, Ukraine, and I find myself now graduating with a PhD from MIT. You have worked and sacrificed to give me every opportunity to succeed. Thank you for your love and support.

Contents

1	Introduction	14
1.1	Interacting atoms and molecules at absolute zero	16
1.2	Production of cold molecules	20
1.3	NaLi and the bi-alkali landscape	24
1.4	Thesis outline	29
2	Experimental apparatus	32
2.1	Ultracold Na, Li mixture experiment overview	33
2.1.1	Cold atom production	33
2.1.2	Imaging	36
2.1.3	Stability	37
2.2	Oven and gate valve replacement	38
2.2.1	Background	38
2.2.2	Improved oven and cleaning procedure	40
2.3	Magnetic field stabilization	43
2.3.1	Background: do we need active stabilization?	43
2.3.2	Stabilization circuit	45
2.3.3	Feshbach molecule sweep coil	49
2.4	Laser systems for NaLi molecules	50
2.4.1	Spectroscopy lasers	50
2.4.2	STIRAP lasers	52
2.5	Future improvements	57

3 Photoassociation spectroscopy	58
3.1 Experimental approach	59
3.2 Finding a first signal	63
3.3 Spectroscopic line positions	66
3.3.1 $v^* = 11$ fine structure	70
3.4 Line strengths	73
4 Two-photon spectroscopy	77
4.1 Experimental approach	78
4.2 Choosing a pathway to the ground state	82
4.3 Dark-resonance spectra: line positions	84
4.3.1 Rotational splittings	87
4.4 Line strengths	89
4.4.1 Autler-Townes spectra	89
4.4.2 Dark-resonance lineshapes	91
4.5 Alternative paths to the triplet ground state	94
4.5.1 Pumping	94
4.5.2 Free-to-bound STIRAP	96
5 Formation of triplet ground state molecules	100
5.1 Experimental approach	101
5.2 Feshbach molecules revisited	103
5.3 Molecular spectroscopy at high magnetic fields	107
5.4 STIRAP transfer to the ro-vibrational ground state	112
5.5 Studies of ultracold NaLi triplet ground state molecules	118
5.5.1 Lifetime and trapping	118
5.5.2 Estimating the loss coefficient	122
5.5.3 Electron spin resonance spectroscopy	127
6 Summary and outlook	131
6.1 Collisional studies	131

6.2	Simplifying experiments	133
6.3	Concluding remarks	135
A	Magnetic field stability circuit calibration	137
B	Dispersion coefficients for Na, Li, and the NaLi molecule	142
C	Triplet <i>ab initio</i> potentials	143

List of Figures

1-1	NaLi molecular potential overview	22
1-2	Dipole moments and universal loss rates for triplet heteronuclear bi-alkali dimers	28
2-1	Ultracold atoms machine diagram	34
2-2	Hyperfine states of Na and Li in a magnetic field	35
2-3	Histogram of most common times to take experimental data	39
2-4	Improved oven design	41
2-5	Cleaning the oven skimmer	42
2-6	Feshbach coil current stabilization circuit	46
2-7	Feshbach field noise measurement at 750 G	48
2-8	Diagram of the STIRAP laser setup	54
2-9	Beatnote linewidth of STIRAP lasers	56
3-1	Photoassociation to NaLi triplet molecular potentials	62
3-2	First observation of photoassociation	64
3-3	Leroy-Bernstein expansion predictions	65
3-4	A sample PA spectrum of the $v^* = 11$ excited vibrational state	67
3-5	PA line structure in the $c^3\Sigma^+$ potential	69
3-6	Polarization dependent PA of the $v^* = 11$ state	70
3-7	Comparison of electronic structures in NaLi and O ₂	72
3-8	$v^* = 11$ PA line strength	74
3-9	PA line strengths for all observed vibrational states	75

4-1	Molecular potential energy level diagram for two-photon spectroscopy	79
4-2	Simulated dark-resonance and Autler-Townes spectra	81
4-3	Franck-Condon factors for optimal STIRAP transfer	83
4-4	Sample dark-resonance spectra	84
4-5	Comparison of $a^3\Sigma^+$ vibrational binding energies to theoretical calculations	86
4-6	Dark-resonance spectrum of rotationally excited NaLi ground state molecules	88
4-7	Autler-Townes spectrum of the ro-vibrational ground state	89
4-8	Bound-to-bound line strengths between vibrational states in $a^3\Sigma^+$ and $c^3\Sigma^+$	93
4-9	Free-to-bound electromagnetically induced transparency	98
5-1	Molecular potentials and transitions for formation of NaLi triplet ground state molecules	101
5-2	Optical dipole trap geometry at high magnetic fields	102
5-3	Feshbach molecule formation and lifetime	104
5-4	Centrifugal distortion of the Feshbach molecule wavefunction	106
5-5	Zeeman splitting of the $c^3\Sigma^+$, $v^* = 11$ excited molecular state	108
5-6	Transition diagram between the Feshbach state ($a^3\Sigma^+$, $v_g = 10$) and intermediate excited state ($c^3\Sigma^+$, $v_g = 11$) at high magnetic fields.	109
5-7	Upleg transition spectroscopy at 745 G	110
5-8	Two-photon spectroscopy using Feshbach molecules	111
5-9	STIRAP from Feshbach molecules to the ro-vibrational ground state .	114
5-10	STIRAP efficiency as a function of pulse duration	115
5-11	Imaging molecules	117
5-12	Initial measurements of the NaLi ground state lifetime	119
5-13	NaLi triplet ground state molecule formation sequence with thorough free atom clean-out	120

5-14 Franck-Condon factors for optical excitations to the $b^3\Pi$ potential of the NaLi molecule	121
5-15 Long lifetime in a pure sample of isolated NaLi triplet ground state molecules	122
5-16 Parametric modulation of the 1319 nm ODT to determine molecular trap frequencies	123
5-17 Time-of-flight distributions of dissociated molecules	124
5-18 Loss coefficients in NaLi collisions	127
5-19 Electron spin resonance spectroscopy of the NaLi molecules	129
5-20 Hyperfine structure and transitions in the NaLi triplet ground state molecule	130
A-1 Modulation bandwidth of series IGBT vs. parallel transistor	138
A-2 Magnetic field stabilization test using injected noise	139
A-3 Hall probe noise performance	140
A-4 Fluxgate magnetometer noise performance	141

List of Tables

1.1	Comparison of ultracold atomic and condensed matter systems	17
1.2	Experimental efforts to produce dipolar bi-alkali molecules	27
2.1	Lasers used for manipulation of NaLi molecules	51
4.1	NaLi $a^3\Sigma^+$ vibrational state binding energies	85
4.2	Comparison of Feshbach resonances to PA	96
B.1	Properties of the NaLi singlet and triplet ro-vibrational ground states	142
C.1	Table of <i>ab initio</i> potential values for the lowest three triplet potentials of NaLi	143

Chapter 1

Introduction

The field of low temperature physics is filled with striking discoveries and unexpected applications. In 1877, physicists Louis Paul Cailletet of France and Raoul Pictet of Switzerland independently produced oxygen in its liquid state [1]. At the time, oxygen was among the “permanent gases”¹, a group of substances which were believed to never exist in a liquid or solid state. Cailletet’s experiment used a highly pressurized chamber of gaseous oxygen that was allowed to rapidly expand to a large volume. This resulted a momentary temperature drop to approximately -200 °C (70 K), and the observation of a visible, liquid mist of oxygen². The following decades produced a flurry of scientific accomplishments, including the discovery of the noble gases, and punctuated by the liquefaction of Helium by the Dutch physicist Heike Kamerlingh Onnes in 1908. Onnes’ experiments produced liquid Helium at record low temperatures of 1.5 K, and marked the beginning of Helium as an industry standard of cryogenic cooling. Only three years later, Onnes would use Helium as a coolant to lower the temperature of Mercury metal below 4.2 K, at which point its electrical resistance was measured to rapidly drop to zero. This was the first observation of superconductivity (or, the superfluidity of the conducting electrons), which would become one of the focal points in modern physics, with mysteries extending to present

¹Including hydrogen, carbon monoxide, methane, and nitric oxide. The noble gases were not yet discovered.

²Pictet’s experiment used an entirely different method of producing liquid oxygen at high (300 atm) pressures [1].

day research [2]. Ironically, Onnes' prior experiments already produced the liquid Helium itself in a superfluid state, though this would go largely unnoticed for two more decades [3].

As time would tell, these discoveries of low temperature physics had enormous impact in both science and engineering. For example, liquid oxygen (or LOX as it's known in the aerospace industry) is a common oxidizer in space-going rockets. Superconductivity is employed in almost every magnetic resonance imaging (MRI) machine, where Niobium-Titanium³ coils are used to produce large magnetic fields of ~ 3 Tesla. In the scientific community, the aforementioned discoveries at the turn of the 20th century sparked an experimental race to absolute zero. Could zero kelvin be reached? What new material properties would one find at absolute zero? In 1995, a team of scientists from the University of Colorado and MIT achieved temperatures below $1 \mu\text{K}$ in dilute vapors of alkali atoms [4, 5], effectively reaching absolute zero⁴. These atoms exhibited superfluidity, similar to the low temperature effects in the electrons of Mercury and liquid Helium but with significantly smaller energy scales. These atomic systems birthed the new field of ultracold physics and "quantum simulation", which will be described in more detail shortly.

The formation of ultracold alkali gases at absolute zero was a momentous scientific achievement, but it was not without its limitations. The techniques used to produce these gases—laser cooling and evaporation (described in Chapter 2)—were very material specific. It was possible to create millions of alkali atoms at nanokelvin temperatures and densities of $\sim 10^{13} \text{ atoms/cm}^3$, but not much else (compare these numbers with a day-to-day example: a milliliter of water, which contains 10^{22} molecules at a density $10^{21} \text{ molecules/cm}^3$). Cooling anything else to these temperatures was a significant challenge, if not impossible. For example, the oxygen molecule (O_2), which played such a crucial role in the field of low temperature physics, currently cannot be cooled to the nanokelvin regime due to the limitations of laser cooling. Nonetheless,

³Niobium-Titanium is a commonly used superconductor in industrial applications which is superconducting below 10 K.

⁴While technically the temperature $T = 1 \mu\text{K}$ is still above zero, it was below any other relevant temperature scales in the system, thus the atoms behaved as if $T = 0$.

the success of ultracold atoms experiments has intrigued scientists to continue the pursuit of the ultracold temperatures with other (non-alkali) atoms and molecules.

The work of this thesis describes the formation of ultracold NaLi molecules. In a broad sense, it is a small step in expanding the types of materials which can be studied in the ultracold regime. It is a direct continuation in the science, art, and tradition of low temperature physics. While I will go on to describe the specific, short term motivations for such a study, they should all be taken with a grain of salt. In 1877 liquid oxygen was discovered, and in 1969 used as fuel to reach the moon. Onnes' discovery of superconductivity in 1911 was used last year to obtain an MRI image of my knee to diagnose an athletic injury. The long term impact of science is impossible to predict. The formation of ultracold NaLi molecules is unlikely to leave any such profound consequences, but it is nonetheless a step forward in low temperature physics. Will the relatively young field of ultracold atoms and molecules grow to produce life changing events? To me, it already has.

1.1 Interacting atoms and molecules at absolute zero

The seminal works of 1995 demonstrated the cooling of gases of ^{87}Rb (University of Colorado [4]) and ^{23}Na (MIT [5]) in an isolated ultrahigh vacuum (UHV) to a regime known as quantum degeneracy. Quantum degeneracy occurs when the thermal de Broglie wavelength of each atom, λ_{dB} , begins to exceed the interparticle spacing, $n^{-1/3}$, where n is the gas number density⁵—that is, the atoms begin to overlap. ^{87}Rb and ^{23}Na are both bosonic⁶, and at quantum degeneracy undergo a phase transition to a Bose-Einstein condensate (BEC). The interactions between the alkali atoms result in the BEC itself to be a superfluid, the same effect observed in liquid Helium and the superconductivity of electrons in a metal. Ostensibly, these systems are wildly different—one a dilute vapor of atoms in a UHV chamber, the other electrons in a chunk of metal in a Helium refrigerator—but they have in common that their

⁵Equivalently, quantum degeneracy is reached when the phase space density is approximately unity, $n\lambda_{\text{dB}}^3 \approx 1$.

⁶Bosonic species have integer total spin, while fermionic species have half-integer total spin.

constituent particles follow the laws of quantum mechanics, and thus it was natural to use ultracold systems to “simulate” the physics of electrons in a solids.

Quantum simulation with ultracold systems is a rapidly growing field dedicated to exploring problems in interacting, many-body quantum systems that are too computationally complex to simulate on a computer [6]. Table 1.1 shows a comparison of energy scales and techniques to describe the correspondence between a dilute ultracold gas and a chunk of metal.

	Ultracold dilute gases	Electrons in a metal
Particles of interest	Atoms or molecules	Electrons
Number density	10^{12} cm^{-3} (*)	10^{22} cm^{-3}
Environment	Magnetic or optical trap (*) Optical lattices (*)	Crystal lattice of nuclei
Fermi temperature (T_F)	$2 \mu\text{K}$ (*)	$5 \times 10^4 \text{ K}$
Interaction energy	100 nK (*)	10 K
Simplest probing techniques	Direct spatial imaging	Transport (resistance) measurements

Table 1.1: Comparison of ultracold atomic and condensed matter systems. All numbers are order-of-magnitude approximations, and vary between different atoms/materials. The (*) label indicates which parameters are experimentally simple to vary, demonstrating the high degree of control possible in ultracold systems which makes them suitable as quantum simulators.

An example of a notable success in quantum simulation is the BEC-BCS crossover [7]: In the years following BEC of bosons, fermionic alkali atoms such as ^{40}K [8] and ^6Li [9] were cooled to quantum degeneracy. In the presence of interactions, these fermionic species showed exactly the same superfluidity mechanism as in low temperature superconductors, known as Bardeen-Cooper-Schrieffer (BCS) pairing. A key component of this work was the ability to change the strength of atom-atom interactions using a magnetically tunable Feshbach resonance [10]. Such tunability is not possible in condensed matter systems, and this has allowed ultracold fermionic atoms to go beyond simply simulating known effects in metals, as demonstrated in experiments measuring the superfluid transition in strongly interacting (unitary) Fermi gases [11]. The ability for ultracold gases to simulate new and unexplored physics is particularly important in development of new theories. A modern open problem

is copper-oxide ceramics which exhibit superconductivity at relatively high temperatures of ~ 100 K. Such materials are greatly intriguing towards engineering a room-temperature superconductor, yet a microscopic theory of their superconductivity is still a mystery [12]. One hopes that an ultracold simulation of a novel material could help in finding the answer.

Using the BEC-BCS crossover as an example, it is clear that interparticle interactions are a crucial ingredient in determining the kinds of physics one can study in an ultracold system. Neutral ultracold atoms experience a van der Waals interaction, given by the potential $V_{\text{vdW}} = -C_6/r^6$ where C_6 is known as a dispersion coefficient, and r is the separation between two atoms. This is a “short-range” interaction, which means the $1/r^6$ potential rapidly drops to zero at large internuclear separations such that the interaction is well approximated by a delta function⁷ $V_{\text{vdW}} \propto \delta(r)$. On the other end of the spectrum are “long-range” interactions, such as the Coulomb interaction between two ions⁸, $V_{\text{Coulomb}} = C_1/r$. The Coulomb interaction is of obvious importance in modern trapped cold ion experiments [13], however for the purposes of many quantum simulations the Coulomb interaction is *too* strong: C_1 is so large that the Coulomb repulsion localizes the atoms to form a classical Wigner crystal without any wavefunction overlap between neighboring atoms, negating any quantum effects. Thus there is an interest in creating a tunable, long-range interaction which could be used to observe novel phenomena in quantum many-body physics.

A candidate for a tunable strength long range interaction is that of two permanent dipoles, which can be either electric or magnetic:

$$V_{\text{d-d}} = \frac{A}{4\pi r^3} \left(\vec{d}_1 \cdot \vec{d}_2 - 3(\vec{d}_1 \cdot \hat{r})(\vec{d}_2 \cdot \hat{r}) \right) \quad (1.1)$$

where r, \hat{r} is the interparticle separation and unit vector, \vec{d} are the dipole moments of the two particles, and the coefficient $A = \epsilon_0^{-1}, \mu_0$ for electric and magnetic dipole

⁷The aforementioned experiments on the BEC-BCS crossover using tunable Feshbach resonances changed the interaction strength by changing the prefactor to this delta function, which is a useful feature to simplify theoretical calculations. For details, see [10].

⁸This is an uncommon notation for brevity; here $C_1 = kq_1 q_2$ where k is the Coulomb constant and q are the two interacting charges.

interactions, respectively. An quantum degenerate gas with such interactions could be used to study dipolar effects in ultracold systems [14], with eventual larger goals of identifying new mechanisms for superfluid pairing applicable to solids [15, 16].

In the world of ultracold science, recent experiments to realize the dipole-dipole interactions have taken two approaches: (i) schemes in atomic systems, and (ii) the production of ultracold dipolar molecules, which is a primary motivation for the work of this thesis. With atoms, significant progress with dipolar interactions has been made with ultracold samples of highly magnetic atomic species, such as Chromium ($d=6\mu_B$ [17]), Erbium ($d=7\mu_B$ [18]), and Dysprosium ($d=10\mu_B$ [19]). Recent work with magnetic atoms has shown the emergence of a magnetic ferro-fluid caused by the underlying dipolar interactions [20]. Alongside using magnetic interactions in atoms, there are proposals to produce electric dipole interactions by dressing the atoms with a Rydberg state [21]. Rydberg states⁹ have strong electric dipole moments, but their short lifetime results in a trade-off between dipolar interaction strength and loss, and the use of Rydberg dressing in many-body physics has thus far been limited [22].

The work of this thesis is motivated by the alternative approach to producing an ultracold dipolar gas: the use of molecules with a permanent electric dipole moment. The simplest case is a heteronuclear dimer, where the differing electron affinities of the two atoms skew the electron cloud distribution in the molecule, thus producing a dipole. In atomic units, dipole moments are measured relative to an electron: the electric dipole moment is measured units of ea_0 where e is the electronic charge and a_0 is the Bohr radius, while magnetic dipole moments are measured in Bohr magnetons μ_B , the magnetic moment of an electron. In this thesis we will often use the Debye to measure electric dipole moments, which is defined as $1\text{ D} \equiv 10^{-18}\text{ statC}\cdot\text{cm} \approx 0.39\text{ }ea_0$. The formation of electrically dipolar molecules is largely motivated by the strong nature of electric dipole interactions: If we take the ratio of eq. 1.1 with two electric dipoles of ea_0 to that of two magnetic dipoles of μ_B , we find $V_{\text{d-d}}^{(\text{el})}/V_{\text{d-d}}^{(\text{mag})} = 4/\alpha^2$ where α is the fine structure constant. This ratio is approximately 10^5 , indicating

⁹A Rydberg state is a highly excited electronic state of an atom, typically to states with principal quantum number $n > 30$. The dipole moment of such a state scales as $d \propto n^2$.

the inherent advantage of using electric dipoles to produce strong interactions. This advantage is apparent in specific examples of ultracold systems: the interaction energy between two of the most magnetic atoms, Dy, with $10 \mu_B$ magnetic dipole moments, is equivalent to two molecules with 0.1 D electric dipole moments. The largest electric dipole moments of heteronuclear molecules are typically ~ 4 D [23], and since the dipolar interaction energy scales as d^2 (see eq. 1.1) this results in significantly stronger dipolar effects in molecules than possible with magnetic atoms.

Another advantage of ultracold molecules is that they can also be used to study an entirely different kind of quantum many-body problem: Chemical reactions. Here we momentarily abandon the idea of using long range elastic dipole-dipole collisions as a kernel for observing novel quantum phases and focus on short range chemical reactions. Accurately calculating the dynamics of just two colliding dimers¹⁰ is a non-trivial problem in physical chemistry [24]. The high state purity and control in ultracold molecular systems makes them a perfect test-bed for studies of quantum-controlled chemical processes [25].

Having showered praise over the prospects of ultracold dipolar molecules, we now turn to their primary disadvantage: producing an ultracold, stable gas of dipolar molecules is difficult. The remainder of this chapter will overview the challenges and solutions in producing cold molecules, and the entirety of this thesis is dedicated to solving the problem of producing ultracold NaLi molecules.

1.2 Production of cold molecules

Even the simplest of molecules—dimers made of two atoms—are notoriously difficult to cool to quantum degeneracy. The difficulty stems from the two extra degrees of freedom associated with a bound two-body system: vibration and rotation. Thus far, laser cooling has been the most effective way to cool atoms from a hot vapor (~ 600 K) to the sub-mK regime. Laser cooling relies on the atoms having a closed

¹⁰Two colliding dimers = A collision of four nuclei and a dozen or so electrons, depending on the species.

set of electronic transitions, i.e. transitions which decay to a small set of states which can be re-excited by only a few different laser frequencies (a “cycling transition” is the special case where the only possible excitation decay is to the initial state, requiring only one laser). Alkali atoms are the ideal case with only one laser color necessary for laser cooling¹¹. In contrast, the plethora of vibrational states in a molecule make it nearly impossible to find a closed set of transitions¹². This is illustrated in Fig. 1-1, the molecular potential energy curves and states of the NaLi dimer. Loosely speaking, the left half of this diagram depicts the numerous molecular states, and the right half free-atom states, of which there are only several. With these considerations in mind, the field of cooling molecules has split into two predominant approaches: (i) direct cooling, which focuses on methods for directly manipulating hot molecules to reach colder temperatures and (ii) ultracold association, which uses the robust techniques for creating degenerate atomic gases in two-species experiments, and then coherently fusing the two different atoms into molecules after they are already near absolute zero.

Currently, the most successful approach to direct cooling of molecules is using pre-cooled molecules from a buffer gas source, followed by laser cooling and trapping in a magneto-optical trap (MOT) [27]. Buffer gas cooling uses cryogenic Helium to produce a source of molecules at ~ 1 K temperatures [28]. The subsequent laser cooling requires substantial modifications from the techniques used in alkali atoms, and here I highlight some key differences: The choice of molecular species is constrained to those with vibrational state branching ratios that form a near-closed transition amenable to laser cooling (currently in use are CaF [26, 29], SrF [30, 27] and YO [31]). The rotational state branching can be closed completely by using a rotating ($N=1$) ground state with laser excitation to a non-rotating ($N'=0$) excited state, however this results in the existence of Zeeman dark states transparent to the laser cooling light. Pumping into these Zeeman dark states can be eliminated by rapidly

¹¹Hyperfine effects actually result in two laser frequencies, but they are typically only ~ 1 GHz apart which is technically easy to implement.

¹²There are also many possible rotational states, however a scheme of forming a cycling transition for rotational states has been developed; see for example [26].

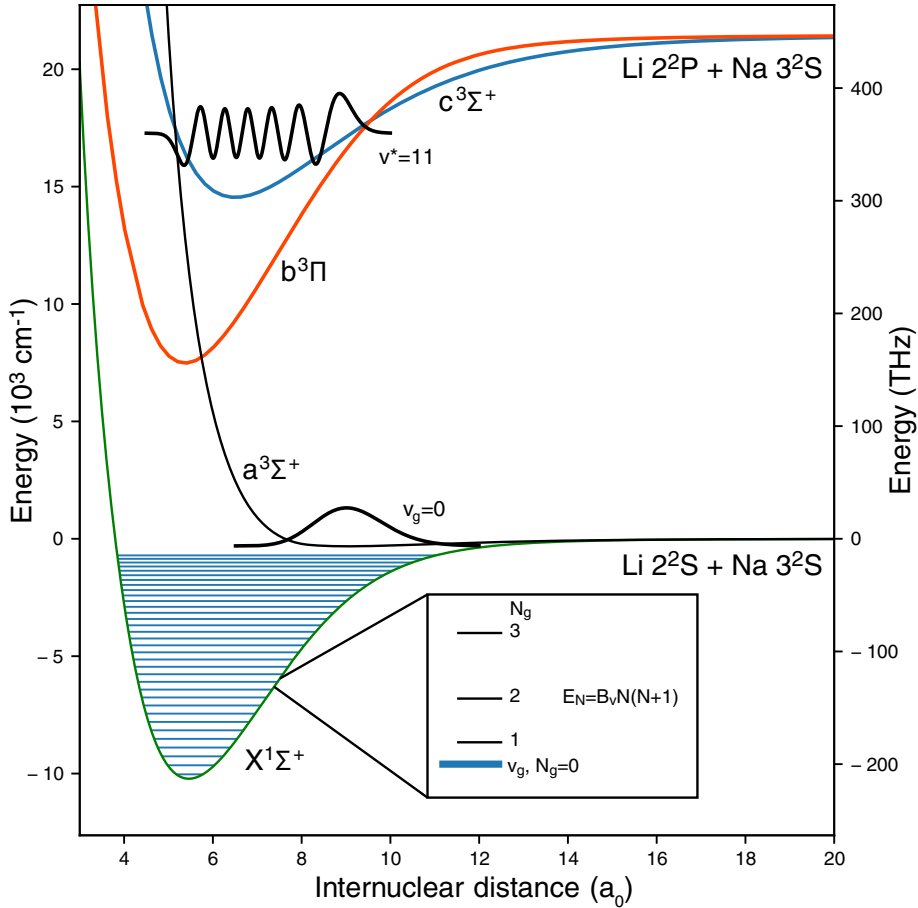


Figure 1-1: NaLi molecular potential overview. The ground ($a^3\Sigma^+$) and first excited ($c^3\Sigma^+$, $b^3\Pi$) triplet potentials as well as the ground singlet potential ($X^1\Sigma^+$) are drawn (the excited singlet potentials have been omitted for clarity). To give a sense of scale, the vibrational states of the singlet potential are drawn (blue) with a typical spacing of ~ 5 THz. The inset shows further rotational state splittings, with energy level spacing of $E_N = B_v N(N + 1)$ where N is the rotational quantum number and the rotational constant $B_v \approx 10$ GHz in NaLi. The lowest vibrational state of the triplet potential ($a^3\Sigma^+$, $v_g = 0$) and an excited vibrational state ($c^3\Sigma^+$, $v^* = 11$) wavefunctions are drawn. A notable feature of the ground potentials is that the triplet potential is much shallower than the singlet. While this diagram is specific to NaLi, the molecular potentials are qualitatively similar for all other heteronuclear bi-alkali combinations.

switching the MOT magnetic field direction at radio-frequency (RF) speeds, requiring the added complexity of high-speed in-vacuum MOT coils. Recent results with direct cooling have produced molecular MOTs with 10^5 molecules at densities of 10^6 cm $^{-3}$ and temperatures of $300\ \mu\text{K}$ [26]. These molecule numbers are a factor of 10^4 smaller than possible in an atomic MOT, but they are competitive with cold molecule pro-

duction rates from ultracold association experiments. Aside from laser cooling, there are alternative direct cooling methods such as Stark and Zeeman decelerators, which use electrically (magnetically) dipolar molecules and rapidly switching electric (magnetic) fields to slow a hot beam of molecules [32]. Recent results with these techniques have gone beyond beam-line experiments, demonstrating magnetic trapping and even observation of evaporative cooling in a sample of dipolar OH molecules [33].

Although direct cooling has made significant advances in recent years, the most effective method to produce near-quantum degenerate gases of molecules has been ultracold association. This method was first demonstrated in 2008 by two groups with Cs₂ [34] and KRb [35], and has since seen ubiquitous use with other species of ultracold atoms. This method begins with an ultracold mixture of two species which is associated to a weakly-bound molecule by using a Feshbach resonance [10]. This highly vibrationally excited molecule is then transferred to its ro-vibrational ground state through a two-photon process known as stimulated Raman adiabatic passage (STIRAP). The entire procedure is state selective and reversible, and does not significantly heat the molecules. The University of Colorado group working with the fermionic KRb molecule has progressed the field by leaps and bounds, with demonstration of molecular formation [35], chemical reactions [36, 37], and dipolar interactions in a lattice [38]. Their experiments have produced $\sim 10^4$ molecules at temperatures of ~ 300 nK. Towards forming a quantum degenerate gas of molecules, these numbers correspond to phase space densities of $n\lambda_{dB}^3 \approx 0.25$ ($T/T_F = 2$, where T_F is the Fermi temperature), a record in the field of ultracold dipolar molecules.

With all the progress in molecule production using ultracold association, there is still much room for improvement. A primary issue is that the fraction of atoms which are converted into molecules is low, typically limited by Feshbach association efficiency to $< 10\%$. This poor formation efficiency results in a loss of phase space density, requiring further cooling of the molecules themselves. A problem arises because the molecules typically do not have favorable collisional properties (i.e. fast inelastic loss), thus making it impossible to use evaporation as is commonly done in atomic systems at ultracold temperatures. Similar collisional issues could exist with the molecules

employed in direct cooling (CaF , OH , etc.). Many groups around the world are circumventing this problem by improving molecule formation efficiency, and ensuring that the molecules never collide with each other. In ultracold experiments, the use of an optical lattice to isolate pairs of atoms can significantly improve Feshbach molecule formation efficiency by eliminating atom-molecule collisions [39]. Another recent idea is to use optical microtraps to catch individual molecules [40], which can be applied to both molecules directly cooled in a MOT or those associated from ultracold atoms. There is certainly no shortage of ideas in the field of ultracold molecule formation, and both direct cooling and ultracold association methods are likely to produce many new results in the near future.

1.3 NaLi and the bi-alkali landscape

We now turn our attention to the world of ultracold association with heteronuclear bi-alkali species. This thesis describes the formation and initial studies with the triplet ground state of the $^{23}\text{Na}^6\text{Li}$ molecule. As we'll see, NaLi is a peculiar molecule compared to other bi-alkali species and is particularly well suited for studies of the triplet state. It should be noted that there are efforts to form heteronuclear ultracold molecules from non-alkali species, such as alkaline-earth atoms [41]. While these mixtures have interesting properties, they currently have a roadblock to molecule formation due to the absence of workable Feshbach resonances in alkaline-earth species [42]. Formation of molecules with mixtures involving the highly magnetic species (Cr, Er, Dy) is an intriguing possibility, but is thus far largely unexplored.

There are a number of parameters to consider when discussing heteronuclear bi-alkali molecules:

- Quantum statistics (fermionic or bosonic): This is determined by the total spin (nuclear and electronic) of the molecule; integer spin makes a boson, half integer a fermion. This is particularly important when considering ultracold collisions, since fermions in the same quantum state can only collide via p -wave collisions which are frozen out at ultracold temperatures [43]. Thus when

considering inelastic loss due to molecule-molecule collisions at ultracold temperatures, typically fermionic molecules have much longer lifetimes than their bosonic counterparts.

- Electronic spin state (magnetic moment): The two valence electrons on each alkali atom can be paired in either a triplet (aligned) or singlet (anti-aligned) spin configuration. The spin configuration determines the symmetry of the valence two-electron wavefunction, and thus greatly affects the interatomic potential between the two atoms. The triplet potential is always much shallower than the deeply bound singlet potential, as shown in Fig. 1-1. This difference between singlet and triplet potentials is common to all bi-alkali pairs. Furthermore, singlet molecules have anti-aligned spin, thus having no magnetic moment (with the exception of the nuclear magnetic moment, which is a factor of 10^3 weaker and negligible for most experimental applications). In the triplet state the valence electrons are aligned, and thus triplet molecules have a magnetic moment of $2 \mu_B$.
- Collisional stability: The ratio of elastic to inelastic two-body collisions in molecules is an important property for sample lifetime and prospects of evaporative cooling. One inelastic loss pathway is reactivity, where a species AB (A, B refer to alkali elements) may be energetically allowed to undergo the exchange reaction, $AB + AB \rightarrow A_2 + B_2$. Other inelastic pathways may exist if the molecule is not prepared in its ground state: For example, collisions of triplet ground state molecules could result in inelastic loss from decay to states in the much deeper singlet manifold (see Fig. 1-1). Thus in principle, singlet ground state, non-reactive molecules are the most desirable candidates for long sample lifetimes. However, as we will discuss shortly, recent experimental evidence has not corroborated this hypothesis.
- Permanent electric dipole moment strength: The electric dipole moment is the key property of a molecule which we would like to use for quantum simulation, thus molecules with a larger dipole moment are preferred. Homonuclear

molecules have zero permanent dipole moment due to their symmetry. Heteronuclear bi-alkali molecules have a wide range of dipole moment strengths, with typically larger values for pairs of atoms with a large mass imbalance. Singlet states also typically have a larger dipole moment, as they are more deeply bound (i.e. shorter equilibrium distance, which can be seen in Fig. 1-1) which results in a more polarized electron cloud due to the differences in short-range forces in the two atomic nucleii. For example, LiCs is one of the most dipolar bi-alkalis with a dipole moment of 5.5 D in the singlet state, and 0.5 D in the triplet state [44, 23]. Note that the term “permanent dipole moment” is a slight misnomer—these molecules must be polarized with an external electric field to observe the long range $1/r^3$ dipole-dipole effects of eq. 1.1.

The first formation of an ultracold dipolar molecule was fermionic $^{40}\text{K}^{87}\text{Rb}$ prepared in its singlet ro-vibrational ground state¹³, a reactive molecule with a dipole moment of 0.5 D [35]. The lifetime of a pure molecular sample is often compared to the “universal” loss rate [43], which is a theoretical upper bound to the inelastic collision rate. The universal model simplifies inelastic collisions by assuming unit probability of loss at short-range, thus its only parameters are the strength of van der Waals (C_6) attraction and the molecular mass (described in Sec. 5.5.2). In the case of KRb, the loss rate was consistent with the universal rate, indicating that two-body reactions played a significant role in limiting the molecule lifetime [36].

Since the seminal work of KRb, other groups have formed singlet ro-vibrational ground state molecules of bosonic RbCs [45, 46], NaRb [47] and fermionic NaK [48] (Table. 1.2). The motivation for using these species of molecules was their large electric dipole moments and non-reactivity, which would in theory make for easy-to-use molecules in quantum simulation experiments. However, measurements of the molecule lifetime in these species showed unexpected results. The lifetimes of the bosonic species (RbCs and NaRb) were measured to be surprisingly short (~ 100 ms), considering the molecules’ chemical stability [45, 47]. The NaK molecule exhibited

¹³Their initial experiment also demonstrated forming the molecule in the triplet ro-vibrational ground state, however the triplet molecule was not used for further studies to its weaker dipole moment of only 0.05 D.

	Singlet	Triplet
Reactive	KRb (fermion, 0.5 D, 2008 [35])	NaLi (fermion, 0.2 D, this thesis)
Non-reactive	RbCs (boson, 1.2 D, 2014 [45, 46]) NaK (fermion, 2.7 D, 2015 [48]) NaRb (boson, 3.2 D, 2016 [47])	

Table 1.2: Experimental efforts to produce dipolar bi-alkali molecules. We classify each molecule by its spin state, reactivity, and give the permanent electric dipole and year of first formation.

significantly longer lifetimes (~ 1 s) due to its fermionic character, however the measured lifetime was still shorter than expected for unknown reasons [48].

These results indicate the presence of a novel inelastic loss process in molecule collisions. The prevailing theory is that of “sticky collisions” [49]: Pairs of colliding molecules form collision complexes, i.e. they orbit one another for a prolonged duration (e.g. ~ 100 ms complex lifetime in RbCs), which then increases the likelihood for a third molecule to join the collision complex and result in three-body loss. The lifetime of a collision complex is proportional to the density of states in the system, thus molecules with higher mass would suffer more loss from sticky collisions. This theory is thus far qualitatively consistent with recent results (especially in the heavier molecules such as RbCs), but conclusive evidence for complex formation is still lacking.

With these recent advancements and roadblocks in the field of ultracold molecules, we now turn our attention to our molecule of interest: fermionic $^{23}\text{Na}^6\text{Li}$. Both ^{23}Na and ^6Li are workhorse species in the field of ultracold experiments, seeing prolific use since the first BEC and degenerate Fermi gas experiments. Would their dimer make for an interesting molecule? In the absolute (singlet) ground state, the NaLi molecule is reactive with a predicted electric dipole moment of 0.5 D [23]. However, due to its light mass, fermionic nature, and small van der Waals interactions, the universal reaction rate is expected to be the smallest out of all the bi-alkali pairs (Fig. 1-2), with estimated lifetimes of > 1 s at densities of 10^{12} cm^{-3} [43]. Such a favorable universal lifetime indicates that NaLi molecules will be experimentally usable in any internal state (since the short-range loss mechanism is irrelevant), including the triplet ro-

vibrational ground-state. In the triplet ground state, NaLi has a predicted electric dipole moment of 0.2 D [44], along with the magnetic dipole moment of $2 \mu_B$ from the aligned electron spins. Fig. 1-2 shows a comparison of the universal loss rates and dipole moments for all bi-alkalis in their triplet ground state, showing NaLi as a reasonably good candidate. While past experiments have focused on the singlet ground state due to its stability (a hypothesis which is now under question due to the “sticky collisions”), we chose to focus on the triplet ground state of NaLi, which has an inherently slow inelastic loss rate.

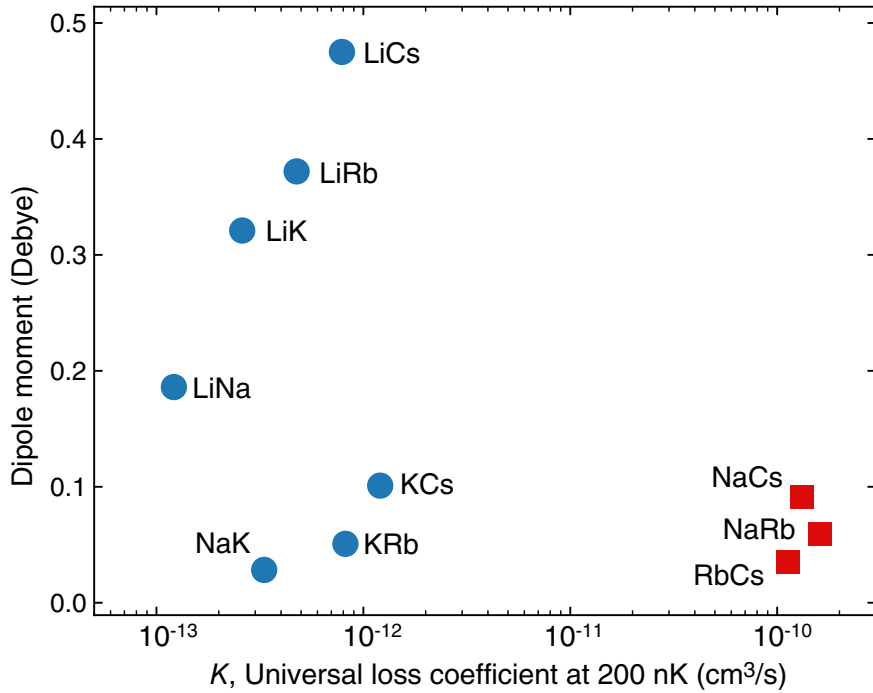


Figure 1-2: Dipole moments and universal loss rates for triplet heteronuclear bi-alkali dimers. The dipole moments for triplet ro-vibrational ground state molecules were obtained from [44], and the universal loss rates were calculated using the methods described in Sec. 5.5.2 with C_6 coefficients from [50]. Blue circles indicate fermionic species which must collide in the p -wave channel, and red squares indicate bosonic which can undergo s -wave collisions and thus have significantly higher universal loss rates.

Triplet NaLi has both an electric and mangetic dipole moment. While the electric dipole moment of triplet bi-alkalis is smaller than that of singlets, the extra magnetic dipole moment opens up a variety of new experimental possibilities. In quantum

simulation, certain lattice models require a non-zero spin which can interact with the electric dipole to simulate a variety of many-body Hamiltonians [51]. In quantum chemistry, the non-zero magnetic moment can be used to tune collisional resonances in molecules, analogous to Feshbach resonances observed in atomic systems [52]. Furthermore, NaLi is the lightest bi-alkali, resulting in a number of interesting opportunities. First, the light mass results in the lowest inelastic universal loss rate and also the lowest rate of sticky collisions among the bi-alkalis [49]. Collisional experiments with NaLi could elucidate the open problems of inelastic collisions in ultracold molecules. Second, the NaLi molecule has weak spin-orbit coupling¹⁴, thus NaLi in the triplet ground state should have weak coupling to the singlet manifold. The suppression of inelastic scattering to singlet states may allow for sympathetic evaporative cooling of the NaLi molecule using collisions with Na atoms entirely within the triplet manifold: while the exchange reaction $2\text{NaLi} \rightarrow \text{Na}_2 + \text{Li}_2$ is possible, the reaction $\text{NaLi} + \text{Na} \rightarrow \text{Na}_2 + \text{Li}$ is theoretically forbidden so long as the bi-alkali molecules involved remain in their triplet states¹⁵ [53]. Sympathetic cooling of molecules with atoms has not yet been demonstrated, and would be a significant step forward to reaching quantum degeneracy with dipolar molecules.

1.4 Thesis outline

The preceding discussion illustrates that triplet NaLi is a new experimental system with numerous prospects, which will hopefully push the field of ultracold science, chemistry, and condensed matter physics for years to come. This thesis describes the experiments in understanding the NaLi molecular structure in its triplet state, and the use of this newfound understanding to form isolated, ultracold NaLi molecules. The method of ground state molecule formation was to use association around a Feshbach

¹⁴The molecule spin-orbit coupling is expected to be weak because the small spin-orbit coupling in the constituent Na, Li atoms.

¹⁵Note that trimer formation, i.e. $\text{NaLi} + \text{Na} \rightarrow \text{Na}_2\text{Li}$, is energetically possible, however this should *not* happen in a two-body collision because energy conservation with only one body in the reaction products is not possible. Thus such processes could only occur in three-body collisions, which are much less frequent.

resonance followed by STIRAP [34, 35]. This work stands on top of prior research on the NaLi molecule in our group, particularly the formation of NaLi Feshbach molecules described in [54] and the thesis of Tout Wang [55]. Thus, the focus of this work is the optical molecular transitions necessary for the STIRAP, coherently transferring the molecules to the ro-vibrational ground state, and finally initial studies using the triplet ground state NaLi molecule.

Chapter 2 is an overview of the ultracold atoms experiment, with a focus on recent modifications for the purpose of formation and manipulation of molecules. Chapter 3 describes our first experiments with optical transitions in the NaLi molecule, where photoassociation (PA) was employed to perform spectroscopy on the excited triplet states of NaLi. Chapter 4 builds upon the PA experiment to perform two-photon spectroscopy of the triplet ground state potential and spectroscopically identify a two-photon transition to the ro-vibrational triplet ground state. Chapter 5 puts all of these pieces together: We revisit our prior Feshbach molecule formation experiments, and implement the coherent STIRAP pulse sequence to transfer NaLi to its triplet ground state. Chapter 5 also describes initial experiments with the triplet NaLi molecule, including the measurement of its lifetime and manipulation of its magnetic dipole moment. Chapter 6 is a summary of the work, describing both short and long term prospects in the NaLi system.

Throughout this thesis we will heavily use molecular physics terminology. A common resource for a physics-perspective on molecules is the text of Herzberg [56]. A concise introduction is also summarized in the thesis of Tout Wang [55] and I have also found fruitful discussions on molecular sub-structure in the book of Brown and Carrington [57]. The notation in this thesis is as follows: v denotes a molecule's vibrational quantum number (with v_g referring to those in a ground electronic state, and v^* an excited electronic state), and similarly N denotes a molecule's rotational angular momentum quantum number. In most cases, the NaLi molecule we will consider are Σ states in Hund's case (b) (i.e., the angular momentum projection onto the internuclear axis is zero, $\Lambda=0$). In this case the total electronic spin (S), the molecular rotation (N), and the total angular momentum ($J=N+S$) are good quantum

numbers.

We will often reference *ab initio* molecular potentials: These are a set of numerical potentials provided to us by the group of Olivier Dulieu, which are explicitly tabulated in Appendix C. There are numerous comparisons of experimental data (especially Franck-Condon factors) to the results from these *ab initio* potentials; this refers to numerical integration of the two-body (Na, Li) Schrödinger equation with these potentials to find bound states¹⁶. Upon completion of the NaLi molecular spectroscopy (Chapters 3 and 4), we were able to calculate improved potential curves which are given [58] and [59]. The primary improvement of these potentials is molecular binding energies at the < 1% level, thus comparisons of Franck-Condon factors to either the improved or *ab initio* potentials yields nearly identical results.

The work of this thesis has resulted in three publications: the spectroscopy of triplet NaLi molecular states [58, 59] and the formation of ultracold NaLi triplet ground state molecules [60].

¹⁶E.g. the potentials, state positions, and wavefunctions in Fig. 1-1 were drawn using the Numerov-Cooley algorithm with *ab initio* data.

Chapter 2

Experimental apparatus

The experimental apparatus, colloquially known as “BEC3”, was built in 2001 to produce ^{23}Na Bose-Einstein condensates and later upgraded in 2007 to co-produce ^6Li degenerate Fermi gases. On occasion the machine is called “The Science Chamber”, which refers to the two-chamber design of BEC3, utilizing a “main” chamber for ultracold atom production, and a second “science” chamber to perform experiments on the atoms (Fig. 2-1). The science chamber is a separate vacuum system isolated from the main chamber by a gate valve, and provides much higher optical access due to the absence of coils and optics necessary for cold atom production in the main chamber. Such a design was necessary in experiments necessitating frequent breaking of vacuum and was used in the pioneering work on atom-chip technology [61]. However, for all BEC3 experiments in the last decade (including this thesis), the main chamber alone has been sufficient.

The primary purpose of this chapter is to give an overview of significant upgrades to the apparatus which were necessary for the spectroscopy and production of ultracold molecules, intended for an audience familiar with the techniques of ultracold atoms. Those looking for a primer on cold atom production are referred to the Varenna notes [62, 63]. Details of the BEC3 design (technical drawings, coil geometries) are given in the thesis of Ananth Chikkatur [64]. The upgrade to produce ultracold Li is described the thesis of Tom Pasquini [65]. Aside from the upgrades discussed below, an overview of the current machine is well described by the thesis

of Gyu-Boong Jo [66]. While the Science Chamber has sat idle for a decade, future work with NaLi molecules will likely require its use; these prospects, along with other potential upgrades are described at the end of this chapter.

2.1 Ultracold Na, Li mixture experiment overview

2.1.1 Cold atom production

BEC3 is an “MIT standard” ultracold atoms machine, outlined in Fig. 2-1. A thorough description of the MIT-style ultracold atoms machines can be found in [67], and here we discuss key points of our NaLi machine and introduce typical experimental parameters and terminology. We use a dual species Na/Li oven to produce a hot atomic beam ($T \approx 450\text{ C}$), which is subsequently slowed to $\sim 100\text{ uK}$ using a spin-flip Zeeman slower. The Na is cooled and confined in a dark-SPOT magneto-optical trap (MOT) [68], which gives $\sim 10^{10}$ Na atoms at a temperature of $\sim 500\text{ }\mu\text{K}$. The Li uses a conventional MOT (with each of the 6 MOT arms containing both MOT laser cooling and repumping laser frequencies) to produce 10^7 atoms at a similar temperature to the Na. The MOTs are simultaneously loaded for $\sim 4\text{ s}$, after which the atoms are optically pumped into the stretched states $|F = 2, m_F = 2\rangle$ for Na and $|F = 3/2, m_F = 3/2\rangle$ for Li, where F, m_F is the total angular momentum quantum number and projection onto the magnetic field axis, respectively. These states are caught in a Ioffe-Pritchard magnetic trap and the sample is “cleaned” to produce a collisionally stable mixture: any other magnetically trapped states of Na in the upper hyperfine manifold (ie. $|F = 2, m_F = 1, 0\rangle$) are transferred with an RF sweep to the untrapped state $|F = 1, m_F = 1\rangle$, and expelled from the trap (note that the population in lower hyperfine trapped state $|F = 1, m_F = -1\rangle$ should be very small from the pumping process). We do not perform a similar cleaning procedure for Li, since it constitutes a much smaller fraction of the initial magnetically trapped mixture and does not significantly contribute to collisional losses.

The magnetically trapped mixture is cooled for 30 seconds using forced RF evapo-

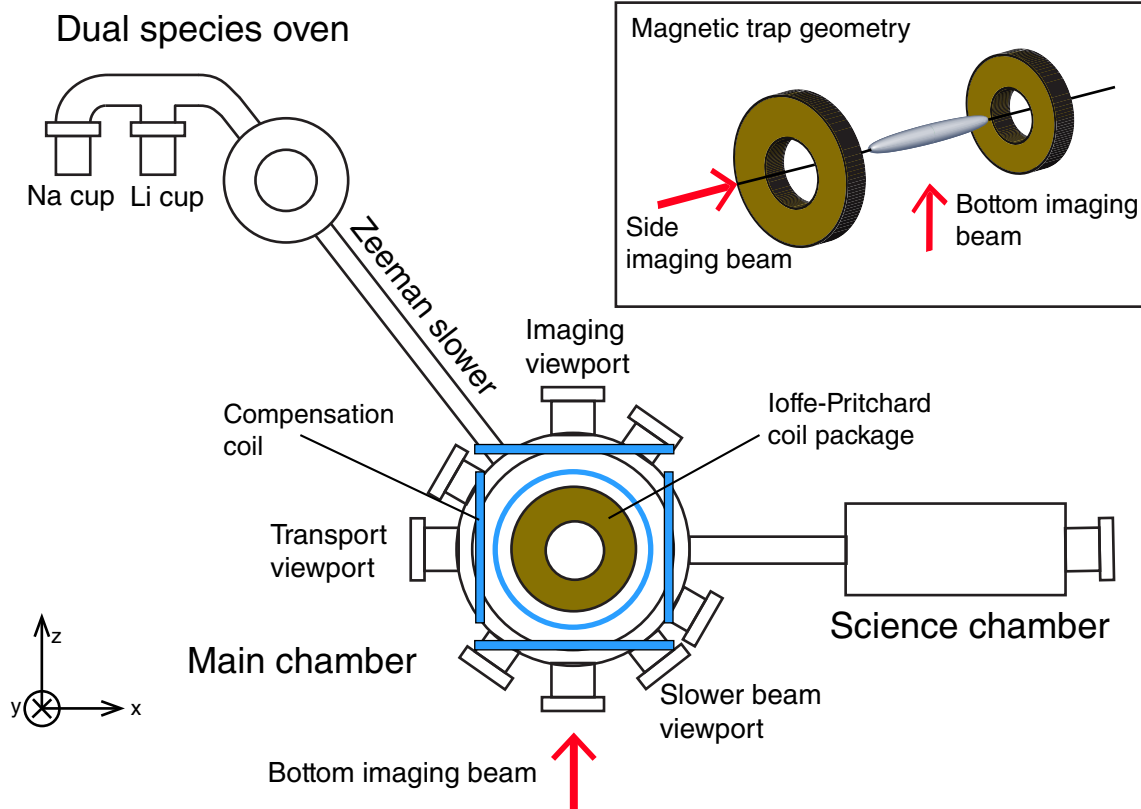


Figure 2-1: A not-to-scale schematic of the experiment geometry. A dual species oven sources a hot Na and Li beam, which is decelerated by a Zeeman slower and trapped in the main chamber. Ioffe-Pritchard coil packages provide magnetic fields for the MOT, magnetic trapping, and Feshbach field (~ 800 G) stages of the experiment. Shim coils wrapped around the chamber are used for minor field adjustments (< 10 G). The atoms are commonly imaged from the top (with the imaging beam entering from the bottom of the chamber), or from the side (with the imaging beam entering from the opposite side). The science chamber was not in use, except occasionally for a beampath to make a crossed optical dipole trap.

ration of Na on the $|F=2, m_F=2\rangle \leftrightarrow |F=1, m_F=1\rangle$ transition at ~ 1.8 GHz. The Li is not evaporated, but rather sympathetically cooled by the Na. At the end of this process, the machine produces a typical mixture of 5×10^6 atoms in each species, at a temperature of $T = 2 \mu\text{K}$, with a total cycle time of 40 seconds. The magnetic trap is cigar shaped, with radial trapping frequency $\omega_{r,\text{Na}} = 290$ Hz, axial trapping frequency $\omega_{z,\text{Na}} = 13$ Hz for Na, and corresponding Li trapping frequencies scaled by the mass ratio $\sqrt{m_{\text{Na}}/m_{\text{Li}}} \approx 2$. The final peak densities were typically $n_{\text{Na}} \approx 1 \times 10^{13} \text{ cm}^{-3}$ and $n_{\text{Li}} \approx 5 \times 10^{12} \text{ cm}^{-3}$. The species number balance is easily modified by varying

the duration of MOT loading (e.g. 2 s of Na MOT pre-load, followed by 3 s of dual species MOT loading). A good benchmark for machine performance is pure Na BEC number without the presence of any Li, for which 1×10^7 is typical.

The magnetic trap described above is the starting point for the photoassociation (PA) and two-photon spectroscopy experiments described in Chapter 3 and 4. For the production of ground state molecules (Chapter 5), we required the use of a NaLi Feshbach resonance in the Na $|F=1, m_F=1\rangle$ and Li $|F=1/2, m_F=1/2\rangle$ hyperfine states that are not magnetically trappable (often named the Na $|1\rangle$ and Li $|1\rangle$ states at high magnetic fields, as depicted in Fig. 2-2). Thus, an optical dipole trap (ODT)

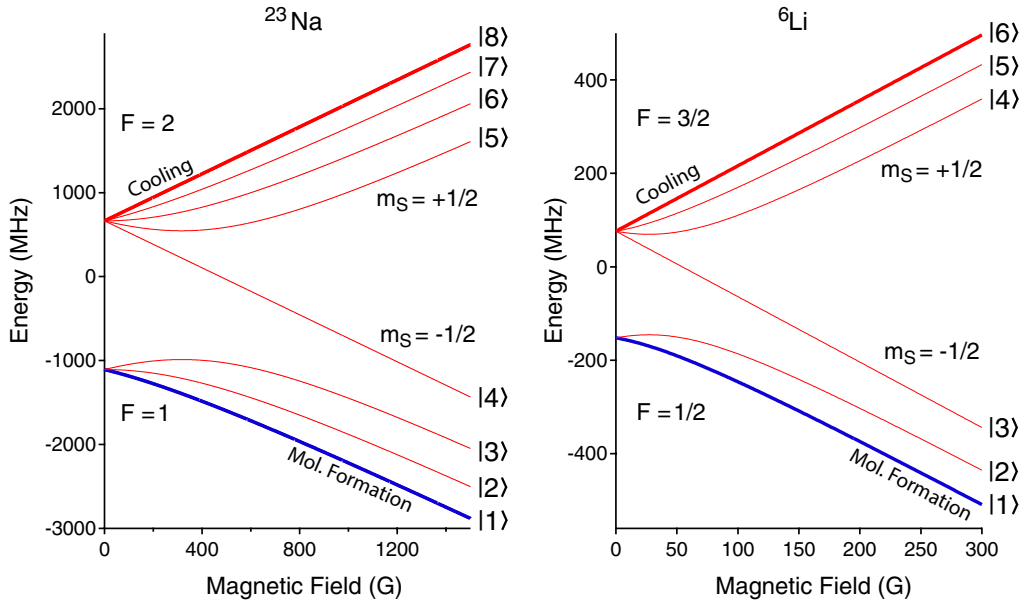


Figure 2-2: Hyperfine states of Na and Li in a magnetic field. The Na (left) and Li (right) hyperfine states split into two manifolds according to their electron spin orientation relative to the external magnetic field. For ultracold atoms production, a Na $|8\rangle$ and Li $|6\rangle$ mixture is used (thick red lines). For experiments involving molecule formation, RF pulses are used to transfer the atoms to the low field seeking Na $|1\rangle$ and Li $|1\rangle$ states (blue lines).

was necessary, which allowed for the use of the magnetic field for Feshbach molecule formation, rather than trapping. To load into the ODT the RF evaporation was cut short leaving the sample at $T \approx 10 \mu\text{K}$, and the ultracold mixture was then adiabatically transferred into a 5 W, 1064 nm ODT with a beam waist of 30 μm , and trap depth of 200 μK (while this depth may seem excessive given the sample tem-

perature, in practice the high power made ODT alignment much easier). During the ODT transfer the gradient coils (responsible for radial magnetic confinement) were ramped off, leaving the ODT to provide tight radial confinement. The axial trapping force from the ODT Rayleigh range is weak (7 Hz for Na at full ODT power), and the majority of axial trapping was still from magnetic confinement, produced by the curvature and anti-bias coils which were kept on. Both species were then transferred to their lowest Zeeman sublevels (ie. the $|1\rangle$ states) with simultaneous RF Landau-Zener sweeps, and immediately following this the axial magnetic field was flipped to create an axially confining potential for the high-field seeking states (see Sec. 2.3.5 of [63]). The magnetic field was then ramped a few Gauss above the target Feshbach resonance at 745 G, where the sample is further evaporatively cooled by lowering the ODT power to 0.3 W in 2.5 s. After this procedure, typical atom numbers were 1×10^6 each of Na and Li at temperatures of $2 \mu\text{K}$. The corresponding peak densities were $n_{\text{Na}} = 4 \times 10^{12} \text{ cm}^{-3}$ and $n_{\text{Li}} = 3 \times 10^{12} \text{ cm}^{-3}$.

2.1.2 Imaging

The ultracold sample was imaged in absorption from two possible directions: (i) “Bottom” imaging, with the imaging beam entering from below the chamber and producing a top-view of the cloud, showing its elongated aspect ratio, and (ii) “Side” imaging, with the imaging beam entrance along the long-axis of the cloud, hence producing symmetric-looking images with high optical density. We typically used a magnification of 2 for both configurations. Both Na and Li were imaged simultaneously on the same camera, which allowed for quick successive image acquisition with a 5–10 ms delay (depending on the image resolution and camera readout speed). The bottom imaging configuration looked down the direction of gravity and allows for time-of-flight (TOF) times of up to 170 ms, and was the preferred configuration for both atom number counting and temperature measurements. Side imaging was primarily used for beam alignment (ODT, STIRAP beams), however it was also exceedingly useful in observing weak molecular signals (see Chapter 5), owing to the high optical densities when imaging along the long axis of the trap.

2.1.3 Stability

An important aspect for all ultracold atoms machines is stability. This was especially important for our experiments in photoassociation spectroscopy (Chapter 3 and 4), which required repetitive data collection for nearly one year. It was very difficult to perform PA spectroscopy on any day during which the machine produced unstable atom numbers. The majority of stability issues were caused by laser cooling problems, and here I will outline some very simple modifications which greatly reduced atom number fluctuations and drift:

- Fiberized injection lock seeding. The Li laser cooling system used two injection locks to boost the laser power, which were seeded with light from an external cavity diode laser (ECDL) locked to an atomic reference. Rather than sending a free-space beam from the ECDL to seed the injection lock diodes, we used an optical fiber for each injection locked diode, hence modularizing the setup. This made a drastic difference in injection lock stability, especially because tuning the ECDL grating would change its beam pointing direction. By using an intermediate fiber before the injection lock, all pointing fluctuations result in intensity fluctuations in the seed light to which the injection locks are much less sensitive.
- Simple laser table enclosures. We replaced the old curtain-style laser table enclosures with a rigid housing, consisting of sliding plexiglass panels. Just having this simple, passive box around the laser table greatly reduced the amount of day-to-day drift in optics alignment. The long-term goal is to actively temperature stabilize this enclosure, but this has not yet been implemented.
- The Li MOT fluorescence trigger. The Li MOT fluorescence was monitored on a photodiode during MOT loading, and the experiment sequence would continue only when a threshold level of fluorescence was achieved. This trigger would compensate for poor performance when the Li laser cooling system was unstable, allowing us to focus on ultracold atoms physics rather than mundane laser issues.

- Counting total atom number. In experiments with only Na or Li, shot-to-shot number fluctuations of 10 % were typical. In experiments with a Na and Li mixture, 30 % number fluctuations in both species were typical. These fluctuations were anti-correlated due to the changes in heat load for the Na as a sympathetic coolant of Li during evaporation. When a higher than normal amount of Li was loaded into the magnetic trap, this resulted in more Na being evaporated as it tried to cool the Li (and vice versa for a lower than usual Li load). To combat this issue, in experiments where an effect in both Na and Li was expected (e.g. photoassociation loss, Feshbach resonances), a much cleaner signal could be seen by monitoring the total number of both species¹.

The improved experimental stability with these adjustments was crucial in certain data-intensive experiments, such as photoassociation spectroscopy. Fig. 2-3 shows a histogram of data collection times over a 9 month period in BEC3, in comparison to a similar plot from the thesis of Dan Stamper-Kurn [69]. The larger volume of data in BEC3 is perhaps a testament to the stability improvements to BEC machines over the years (though, it is amusing that shape and mean of the histogram is the same).

2.2 Oven and gate valve replacement

2.2.1 Background

Our method of ultracold atoms production used forced evaporation of Na as a sympathetic coolant for Li. This required the number of atoms in the Na MOT to be a factor of $\sim 10^3$ higher than those of Li, and correspondingly the oven flux and usage rate of Na was significantly higher than Li. The oven was initially loaded with 25 g of each Na and Li, with normal operating cup temperatures of 360 C for Li and 300 C for Na. Under these conditions the Na cup was emptied and replaced annually (known as an “oven change”), while the Li was rarely ever depleted (at least it was never an issue during my PhD). Where did all of the sodium go? The beam flux

¹Of course, when confirming an observation that required the presence of both species, we would double-check with each species individually.

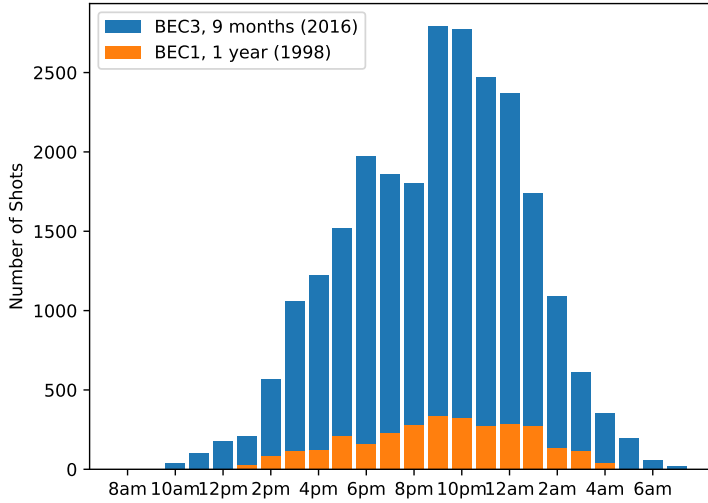


Figure 2-3: Histogram of most common times to take experimental data. In blue is a histogram of experiment cycles from BEC3 during the period of Aug 22 2016 - May 15 2017, during which we worked on Feshbach molecule formation, STIRAP to the triplet ground state, and studies of the triplet ground state molecules. In orange is similar data from 1999 in BEC1.

to the main chamber is at most 10^{12} atoms/second; even if the oven was on all year that would account for $10^{12} \frac{\text{atoms}}{\text{second}} \times \left(3 \times 10^7 \frac{\text{seconds}}{\text{year}}\right) = 1 \text{ mg}$ of Na deposited into the main chamber (and even this is a huge overestimate, since the oven shutter is mostly closed). The answer (as anyone who has looked inside a Na oven viewport would know), is that only a small solid angle of the beam makes it down the slower tube, and the rest is deposited onto the walls of the oven chamber itself.

During a routine oven change in late 2013, this became a problem. While baking the oven after a successful Na oven change, all of the sodium that was collected on the walls liquefied, and began to flow and migrate to unwanted areas of the oven. This sodium clogged the oven shutter mechanism, destroyed the ion gauge, and cracked a vacuum viewport (which miraculously still held vacuum). Furthermore, the gate valve separating the oven from the Zeeman slower was already broken, hence there was always an ominous worry that a vacuum failure in the oven would propagate to the main chamber. For these reasons we decided to replace the oven entirely. During this time we were lucky to have with us a highly talented Master's student, Pascal Notz,

and the diagnosis of the oven issue, new oven design, replacement procedure, and performance testing are all very well documented in his thesis [70]. In the following, I will only summarize key modifications to the oven design, comment on its performance to date, and discuss possible future improvements.

2.2.2 Improved oven and cleaning procedure

A schematic of the improved oven is shown in Fig. 2-4. The goal of the new design was for an oven with a similar form factor to the previous design (so it would approximately fit in the same location), but with significantly less risk of similar “melt-down” failure and lower possibility of vacuum issues propagating to the main chamber. The old faulty gate valve was replaced with two all metal gate valves. It has become an empirical fact in both the Ketterle and Zwierlein groups that gate valves seem to suffer damage from the alkali atomic beams, although the exact mechanism is not clear. The current solution is redundancy, preferably using gate valves from two different manufacturers.

The prior oven shutter was based on a rotary bearing feed-through design which became clogged with solid sodium. This was replaced with a much simpler shutter consisting of a flat sheet of copper attached to a flexible vacuum bellows, which moves in and out of the atomic beam-path (for details, see Sec 4.6 of [70]). The bellows based design has no moving parts (aside from the flexible bellows itself), and should function even if encrusted by sodium.

The last significant modification was to extend the skimmer such that its end hanged over top of an empty vacuum cup, in an attempt to provide a simple, minimally invasive way to clean the oven and slow down the build up of stray sodium. The skimmer is the first object the atomic beam encounters out of the nozzle, and tends to accumulate large globules of sodium. In the old oven, the skimmer needed to be removed and manually scraped to remove the sodium—an unpleasant process that usually resulted in damage to the skimmer. The new oven uses a cleaning process which does not require manually scraping vacuum components. The skimmer is heated externally above the melting point of sodium, such that the liquefied globules

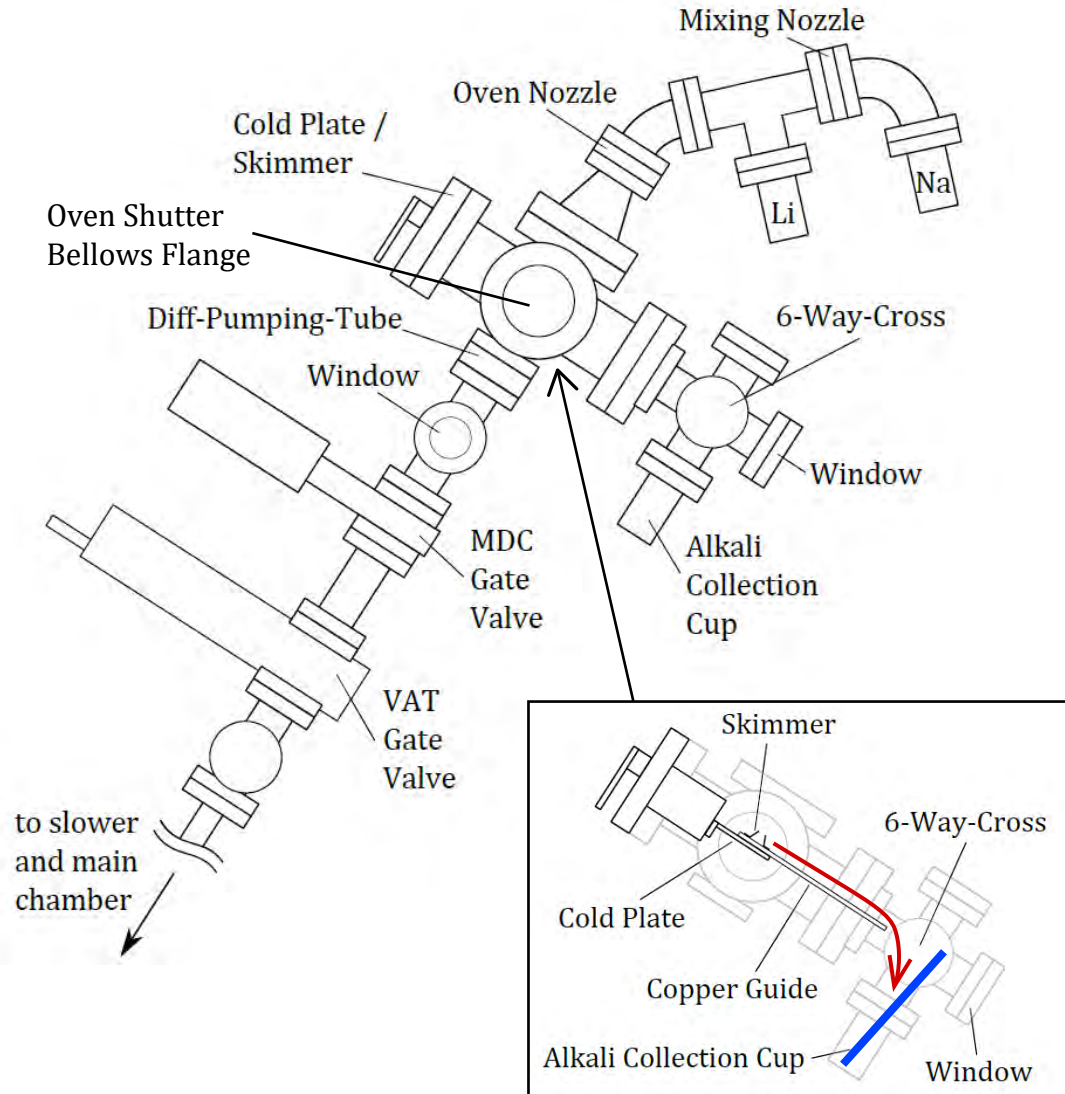


Figure 2-4: Not-to-scale schematic of the new oven. Two gate valves are used to separate the slower from the oven, a pneumatic gate valve (MDC GV-1500V-P-11) and a manual hand-operated valve (VAT 48132-CE01). The oven shutter is transverse to the skimmer and is not shown. Inset: A close up of the skimmer and new alkali collection mechanism. The red arrow depicts the intended path of liquid Na flow during oven cleaning. Initial attempts to clean the oven using this method resulted in Na spilling onto the bottom window. The blue line depicts where a glass shield can be placed to prevent Na from splashing onto the window. Figure adapted from [70].

of sodium flow down off of the skimmer and into the alkali collection cup, which can easily be replaced or recycled back into the oven (Fig. 2-4, inset).

The new oven was successfully installed during the middle of 2014, and has been

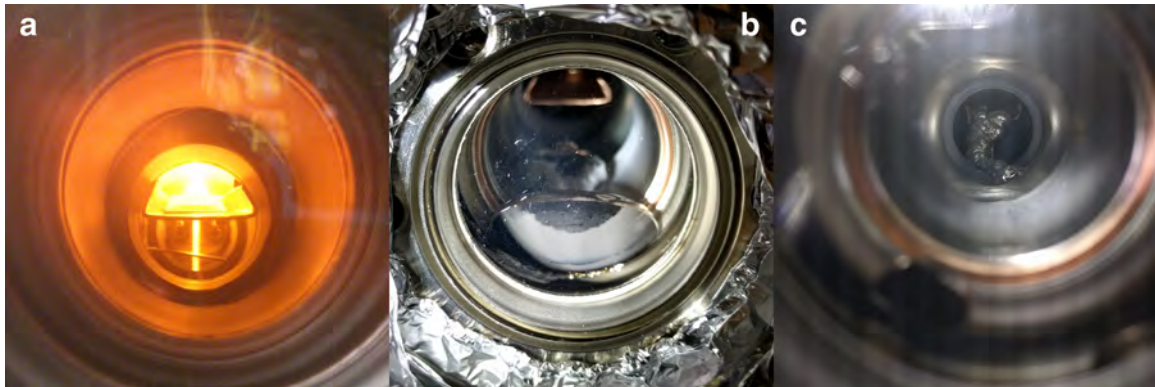


Figure 2-5: Photos of the oven through the bottom viewport. a) Normal oven operation: The atomic beam fluorescence is visible as it passes through the skimmer. Above the skimmer the beam is very bright. Below the skimmer the oven shutter is visible, crossing the beampath. b) Na accumulation on the bottom oven window during cleaning. First attempts at melting Na off of the skimmer (as shown in Fig. 2-4) resulted in Na spilling onto the window. A stream of solidified Na is visible in the background. c) A second attempt at melting Na off of the skimmer with a shortened skimmer. A stream of solid Na is visible. This Na would melt, flow, and re-solidify to form a “waterfall”. In the foreground (out of focus, bottom left) a spot of Na is visible on the window. The shortened skimmer resulted in most of the Na accumulating in the alkali collection cup, but some still managed to splash onto the window.

functioning as expected. During the installation procedure, we also found the slower window (on the main chamber) to have been coated with sodium such that light transmission through the viewport was only 25 %, and it was replaced as well². Since installation of the improved oven, we have attempted to employ the new skimmer cleaning method, but with only partial success. While slowly heating the skimmer, the sodium globules liquefied and slid down the skimmer, but the sodium stream overshot the collection cup, and landed on the bottom viewport! (Fig. 2-5 b) Having little intuitive understanding of the viscous, adhesive, and cohesive properties of liquid sodium, we designed the skimmer to be too long. We immediately pulled out the skimmer, cut it short, and tried the process again (Fig. 2-5 c). The second attempt worked significantly better; the majority of the sodium now fell from the skimmer and onto the bottom of the vacuum flange, which upon further heating caused the sodium to flow into the collection cup. Nonetheless, a small amount of sodium still

²The slower window needs to be heated to $\sim 200\text{ C}$ to prevent coating with sodium from the atomic beam, and we suspect the window heating band failed.

managed to “hop” over the collection cup and reach the viewport again. We did not observe how exactly this happened. The movement of sodium was erratic, sometimes slowly moving when only partially liquefied (forming solid-trails such as Fig. 2-5 b), but flowing very rapidly when a globule was fully liquefied. The flow events were so rapid that we only caught a few glimpses of them by eye, and I suggest the use of a recording video camera in future such experiments.

Despite a small splash of sodium left on the bottom viewport, the procedure worked and the end result was a clean skimmer. A simple solution to the window-splash problem is to insert a long glass slide into the alkali collection cup to act as a transparent shield (a clear “backboard”, to borrow basketball terminology), as shown in the inset of Fig. 2-4. Along with this modification, the new oven is a simpler and cleaner source of hot sodium and lithium compared to past designs, and I hope it will facilitate experiments in BEC3 for many years to come.

2.3 Magnetic field stabilization

2.3.1 Background: do we need active stabilization?

The formation of NaLi Feshbach molecules requires active stabilization of magnetic fields up to ~ 800 G, with field noise less than 1 part in 10^5 . Our prior work on NaLi Feshbach molecules only succeeded in formation of molecules using the 745.4 G resonance that has a width of 10 mG [71, 72, 54]. This is the narrowest resonance around which Feshbach molecules have been formed to date, and the method of magnetic field stabilization used in these experiments is described in Caleb Christensen’s thesis [73]. Unfortunately, since Caleb’s departure from the group, the specific knowledge and physical implementation of his magnetic field stabilization scheme was lost. Thus, our initial attempts to re-form Feshbach molecules as a stepping stone towards the triplet ground state did not use any active magnetic field stabilization. Our intuition that this would work was as follows:

- The large inductance of the Feshbach (anti-bias) coil should filter out noise

fluctuations from the driving power supply. The Feshbach coil has an inductance of $250 \mu\text{H}$ and resistance of $50 \text{ m}\Omega$, making a low pass filter for the current with a 30 Hz corner frequency.

- On an oscilloscope trace, we could see that most of the fluctuations come from 60 Hz wall-plug noise, which was “eliminated” simply by synchronizing the experiment to the 60 Hz wall supply phase (i.e. prior to any magnetic field sensitive step of the experimental sequence, the computer would wait until a peak of the 60 Hz oscillation before proceeding).
- A large amount of fluctuations comes from the noisy analog setpoint which is sent to the controlling power supply, often in the case of 60 Hz noise due to ground loops. This was eliminated using a programmable digital setpoint from a device physically close to the high-current power supply.
- Any outside magnetic field fluctuations (e.g. magnetic field noise at the atoms from a nearby ion-gauge, or other sources external to the Feshbach circuit) would have to add in quadrature with the large 750 G bias field, and be suppressed unless co-axial to the large field.

With these simple modifications, we measured that our field noise was $\sim 10 \text{ mG RMS}$ without any active stabilization. This should have been just low enough to make Feshbach molecules around the 10 mG wide resonance, but all of our attempts failed. Given that we knew our field stability was questionable, we decided to implement an active stabilization circuit, which is described in the next section. But even with the active field stabilization, we could not make molecules. We later discovered that our Feshbach molecule issues were unrelated to the magnetic field, but rather an issue with the free-atom clean-out light pulse (see Sec. 5.2). It turns out that the aforementioned simple magnetic field stability guidelines were sufficient to form Feshbach molecules, without any significant performance decline in comparison to active stabilization.

Nonetheless, here I will present the details of our active magnetic field stabilization scheme. It is a significant improvement over prior stabilization schemes, both in the

noise performance and in the methodology used to measure and characterize noise. With this scheme we reach 1 mG RMS noise in the 10^2 – 10^4 Hz band, at bias fields up to 800 G.

2.3.2 Stabilization circuit

The circuit diagram of the Feshbach coil is shown in Fig. 2-6. We used a 20V, 500A commercial power supply (TKD-Lambda, ESS 30-500-2-D-0806), for which we measured the RMS current fluctuations to be $\sim 0.1\%$ ³. When operating at 200 A (roughly corresponding to 700 G), this results in 200 mA of RMS noise current that needs to be suppressed. Prior schemes used a Hall probe to measure the current through the coils, and PID feedback to a high-power insulated gate bipolar transistor (IGBT) in series with the coil to actively suppress noise fluctuations. While this scheme has worked in the past [65, 73], it has a number of draw backs: (i) One must be careful to always ensure a low voltage drop across the IGBT to keep power dissipation low and prevent the IGBT from melting (e.g. at 200 A, a 1 V drop results in 200 W dissipation). (ii) The IGBT is a nonlinear device designed for switching rather than analog performance, and thus requires frequent PID adjustment if used at different bias points. (iii) The IGBT is a large high-power device with a very large gate capacitance⁴, and it has much lower modulation bandwidth than smaller transistors (see Appendix A for comparison). An alternative approach, inspired by the methods of laser frequency stabilization, is to split the feedback path into two: Low speed, high dynamic range and high speed, low dynamic range. In the context of magnetic field stabilization, we used the power supply voltage control as the slow feedback path (full dynamic range, 100 Hz bandwidth), and a low power transistor in parallel with the coil as the fast feedback path (0.2 A dynamic range, 30 kHz bandwidth) as in Fig. 2-6 a. The use of a “tweeter” transistor in parallel to bleed off current from the coil path is an elegant way to reduce the problem of high-current stabilization into the regime of small signal

³This measurement was without any of the simple modifications listed in the previous section. It is the worst-case noise to expect from the power supply.

⁴This is fundamentally because the conductors in high power devices need to have large surface area to accommodate a large current, and capacitance scales with area.

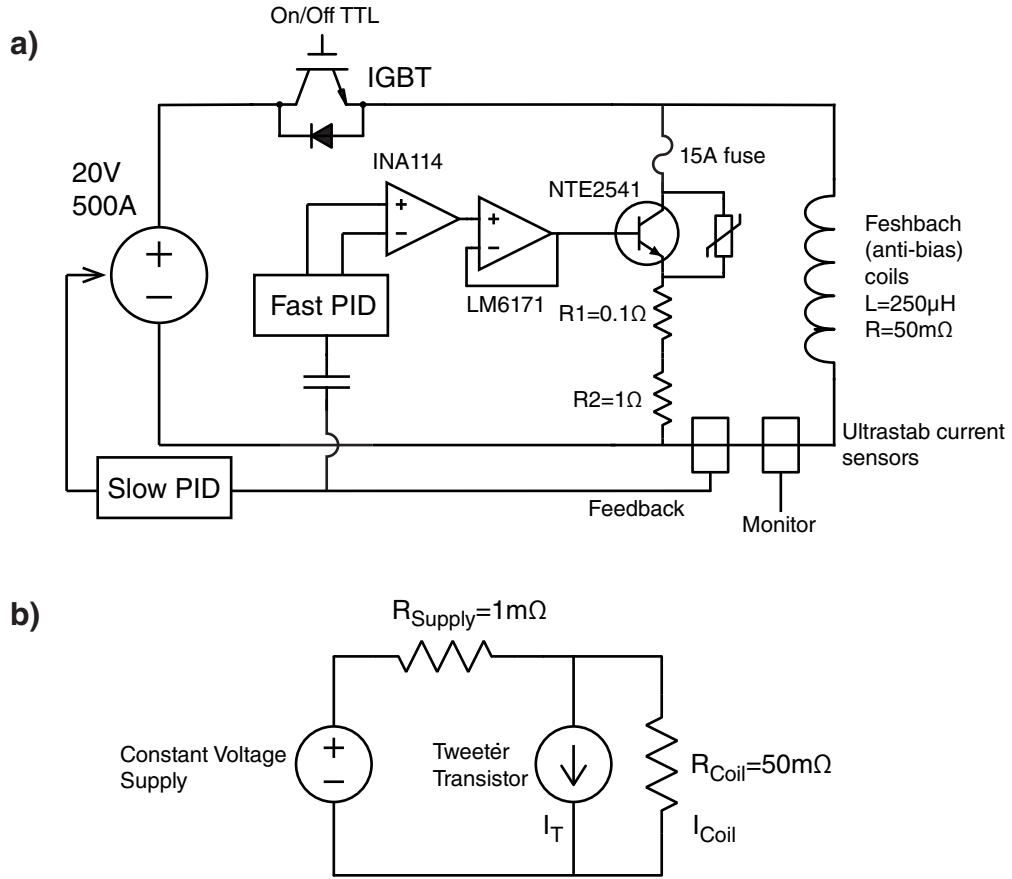


Figure 2-6: Feshbach coil current stabilization circuit. a) The full circuit diagram. The current through the Feshbach coils was measured through a fluxgate current sensor (LEM IT-700S). This signal was split into two feedback paths. The slow feedback was directly to the power supply voltage control using a commercial PID controller (SRS SIM960). The fast feedback path was AC coupled and used a low noise pre-amplifier (SRS SR560) for feedback gain. This signal was passed into an instrumentation amplifier (INA114) for isolation, and an op-amp (LM6171) to drive the tweeter transistor (NTE2541, which is a Darlington pair and requires little drive current, however the gate op-amp was necessary when testing other transistors). R1 was used as a current-sense resistor for testing. R2, the 15A fuse, and a metal-oxide varistor (MOV) were used in order to prevent the tweeter transistor from burning during voltage surges when switching current through the coils. The IGBT (Mitsubishi CM1000HA-24H) was used only to switch the total current. A separate current sensor was used to measure the current through the Feshbach coils. b) A simplified diagram of the Feshbach stabilization circuit. This simple model can be used to understand the modulation limitations of the tweeter transistor. It is missing the coil inductance and other reactive impedances from the power supply. Modeling the reactive components of the circuit was done empirically with a network analyzer.

electronics. A practical benefit from this scheme is during its construction: burning a low power transistor costs only a few dollars, compared to hundreds of dollars for high-power elements. There is one caveat to this, which is that the large power supply driving the coil is fundamentally a constant voltage supply⁵ and inhibits the ability of the tweeter transistor to modulate the coil current. Consider Fig. 2-6 b in the case of $R_{\text{Supply}} = 0$; in this case no amount of modulation current I_T would modify the coil current. Using a simple application of Thevenin's laws we find that the coil current is modulated by the transistor by $\delta I_{\text{Coil}} \approx (R_{\text{Supply}}/R_{\text{Coil}})\delta I_T$, which in our case is 2 % of δI_T . Unfortunately, this means that in order to modulate away 0.2 A of current noise, we need a 10 A transistor, requiring the use of slightly higher power electronics (the NTE2541 transistor we used is rated to 25 A, 120 W). The Feshbach coil current was measured using a fluxgate magnetometer (LEM IT-700s), which measures current from the magnetic field around the current carrying cable and does not directly connect to the coil circuit. We have found the fluxgate magnetometers to have far superior noise characteristics than Hall probes (see Appendix A). The current sensor was split into two feedback paths, connecting to commercial amplifiers and PID controllers (Fig. 2-6 a). In order to prevent accidentally injecting any noise into the circuit (via e.g. ground loops), a separate current sensor was used to monitor the feedback performance and the results are shown in Fig. 2-7.

The active stabilization using the tweeter transistor reduces the field noise by ~ 10 dB up to 10 kHz, above which the performance becomes slightly worse due to the expected servo bumps. The majority of the noise is at 60 Hz and higher harmonics, which can be removed by syncing the experiment to a 60 Hz line trigger, as previously mentioned. Thus, while running the atomic experiment we expect our field stability to be below 1 mG RMS in the $10^2 - 10^4$ Hz band. Without stabilization the RMS magnetic field noise is 10 mG, which is consistent with our observation that active stabilization with the tweeter transistor was not necessary to make Feshbach

⁵Whether the supply is “constant voltage” or “constant current” depends on the frequency band considered. For example, at high enough frequencies the cable inductance would make a current source (i.e. $R_{\text{Supply}} = j\omega L$ becomes large). However, for the relatively low frequencies considered here the supply is well modeled as an ideal voltage source with a purely resistive output impedance.

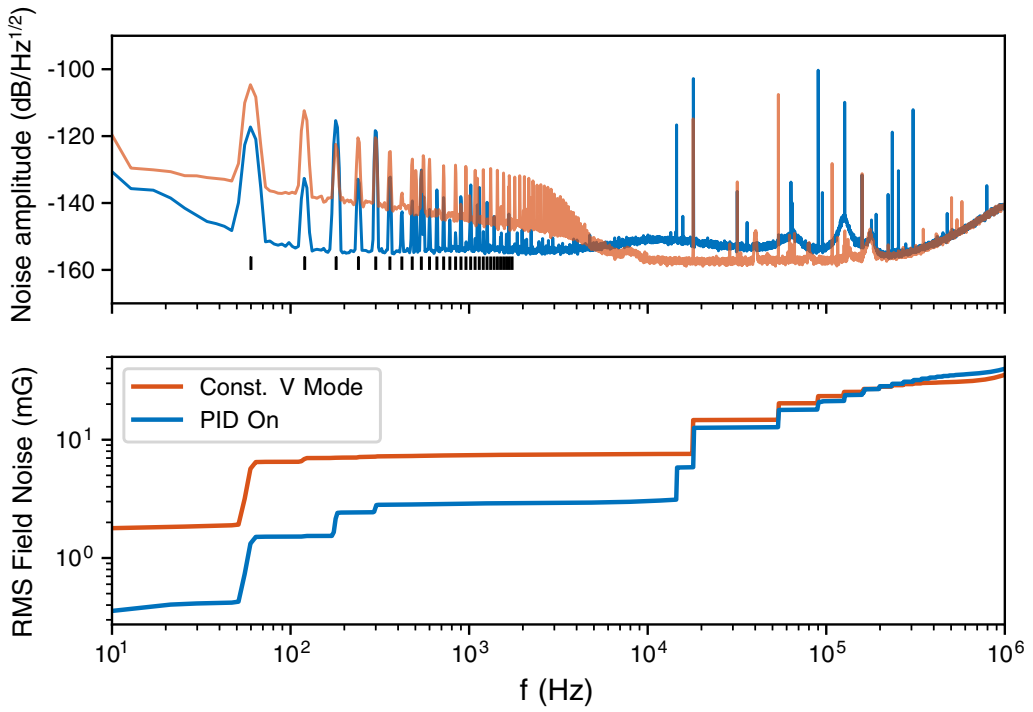


Figure 2-7: Feshbach field noise spectrum measurement at 750 G. a) The noise spectrum of the current through the Feshbach coils. Black lines mark 60 Hz and higher harmonics. The active field stabilization reduces noise up to 5 kHz, however servo-bumping is observed at higher frequencies. This spectrum was measured by amplifying the fluxgate current measurement using a commercial pre-amplifier (SRS SR560), and taking the Fourier transform of the oscilloscope trace. The noise amplitude is calculated as $20 \log(I_{\text{noise}}/I_{\text{DC}})$ where I_{noise} is the noise spectral density in units of $\text{A}/\sqrt{\text{Hz}}$ and I_{DC} is the DC current, approximately 230 A to produce a 750 G bias field. b) The RMS magnetic field noise at 750 G ($I_{\text{DC}} = 230$ A), calculated by integrating the noise spectrum from 1 Hz up to f . There is a significant noise contribution from the 60 Hz peak, and another significant bump at 16 kHz which is the switching frequency of the fluxgate current sensors.

molecules (note that we still required the slow feedback to the coil power supply).

While this feedback scheme was more than sufficient for our purpose of Feshbach molecule formation, there is still room for improvement. The fast feedback bandwidth is not limited by transistor speed (which is in excess of 1 MHz), but rather LC resonances formed by the large Feshbach coil inductance and stray capacitance in the high current power supplies (see Appendix A). Another issue is the linearization

of the tweeter transistor, which would allow for better PID performance when the full dynamic range of the transistor is necessary. In principle, this is easily achieved by placing the transistor (NTE2541) in the feedback path of the driving operational amplifier (LM6171)⁶, but in practice this requires careful placement of shunt capacitors to ensure the linearized circuit doesn't oscillate. We gave only modest effort in solving these issues, and ultimately they were unimportant to the physics of ultracold molecules.

2.3.3 Feshbach molecule sweep coil

The field stabilization circuit previously described does well in order to make a noise-free DC bias field near the Feshbach resonance of 745 G, however it was not designed for fast field sweeps that are necessary to make Feshbach molecules. In the past, the Landau-Zener magnetic field sweeps for Feshbach molecule formation were performed with one of the external compensation⁷ coils coaxial with the Feshbach coils. The compensation coil was driven by a commercial low current supply of ~ 10 A (producing ~ 10 G) with an off-the-shelf noise stability of 0.01 %. During development and testing of the high-current Feshbach coil, we noticed that modulating the current in the compensation coil would inductively inject the modulation into the high-current Feshbach circuit. The compensation coil is in Helmholtz configuration, co-axial to and surrounding the Feshbach coil, thus it makes sense that there is a large cross inductance between the two coils. While this effect found use in injecting noise into the Feshbach circuit to test the active stabilization feedback, it limited the speed at which we could sweep the magnetic field using the compensation coil. Intuitively, the inductance of the Feshbach coil tries to keep the field constant, and changes in the total field flux through the coil are counter-acted by an induced current.

For these reasons, we decided to make a single small coil with a very small area that would be placed as close as possible to the atoms to do very fine field sweeps, which we called the “Mok” coil (named after Hyungmok Son, the graduate student

⁶See for example The Art of Electronics by Horowitz and Hill, p. 257 example CC.

⁷Sometimes called “shim” coils.

who wound it). The small area ensured a small cross inductance to the Feshbach coil, such that we couldn't find any measurable current cross-modulation between the two coils. The Mok coil was 1 inch in diameter with 7 turns of 32 American wire gauge (AWG) copper wire, inserted into one of the bucket windows as close to the atoms as possible. This coil produced 35 mG/A at the atoms, allowing for 0.5 G field sweeps with modest power current supplies. In all Feshbach formation experiments, the large stable DC bias field was produced by the Feshbach coils, and the molecule formation sweeps were performed by sweeping the Mok coil.

2.4 Laser systems for NaLi molecules

Unlike alkali-atoms, molecules have a broad range of ro-vibrational energy levels with excitation spectra spanning hundreds of nanometers. We required new laser systems for spectroscopy, formation, and optical trapping of the NaLi molecules. Table 2.1 overviews the laser systems used for the manipulation of NaLi molecules.

In the following sections I discuss the laser systems used for PA spectroscopy and coherent transfer to the NaLi triplet ground state. For optical trapping of NaLi molecules, we required the use of longer wavelength lasers than our standard 1064 nm ODT to observe long lifetimes, and this is presented in detail in Chapter 5. The 1319 nm laser is a typical, out-of-the-box system without any significant modifications. In most cases, the lasers in Table 2.1 were introduced to the atomic/molecular cloud along the long axis of the trap (see Fig. 2-1, inset).

2.4.1 Spectroscopy lasers

Our initial exploration of excited molecular states in NaLi was using PA spectroscopy, which was performed using an external cavity diode laser (ECDL) at 671 nm. Using an ECDL for spectroscopy was difficult: The mode-hop free tuning range is at best 3 GHz with a maximum tuning range of ~ 5 nm. Searching for a single PA transition over hundreds of GHz required frequent adjustments of the ECDL, and searching for other PA transitions required occasionally switching laser diodes to access different

Table 2.1: Lasers used for manipulation of NaLi molecules

Laser Name	Wavelength	Power	Purpose
“670 TiSaph” (M2 SolTiS)	670-725 nm	1.5 W	PA spectroscopy, high vibrational states of $c^3\Sigma^+$
“Standard TiSaph” (M2 SolsTiS)	725-900 nm	2 W	PA spectroscopy, STIRAP upleg
Downleg ECDL (Homebuilt)	819 nm	20 mW	STIRAP downleg
Mephisto	1319 nm	1 W	ODT for molecules

wavelengths. Another issue was the spontaneous emission pedestal⁸, which would resonantly excite the free Li atoms and result in heating of the ultracold sample. This pedestal was filtered out by passing the ECDL output 3 times through a heated Li vapor cell. With this method, we found the first 18 PA lines ($v^* = 51 - 34$, spanning the range 671-694 nm) using an ECDL (see Chapter 3.).

The remaining PA lines were found using two Ti:Sapphire lasers from M-Squared Lasers: one spanning the 725-900 nm range typical of the Ti:Sapphire gain medium, and a newer model which could reach wavelengths down to 671 nm (which in principle could be used to laser cool Li). The Ti:Sapphire lasers are easily tunable, higher power devices which allowed for a much faster pace of performing PA spectroscopy. The difference was staggering: It took 4 months to find 18 PA lines by swapping diodes in and out of an ECDL, and 10 days to find the next 29 lines using the Ti:Sapphire lasers⁹. The PA lines initially observed using the ECDL were re-scanned using the Ti:Sapphire lasers. ECDLs typically have a broad spectral pedestal due to amplified spontaneous emission (ASE) which is not spectrally filtered by their low finesse cavity. The Ti:Sapphire laser (with its much higher finesse ring cavity) doesn't have this pedestal issue, and allowed for acquisition of much cleaner PA data.

⁸An ECDL provides light with a ~ 100 kHz linewidth, but in addition emits weak “pedestal” light spanning a few nanometers which corresponds to the broad amplified spontaneous emission profile of the diode.

⁹The deepest PA lines, $v = 0, 1, 2$ were outside the range of our Ti:Sapphire laser, and we are grateful to the Fermil group of Prof. Zwierlein for letting us borrow their Ti:Sapphire laser which could tune down to 1000 nm.

In all spectroscopic studies the wavelength was recorded using a HighFinesse WS-7 wavemeter. The wavemeter is nominally accurate to 60 MHz, however our experience has found it to be reliable down to 20 MHz, which is the spectroscopic uncertainty quoted in our measurements. This was determined by testing the wavemeter using a broad range of wavelengths from locked lasers to atomic references from Li (671 nm), Na (589 nm), and Rb (780 nm). The wavemeter would drift \leq 30 MHz daily, and this was corrected for by daily calibration with Li laser cooling light.

The Ti:Sapphire lasers were tunable from a computer interface, and using the application programming interface (API) provided by the wavemeter and Ti:Sapphire lasers we implemented a “soft-lock” to digitally lock the laser to a desired wavemeter value. We estimate the soft-lock provided a relative stability of 1 MHz, and greatly increased the quality of PA data (especially PA line strength data, where the laser needed to be constantly on PA resonance; see Chapter 3). We could also implement this softlock on an ECDL using an Arduino microcontroller to convert digital feedback commands to an analog signal for the ECDL piezo control.

2.4.2 STIRAP lasers

The formation of ro-vibrational ground state molecules from a highly excited Feshbach state used the technique of two-photon stimulated Raman adiabatic passage (STIRAP) [74, 75]. This technique uses two laser pulses designed to keep the molecules in a coherent “dark” state—a state without any probability of electronic excitation and thus no loss from spontaneous emission. The physics of STIRAP is discussed in detail in Chapter 5, and here we only concern ourselves with the technical requirements of the two lasers.

For the molecular potentials of NaLi, we decided to use an 833 nm (“upleg”) and 819 nm (“downleg”) laser frequencies to couple the NaLi Feshbach and ground states via the $v^* = 10$ excited vibrational state in the $c^3\Sigma^+$ potential. The frequencies were chosen for a very strong downleg Rabi coupling with a compromised upleg coupling strength (see Chapter 5). The weak upleg transition strength was compensated for by using the high power Ti:Saphhire laser tuned to 833 nm, while the downleg only

required modest powers for which we used a home-built ECDL at 819 nm, following the robust design of the Steck group at the University of Oregon [76].

The STIRAP transfer efficiency depends on the strengths of the two laser couplings, and their relative phase stability. A simple estimate of the laser phase constraint is as follows: The typical Rabi frequencies achievable in a bound-to-bound molecular transition are $\Omega_{\max}/2\pi = 1$ MHz, and since STIRAP is an adiabatic process it requires pulse durations longer than Rabi frequency, for example $\tau_{\text{pulse}} \gg 10 \Omega_{\max}^{-1} \rightarrow \tau_{\text{pulse}} \sim 2 \mu\text{s}$ (the factor of 10 is somewhat arbitrary here, however it turns out to be a reasonable value; see eq. 13 of [75]). Ideally there would be no phase fluctuations over the duration of the pulse, hence we require the relative linewidth of the two lasers to be narrower than the Fourier limited bandwidth of the pulse, i.e. $\delta\omega_{\text{lasers}} < 100$ kHz. A more careful calculation requires the specific details of the two laser pulse shapes along with a well defined noise model, which can be found in [77]. While the simple calculation presented here provides some intuition for the technical constraints in the STIRAP procedure, our target for relative laser stability was significantly less than this 100 kHz estimate for two reasons: (i) We did not know *a priori* what Rabi frequencies are experimentally achievable in the NaLi system, and even considered the possibility of a free-to-bound upleg transition for which we expected orders of magnitude weaker upleg Rabi frequencies (see Chapter 4), and (ii) A survey of prior STIRAP experiments with ultracold atoms typically used pulse durations of < 1 ms with lasers locked to 1 kHz. Erring on the side of caution, our goal was a similar relative linewidth for the two STIRAP lasers.

There are two common methods to make a narrow lock for two lasers with a large frequency difference (in this case, the frequency difference was 6 THz): phase locking different teeth of a frequency comb, and frequency locking to a narrow cavity. While the seminal work with KRb was performed using the former technique [78], we decided to use a narrow cavity lock because of the simplicity of using a passive optical element and prior experience with this technique in the NaK experiment in the Zwierlein group [79]. The two lasers (at 819 nm and 833 nm) are simultaneously passed through a very stable optical cavity, and locked to different interference maxima (see Fig. 2-8).

We used a commercial optical cavity made of ultra low expansion (ULE) glass with a finesse of 3×10^4 (linewidth of 15 kHz), and free spectral range of 1.5 GHz. The ULE cavity was expected to drift in absolute frequency stability by ~ 1 MHz/year, however in approximately 6 months of use for ground state molecule formation no recalibration was necessary¹⁰. This cavity allowed for locking lasers over a range of 810-880 nm to relative linewidths of < 1 kHz (depending on the locking signal-to-noise). Note that strictly speaking this is *not* a phase lock of the lasers, but a narrow frequency lock. This means that if the laser frequencies are compared for some duration of time, their phase variation will be small (because the lasers have a very narrow frequency), however there isn't a deterministic relationship between the initial phases of the two lasers at the beginning of the time interval. For STIRAP, only the phase-noise characteristics are important, and the relationship between the initial phase of the two lasers plays no role in STIRAP efficiency (see Sec. E3 of [75]). Thus, a narrow frequency lock with the ULE cavity was sufficient.

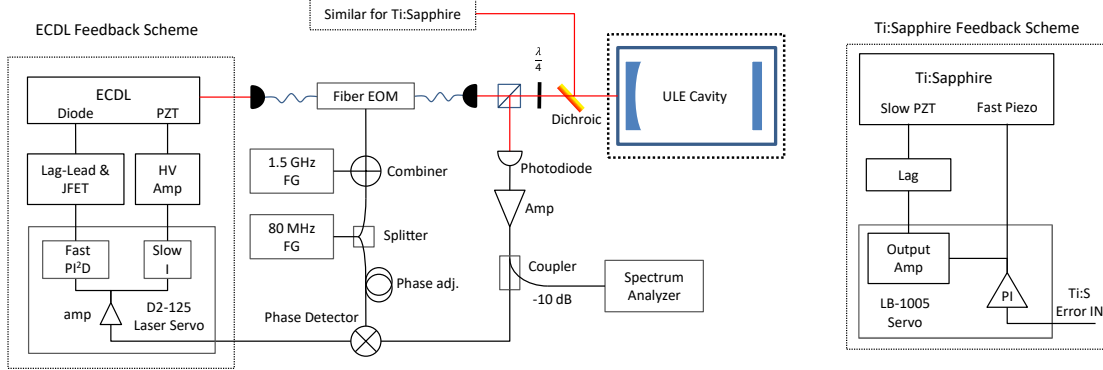


Figure 2-8: Diagram of the STIRAP laser setup. The ECDL and Ti:Sapphire were locked to a ULE cavity. The lasers could be tuned relative to the cavity up to 1.5 GHz using a fiber EOM to offset the lock frequency. The fiber EOM also generated sidebands to generate a Pound-Drever-Hall lock signal. Figure reproduced from [80].

The technical details and test measurements of the STIRAP lasers can be found in the thesis of Sepehr Ebadi [80], a talented and tenacious undergraduate student

¹⁰Our experiment is sensitive to the two-photon detuning rather than absolute frequency stability. Considering the wavelength $833\text{ nm} \rightarrow 360\text{ THz}$, and the locked frequency difference of 6 THz, we expect the two-photon detuning to drift by $6\text{ THz}/360\text{ THz} \times 1\text{ MHz}/\text{year} = 16\text{ kHz}/\text{year}$.

we were privileged to work with for a year. Here, I only summarize key points. For both lasers, we used high frequency fiber electro-optic modulators (EOM) fed with two frequencies to provide a tunable offset from the cavity (up to 1.5 GHz), and the Pound-Drever-Hall (PDH) sidebands (~ 30 MHz) for generating a lock signal. The free-running unlocked linewidth is 50 kHz for the upleg Ti:Sapphire, and 200 kHz for the downleg ECDL [76]. We needed to narrow both lasers to below 1 kHz linewidth. A rule of thumb for laser narrowing is that the feedback bandwidth must be larger than the laser linewidth (this is true for typical laser noise models [81]). Thus the ECDL required a much faster feedback path than the Ti:Sapphire laser. For the ECDL feedback we used a 10 MHz Vescent Photonics D2-125 controller with a phase compensation circuit to provide fast current modulation via a transistor parallel with the laser diode. The Ti:Sapphire feedback was simpler, using a 10 MHz Newport LB1005 controller¹¹ to modulate the piezo-electric elements built into the Ti:Sapphire laser. Note that in this case the modulation bandwidth is limited by the piezo actuation speed, typically < 100 kHz. Although the ECDL was technically more challenging to lock than the Ti:Sapphire laser, we found its locked state to be much more robust against noise. For example, moderate level noise (e.g. talking near the laser) would routinely unlock the Ti:Sapphire, but had no affect on the ECDL. This was improved by wrapping all Ti:Sapphire electrical and water cooling connections with sorbothane at locations where they came in contact with the optical breadboard. A further minor improvement was achieved by enclosing the entire laser with sound-proof foam. These modifications improved the Ti:Sapphire lock stability (only “loud” noises such as hard clapping would unlock the laser). Despite these improvements, the ECDL lock was still more robust, typically insensitive to acoustic noise and unlocking only if something was accidentally dropped onto the laser table.

The relative laser linewidth of the ECDL and Ti:Sapphire laser was estimated by measuring the electrical noise spectrum of the lock signal (for details, see [80]), and the beatnote between the two lasers. By locking the two lasers to adjacent teeth of the

¹¹While the nominal bandwidth of the Newport controller is the same as the Vescent Photonics product, we found the Vescent Photonics controller to have better performance.

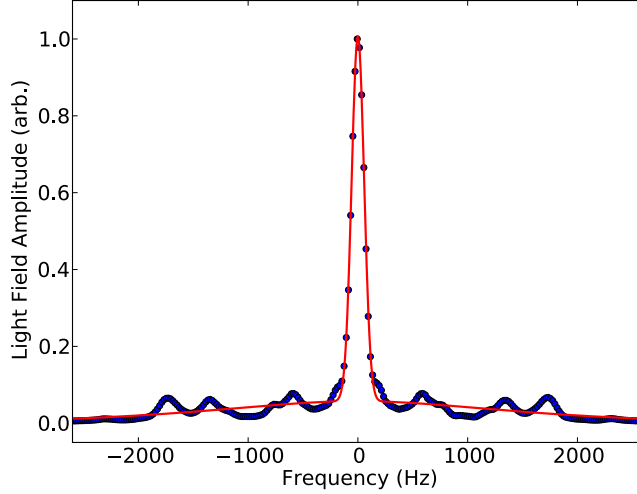


Figure 2-9: Relative linewidth measurement of the ECDL and Ti:Sapphire STIRAP lasers. The two lasers were locked to adjacent cavity mode separated by 1.5 GHz, and by overlapping the lasers on a fast photodiode we measured the corresponding beatnote. This measurement shows a 100 Hz full-width half maximum linewidth over a 2 s integration time.

cavity, the 1.5 GHz beatnote was monitored on a fast photodiode (see Fig. 2-9). From the frequency jitter of the beatnote, we observed a relative laser linewidth of 100 Hz. There are two reasons why this measurement should only be regarded as a lower bound on the relative linewidth. First, the beatnote measurement was performed with the lasers differing in frequency by only 1.5 GHz, while the locking frequency for use in the STIRAP experiment is 6 THz, thus if the linewidth is limited by any “accordion” type vibrations of the cavity, then this effect is amplified by a factor of ~ 1000 when the lasers are locked to their working frequencies. Second, passing the locked laser light through an optical fiber can lead to \sim kHz scale broadening from the mechanical vibrations in the fiber [82]. In our experiment both lasers are passed through the same single-mode polarization maintaining optical fiber, but at orthogonal polarizations to produce opposite circular polarizations for STIRAP (see Chapter 5). Since the two polarization maintaining axes of the fiber have indices of refraction typically differing by $< 1\%$, we assume the residual broadening from the fiber is on the order of 10 Hz. When locking the two lasers at their working wavelengths (819 nm and 833 nm), we could no longer perform an optical measurement of the linewidth, but rather we

were able to estimate the absolute laser linewidths to be 400 Hz from measurements of the electrical jitter of the lock signal [80]. Thus, from a combination of optical- and electric-based linewidth measurements, we quote the relative linewidth of our STIRAP lasers to be < 1 kHz.

2.5 Future improvements

I have discussed some of the key improvements and added subsystems necessary for the experiments we have performed on NaLi molecule formation. Future experiments with molecules in BEC3 are likely to become more complex, requiring reliable formation of ultracold molecules everyday. With this in mind, I believe the most beneficial future upgrades to BEC3 should focus on stability. Removing injection locks from the laser cooling lasers, using fiber (rather than free-space optics) to deliver the MOT beams, and improving the Na laser cooling seed-laser mode quality are just some of many small upgrades that would improve stability. BEC3 is nearly a two-decade old machine, however I am very optimistic that with continual upgrades it will continue to deliver world-class performance.

Aside from stability, a large upgrade to BEC3 will be to once again utilize the science chamber. The spectroscopy and production of ultracold NaLi did not require the use of in-vacuum optomechanical devices, and the optical access was (barely) sufficient. However, future experiments will likely necessitate transport of the NaLi mixture into the science chamber. Formation and manipulation of molecules within an optical lattice will require more optical access (even if the MOT optics are placed on flipper mirrors as in newer experiments such as BEC5, the bulky Ioffe-Pritchard coil packages are obstructive). Experiments to polarize the dipole moment of the molecules will require directional microwave horns, or even in-vacuum DC electric field plates. It is my hope that after the initial hurdle of dual species transport to the science chamber, the improved optical access will pay dividends when setting up new, more complex experiments.

Chapter 3

Photoassociation spectroscopy

The use of STIRAP for coherent transfer to the NaLi triplet ground state requires knowledge of both excited and ground state molecular potentials. The NaLi Feshbach molecules are in the $v_g = 11$, $N_g = 2$ state of the ground triplet ($a^3\Sigma^+$) potential [72, 54], thus in order to STIRAP to the lowest state of this potential we needed a suitable excited molecular potential of triplet character. Prior to this work, there were no observations of any triplet excited states of NaLi. Past NaLi excited state spectroscopy experiments used hot ($T \sim 400$ C) Na and Li mixtures [83, 84, 85], which contained free Na, Li atoms, and a thermal ro-vibrational distribution of NaLi molecules (although some experiments such as [84] used supersonic expansion to cool a molecule beam down to 2 K, such a technique does not effectively cool the ro-vibrational degrees of freedom). In bi-alkali molecules the ground singlet potential is much deeper than the triplet, hence the initial thermal distribution was entirely of singlet character, and finding transitions to excited triplet states was forbidden by selection rules. This is particularly challenging in NaLi, which has a large vibrational energy spacing and small spin-orbit coupling, thus singlet-triplet intercombination lines from “accidental” state crossings are rare. Recent experiments to find intercombination lines to NaLi triplet potentials were unsuccessful [85].

The limitation of a singlet character initial state for spectroscopy is readily overcome in an ultracold atoms experiment. The ultracold atoms machine gives hyperfine-state control over the atoms’ collisional state, and in the NaLi system a triplet initial

state can be directly accessed by forming Feshbach molecules, which are of triplet character. Thus from the outset we had two options for excited state spectroscopy: (i) start from Feshbach molecules and look for bound-to-bound molecular transitions or (ii) use photoassociation (PA) from an initial triplet collisional state. The use of Feshbach molecules has the advantage that bound-to-bound transition strengths are a factor of $\sim 10^9$ stronger than PA, giving a much stronger signal. Spectroscopy using an initial Feshbach molecule state was done in many prior bi-alkali experiments with success [35, 86, 87]. However, in the case of NaLi our prior measurement of the Feshbach molecule lifetime was 1 ms, which is prohibitively short for spectroscopy, and so we chose to use PA. PA spectroscopy has been previously used in a number of ultracold mixed species experiments [88, 89, 86, 90, 91], and is particularly useful in experiments involving alkaline-earth species where the prospect of Feshbach molecule formation is difficult [92, 42, 88]. As will be discussed in Chapter 5, when we experimentally revisited NaLi Feshbach molecule formation we found a much improved lifetime of 200 ms, and in retrospect using the Feshbach molecules for spectroscopy may have been a better option. The upshot of our misunderstanding of the Feshbach molecule lifetime is that our PA measurements were the first observation of PA in the NaLi system.

In performing PA spectroscopy, we were given point-wise *ab initio* potential data by Olivier Dulieu, to whom we are grateful (see Appendix C). From these *ab initio* potentials we could calculate that $v^* = 11, 12$ of the $c^3\Sigma^+$ potential would have the largest Franck-Condon factors to the triplet ground state, and finding these states was of particular interest. After our study of PA spectroscopy, we were able to calculate improved potential fits which can be found in [58].

3.1 Experimental approach

Photoassociation (PA) is the formation of a molecule from initially unbound free atoms using a photonic excitation (for a full review, see [93]). If a pair of colliding Na and Li atoms is illuminated with light resonant to an excited molecular state,

the pair can absorb a photon and form an electronically excited NaLi molecule. This excited molecule will then rapidly decay to lower lying molecular states (Fig. 3-1). The ultracold atoms experiment images only the free Na and Li atoms, hence a PA event will appear as simultaneous loss of an Na and Li atom. For a bulk Na and Li mixture, this process can be described by the rate equation:

$$\dot{n}_{\text{Na}} = \dot{n}_{\text{Li}} = -\bar{K}(v^*)In_{\text{Na}}n_{\text{Li}} \quad (3.1)$$

where n_{Na} , n_{Li} are the free atom densities and I is the PA laser intensity. $\bar{K}(v^*)$ is the intensity normalized PA rate coefficient, which depends on the PA laser detuning, weakly depends on temperature ($\propto T^{-1/2}$), and specific properties of the excited state v^* (see Sec. 3.4).

The form of eq. 3.1 gives us a rough guide for how to perform a PA spectroscopy experiment: We want to squeeze the atoms to the highest densities possible, illuminate them with as high-intensity PA light as possible, and look for simultaneous Na and Li loss while changing the PA laser frequency. Furthermore, we are interested in finding PA to triplet excited molecular states, thus the initial collisional state should have $S_{\text{tot}}=1$. This condition was easily fulfilled since evaporatively cooling in the magnetic trap leaves the atoms in the stretched states, Na $|F=2, m_F=2\rangle$ and Li $|F=3/2, m_F=3/2\rangle$. The two-body collisional state has the quantum numbers $|J=1, m_J=1\rangle$ where $J=N+S$ and $N=0$ since the atoms undergo only s -wave collisions at ultracold temperatures.

The magnetic trap frequencies were $\omega_{r,\text{Na}} = 2\pi \times 325 \text{ Hz}$, $\omega_{z,\text{Na}} = 2\pi \times 25 \text{ Hz}$ for Na. The atoms were cooled at a temperature of $T = 3.7 \mu\text{K}$ which corresponds to $T/T_c = 2.7$ and $T/T_F = 1$. Forming an Na BEC was purposely avoided since it would collapse the Na cloud to a small volume with poor spatial overlap with the Li atoms. These trap parameters corresponded to densities of $n_{\text{Na}} = 9 \times 10^{12} \text{ cm}^{-3}$ and $n_{\text{Li}} = 3 \times 10^{12} \text{ cm}^{-3}$. It was possible to achieve higher densities by running more current to the gradient coils to make a tighter magnetic trap, however three-body loss quickly became a limiting factor. The magnetic trap produced a small bias field,

$B_z = 1.2$ G.

The atoms were illuminated with the PA laser propagating along the long axis of the trap, such that the beam could be focused to a small spot and produce the largest PA intensities. Typical PA beam spot sizes had a $250\ \mu\text{m}$ waist, which was purposely larger than the typical cloud diameter of $50\ \mu\text{m}$, allowing for easier alignment¹. The PA light was linearly polarized, which maximized the chances of observing PA by allowing for σ^+ and σ^- selection rule transitions. The PA laser power was initially only 6 mW when we used an ECDL laser, but later we were able to use a Ti:Sapphire laser to send up to 600 mW to the atoms, allowing for much faster PA spectroscopy (see Sec. 2.4.1). When searching for a vibrational PA line, we would use the maximum laser power (600 mW) and sweep the laser at ~ 1 GHz over an exposure time of 3 seconds. Once a PA feature was found, finer scans were performed at much lower laser intensities to avoid line broadening and possible Stark shifts. After PA exposure, the surviving free Na and Li atoms would be counted via absorption imaging.

It is worth comparing our method of PA spectroscopy using an ultracold mixture to another technique accessible with our experiment: PA directly from a dual species MOT. In such an experiment the two MOTs are illuminated with PA light and trap loss is measured from the MOT fluorescence² [96, 97, 98, 99, 42]. We successfully implemented such a scheme to briefly study Li_2 PA, and found a clear MOT-loss signal using a lock-in amplifier with ~ 1 s integration times. The primary advantage of such a technique is experimental simplicity and improved duty cycle, potentially offering a factor of 30 in search speed compared to the ~ 30 s cycle time of ultracold atoms production. But there are a number of disadvantages which led us to use the ultracold mixture. First, the highest achievable MOT densities are $\sim 10^{10}\ \text{cm}^{-3}$, which would result in a factor of 100 lower PA rate than in an ultracold mixture. On top of this, theoretical calculations predicted very low NaLi PA couplings due to

¹When first looking for a PA signal, we would occasionally worry that the PA beam was too small and misaligned with the atoms from chromatic aberrations in the imaging path which was used for alignment. Hence, we made the PA spot size slightly larger than necessary.

²There are variations of this experiment which ionize the photoassociation products for detection (e.g. [95]), however this would need a significant modification of our current setup which does not have an in-vacuum microchannel-channel plate detector.

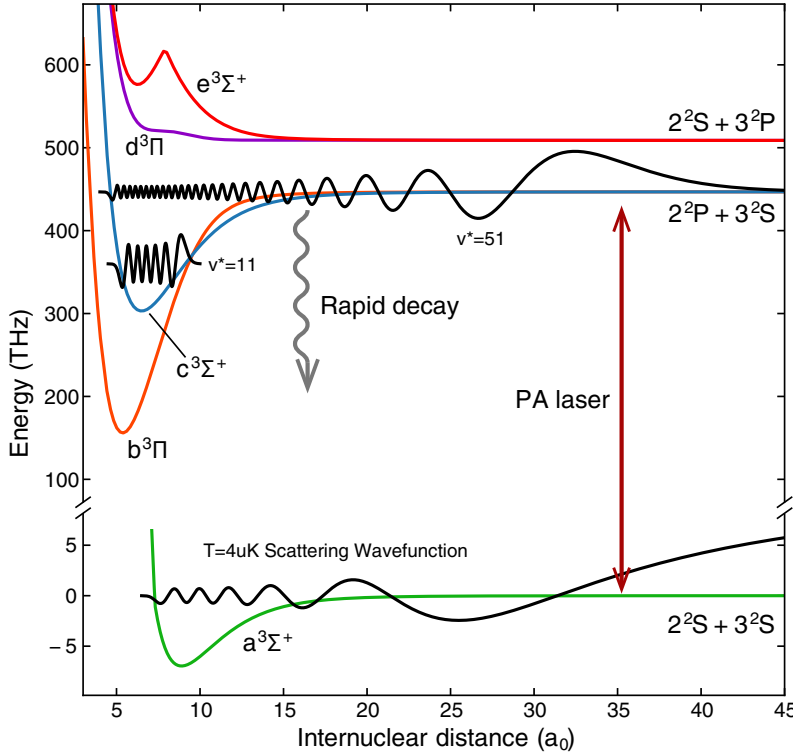


Figure 3-1: Photoassociation to NaLi triplet molecular potentials. The ground $a^3\Sigma^+$ and first excited triplet potentials of NaLi are drawn. All triplet molecular potentials connecting to an excited free Na atom are repulsive, and contain no molecular states. In the ground potential, the free Na and Li atoms collide with an ultracold scattering wavefunction. A photoassociation laser can excite the two atoms into an excited molecular state. The $v^* = 51$ state in the $c^3\Sigma^+$ potential was the first state we observed with PA spectroscopy. The $v^* = 11$ state in the $c^3\Sigma^+$ potential is the intermediate state which was used for STIRAP. After PA excitation, the excited molecular state quickly decays to other bound states or high kinetic energy scattering states, resulting in trap loss [94].

poor free-to-bound Franck-Condon overlap arising from the small C_6 coefficients in Na and Li [100]. With these considerations, we expected the high-density ultracold mixture to give a higher probability of finding a PA line. Another issue with using a MOT is the background homonuclear PA lines. Heteronuclear MOT PA spectroscopy in LiYb suffered from observing much stronger Li_2 PA near-dissociation, which had to be carefully subtracted to see the heteronuclear signal [42]. In our ultracold spin-polarized Na and Li mixture, homonuclear Li_2 PA is suppressed due to the fermionic nature of Li which prevents s -wave collisions at low temperatures. While Na_2 PA is

still possible, it would be rare since the NaLi molecular potentials we are interested in do not connect to the excited 3^2P Na asymptote.

3.2 Finding a first signal

In searching for NaLi photoassociation, we chose to use look for excited molecular states near the Li D line asymptote. Using the excited Na asymptote was never an option, as all connecting triplet potentials were repulsive and without any bound states (Fig. 3-1). Searching for near-dissociation states gave us a smaller search window, since the vibrational level spacing near-dissociation is only ~ 100 GHz, as opposed to ~ 5 THz for deeply bound excited states. Furthermore, near-dissociation states typically have the strongest PA transitions because of their large size: The Franck-Condon factor is dominated by the contribution at the turning points of the bound molecular wavefunction (called the Condon points), and states with larger turning points would better overlap with the large, slowly varying ultracold scattering wavefunction. The disadvantage to searching for near-dissociation PA lines was off-resonant Rayleigh scattering of the PA light to the Li atoms, which heats the ultracold sample and limits the maximum PA exposure time.

With these ideas in mind, we began the search for a PA signal 40 GHz below the Li D1 line, where we could achieve 1 second exposure times using the full power of an ECDL (~ 6 mW). The raw data for the first PA signal we observed is shown in Fig. 3-2, which we later determined to be $v^* = 51$ of $c^3\Sigma^+$, shown in Fig. 3-1. The clear signature of PA was the simultaneous loss of both Na and Li species under the illumination of light, which was double checked by observing no effect using an initial sample of Na or Li only. The effect of Rayleigh scattering is clearly visible at high PA frequencies, which resulted in Li number loss and partial Na loss due to collisions between the species. A finer scan of this PA feature reveals line splitting and finer sub-structure; these effects are discussed in the following section and here we only discuss the vibrational structure.

After observing this single PA feature, we continued downward in PA frequency

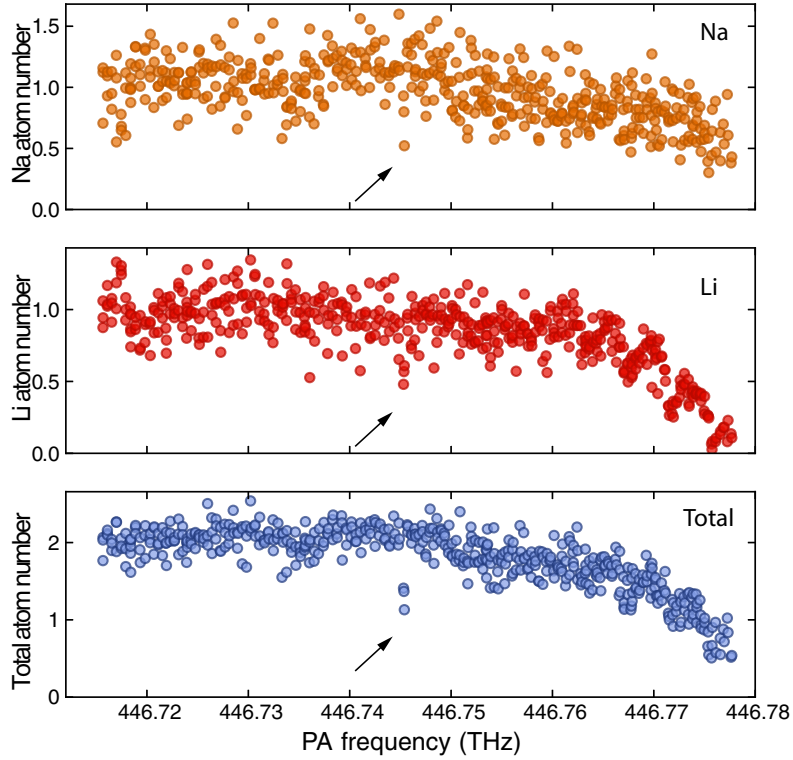


Figure 3-2: First signal of photoassociation. The arrows point to a loss in both Na and Li number, indicative of PA. This state would later be identified as $v^* = 51$ in the $c^3\Sigma^+$ potential. The signal is visible in both Na and Li, however the total atom gives a much cleaner signal. The loss of Li due to Rayleigh scattering is clearly visible for PA laser frequencies closer to the Li D1 line. The atom numbers are normalized to their peak values.

looking for deeper states. Our prediction of where to search for the next state was determined using the Leroy-Bernstein near-dissociation expansion, which provides a simple model for highly-excited vibrational state spacing based on the WKB approximation [101]:

$$E_b = - \left[A \frac{(v_D^* - v^*)}{C_6^{1/6}} \right]^3, \quad A \equiv 2\hbar \sqrt{\frac{2\pi}{\mu} \frac{\Gamma(7/6)}{\Gamma(2/3)}} \quad (3.2)$$

where E_b is the vibrational state binding energy, μ is the reduced mass, C_6 is the van der Waals coefficient, and v_D^* is a free fitting parameter which can be interpreted as the fractional vibrational quantum number at dissociation. After the observation of one PA line, we used a theoretical value for C_6 [102, 103] to find the parameter v_D^* and obtain a prediction for the position of the following state. After finding two lines, we

would then fit their positions to eq. 3.2 to get a better prediction for the subsequent line, and thus “bootstrap” the PA spectroscopy. Note that the C_6 values for all molecular potentials dissociating to the Li 2^2P asymptote are the same [102, 103], and from the Leroy-Bernstein analysis alone it was not yet possible to tell which excited potential we were probing (either the $b^3\Pi$ or $c^3\Sigma^+$ potential). This would be determined later, when a large collection of spectroscopic lines could be compared to *ab initio* calculations³. The *ab initio* potentials are notoriously inaccurate for near-dissociation states, and we relied primarily on the Leroy-Bernstein analysis to make spectroscopic predictions for highly excited vibrational states.

Fig. 3-3 shows the result of fitting eq. 3.2 to the binding energies of highly vi-

³It is possible to determine the excited molecular potential from selection rule differences between Σ and Π states, or perhaps by a careful examination of the PA fine-structure. At the time, we were more interested in finding deeper triplet PA lines for use in STIRAP.

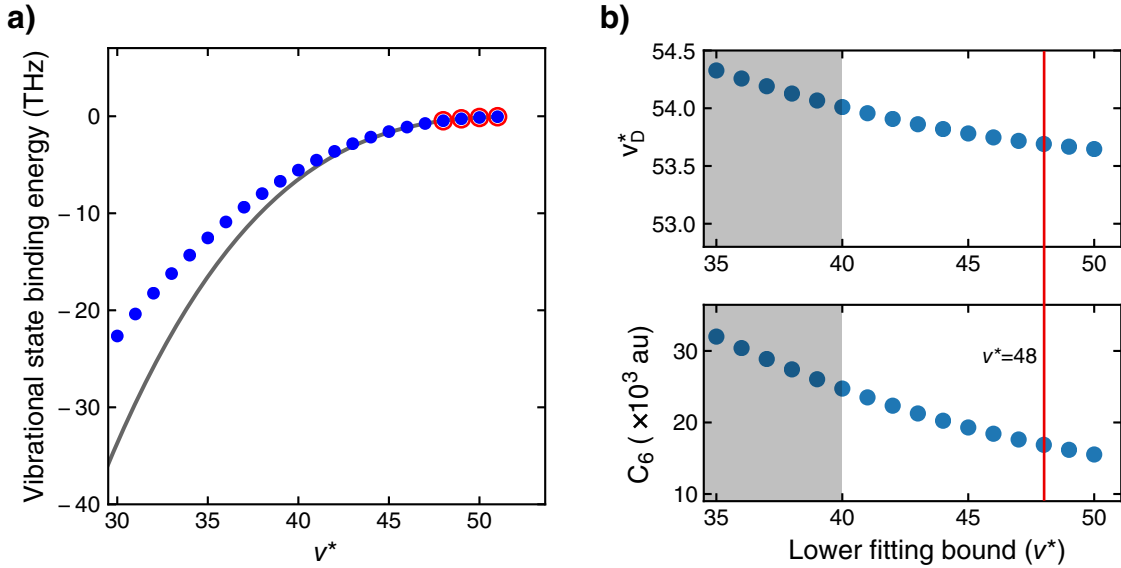


Figure 3-3: Leroy-Bernstein expansion predictions. a) Experimental PA line positions are shown with blue circles. A Leroy-Bernstein fit (eq. 3.2) of the 4 highest vibrationally excited PA lines (red outlines) is shown as a gray line. The resulting Leroy-Bernstein fit (grey line) shows worse deviation from measured values at deeper vibrational states. b) Fitting parameter values (v_D^* , C_6) for different depths of fitted data (from $v^* = 51$ down to a lower fitting bound). The fits become unphysical in the gray area where $v_D^* > 54$, since that would imply the existence of another bound state. Based on the Leroy radius (see text), the most physically meaningful fits were for the data points $48 \leq v^* \leq 51$.

brationally excited states, which was used to predict the positions of deeper bound levels. The fitting parameters become less meaningful when fitting a deeper range of bound states (Fig. 3-3 b). The range of validity for a Leroy-Bernstein analysis is given by molecular states larger than the Leroy radius, $R_{\text{LR}} = 2 [\langle r_{\text{Na}}^2 \rangle^{1/2} + \langle r_{\text{Li}}^2 \rangle^{1/2}]$, where r refers to the atomic radii of the Na and Li atoms [104]. In NaLi we estimate $R_{\text{LR}} \approx 25a_0$ based on hydrogen wavefunctions with a simple quantum defect modification. By calculating outer-turning points from *ab initio* potentials we find that only the states $v^* \geq 48$ are larger than R_{LR} , and using a Leroy-Bernstein fit on these states gives $C_6 = 16880$ au, in agreement with theoretical predictions [102, 103]. Near-dissociation fits of deeper bound states are possible with higher order corrections to the Leroy-Bernstein formula as discussed in [105]. In our case, it was difficult to extract meaningful physical parameters with higher order corrections since the C_6 contribution alone predicts deeper bound states than we observed (see Fig. 3-3 a), and additional potential terms such as $-C_8/r^8$ that further deepen the potential do not improve the fit quality. Instead we simply appended eq. 3.2 with a Taylor series, $E_b = a_3(v_D^* - v^*)^3 + a_4(v_D^* - v^*)^4 + \dots$, which provided a useful fitting function in search of bound states but without physically meaningful parameters. As we searched towards deeper vibrational states ($v^* < 30$) we began using the *ab initio* potentials as guidance rather than a near dissociation approach⁴.

3.3 Spectroscopic line positions

As the spectroscopic search proceeded to deeper bound states, near-dissociation expansions became poor predictors of PA line position, and we relied on the *ab initio* potentials. At this point it became very clear we were observing PA to the $c^3\Sigma^+$ potential⁵, and we could definitively assign vibrational quantum numbers to the ob-

⁴Finding PA line positions using *ab initio* potentials was done by either scaling the potential functions or spline-fitting the error between already found PA lines and *ab initio* predictions. The exact method didn't matter, since after we found the first ~ 15 lines any smooth fit to the data produced a reasonable prediction.

⁵Of course, we compared the near-dissociation state spectra to *ab initio* potentials very early in the search process as well, and had hints that we were probing the $^3\Sigma$ potential.

served spectra. The *ab initio* potentials were accurate to 2 % for deeply bound states ($v < 49$), which corresponds to a ~ 600 GHz prediction uncertainty. Such an uncertainty was still much too large to find PA lines quickly (the typical single-shot sweep width was 1 GHz exposed over 3 s for broad searches with the Ti:Sapphire laser), and narrower search windows of 30 GHz were obtained by fitting a smooth spline to the error in the *ab initio* predictions.

Using this method, we were able to find 50 out of 54 vibrational states in the $c^3\Sigma^+$ potential. Their vibrational quantum number assignment was determined by comparison to the *ab initio* predictions. Their rotational quantum number is $N^* = 1$, which is determined by the selection rule $\Delta N = 1$ for $\Sigma \leftrightarrow \Sigma$ transitions. Fig. 3-4 shows a sample spectrum from the $v^* = 11$ PA line. The spectra were fit to Lorentzian

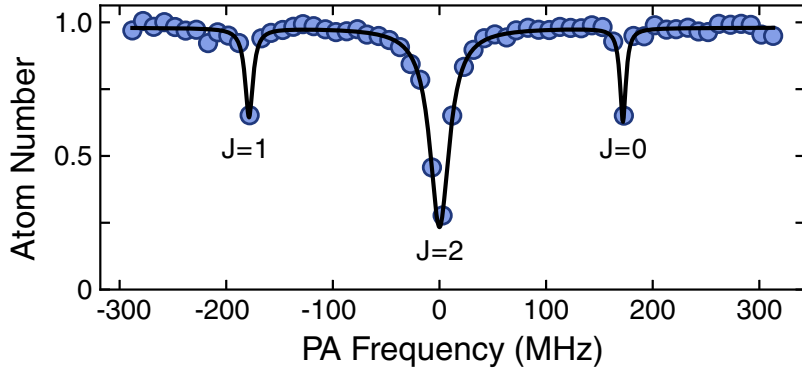


Figure 3-4: A sample PA spectrum of the $v^* = 11$ excited vibrational state. Three finely split lines were observed, which were later determined to be different angular momentum (J) states of the excited molecule. The loss spectra was fit to Lorentzian lineshapes.

lineshapes and the centers of the fits were used to determine the spectroscopic line position. The linewidth of the PA resonances were determined by the Lorentzian width for spectra taken with low PA loss, such that broadening from the nonlinear density dependence of the PA strength (i.e. the n^2 dependence in eq. 3.1) could be neglected. This yielded an average PA linewidth of $\Gamma_{\text{PA}} = 9(3)$ MHz for all PA lines⁶. These fits, along with their resonant PA frequencies, are shown in Fig. 3-5.

⁶The PA linewidth could vary by factors of ~ 2 for different excited vibrational states [106],

All spectra displayed fine-structure on the order of 500 MHz, and the “center” of the vibrational structure was determined somewhat arbitrarily by visual inspection. The absolute laser frequency measurement was accurate to ± 10 MHz (see Chapter 2). The vibrational state binding energies were determined by subtracting the laser frequency from 446.789528 THz, which is the excitation frequency to the Li D1 line that connects to the $c^3\Sigma^+$ potential [107]. We observed no AC Stark shifts when taking PA spectra with different laser intensities. From the peak fitting uncertainty we estimate an upper bound for the AC Stark shift for all lines to be $< 0.1 \text{ MHz/W} \cdot \text{cm}^{-2}$.

Certain vibrational states were not found during PA spectroscopy. $v^* = 52, 53$ were too close to the Li D line, resulting in rapid one-body heating of the sample from the PA laser⁷. $v^* = 12$ is missing because the necessary PA frequency coincides with a water vapor absorption line, preventing the Ti:Sapphire laser from lasing. $v^* = 11, 12$ are two of the states with strong coupling to the triplet ground state, but having also found $v^* = 11$ we did not put in the effort to remove the humidity from the Ti:Sapphire cavity (with either vacuum or N₂ gas) to search for $v^* = 12$. Lastly, $v^* = 28$ was not found after searching only a modest 30 GHz range around its expected position. A possible explanation is the weak strength of this PA line (discussed in the next section). Another possible explanation is a perturbative shift of the line due to coupling to a different nearby molecular state⁸.

Based on our observed PA spectra, we performed a potential fit of the data which improved upon the *ab initio* potentials. The results and methodology of the potential fitting can be found in [58].

however we did not have sufficient data at low PA loss to measure the linewidth for each vibrational state.

⁷This in principle can be remedied by increasing the density of the atoms. The PA rate scales linearly with density, thus at high enough densities the resonant PA rate could be faster than off-resonant Rayleigh scattering.

⁸The likelihood of this could be estimated from the *ab initio* potentials by looking for any other molecular states that may be coincidentally nearby $v^* = 28$.

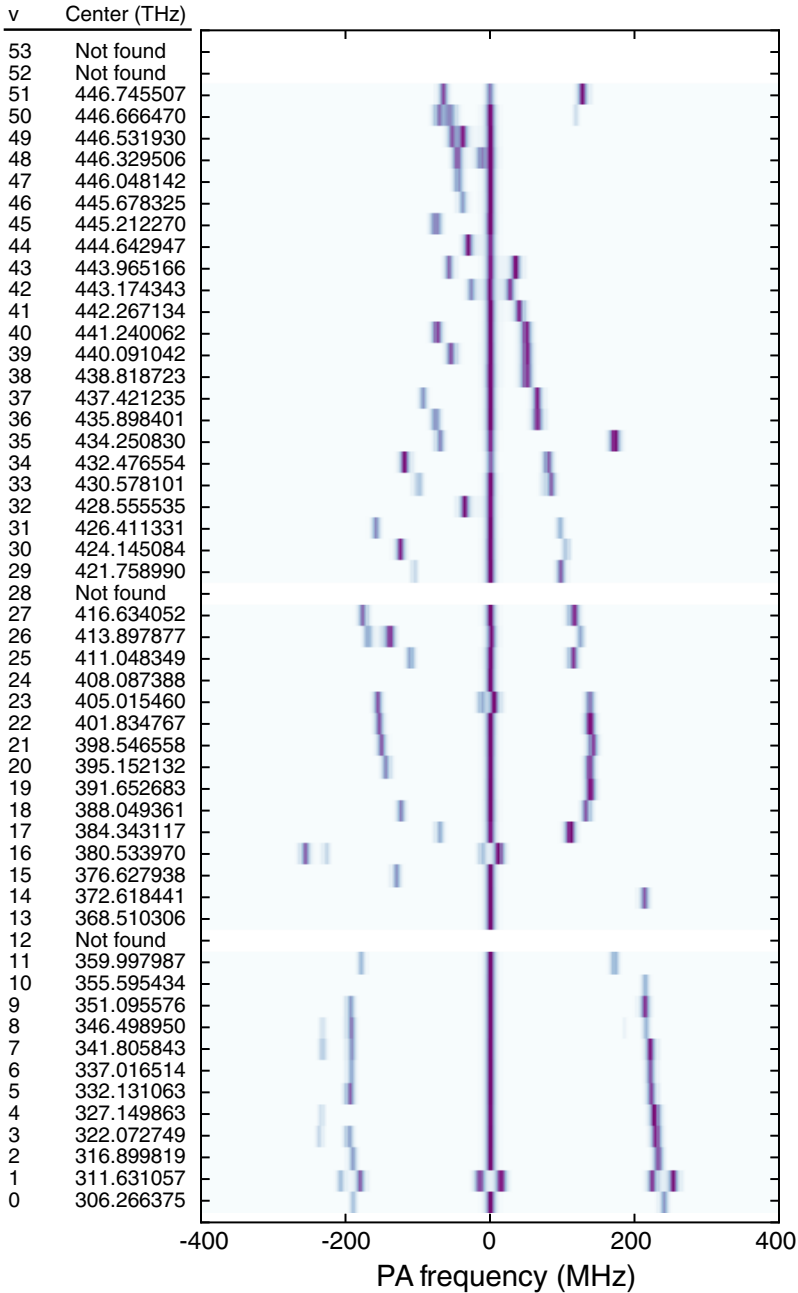


Figure 3-5: Spectroscopic frequencies and substructure for all observed states in the $c^3\Sigma^+$ potential. On the left are the resonant PA laser frequencies, which correspond to zero detuning in the structure diagram. The structure diagram shows the *fitted* data to all observed vibrational states. Since the observed PA linewidth can be broadened by density depletion, the structure diagram shows the results with linewidths set to $\Gamma_{\text{PA}} = 9$ MHz, the average measured value for all vibrational states. The substructure splitting becomes larger for lower v^* , which is consistent with fine structure interactions which become stronger for shorter internuclear separations.

3.3.1 $v^*=11$ fine structure

The $v^*=11$ state was expected to have the highest Franck-Condon overlap with the NaLi triplet ground state, and for this reason it would serve as the intermediate state for STIRAP (details in Chapter 4). Thus, we needed an understanding of the observed substructure in this state (Fig. 3-4). Experimentally, we could figure out the quantum numbers by performing PA with different polarizations. Starting with a $|J=1, m_J=1\rangle$, $N_g=0$ collisional state, the excited state structure could be uniquely determined by PA with different polarizations as shown in Fig. 3-6. Using this method,

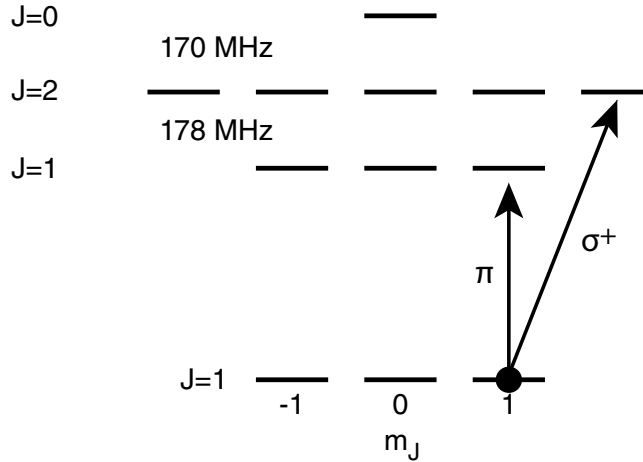


Figure 3-6: Polarization dependent PA of the $v^*=11$ state. The J ordering of the excited state was determined by applying different polarizations of PA light. The $J = 2$ state could be uniquely determined, as it is the only one which responds to σ^+ polarization. The $J = 0$ state could then be determined as it is the only one which would *not* respond to π light. Note that in order to produce π polarization, the PA beam was introduced to the atoms through a different beam path (the same beam path as for the bottom imaging).

we found the excited state had the peculiar energy ordering of $J = 1, 2, 0$. This is peculiar compared to the level splitting in alkali atoms, and cannot be explained by a simple $S \cdot N$ type coupling. Searching the literature revealed that a similar splitting was first observed in O₂ [108, 109], for which the triplet state is the absolute ground state⁹. This structure is explained mostly by a dipole-dipole (magnetic dipole)

⁹Triplet absolute ground states are not often found in nature (NaLi is certainly not one of them), and O₂ is a rare example. It turns out this plays a strong role in certain chemical reactions which

interaction between the valence electrons, along with a smaller contribution from spin-rotation coupling. The Hamiltonian for these interactions is given by

$$H_{\text{exc}} = \alpha \left(3(\vec{S}_1 \cdot \hat{r})(\vec{S}_2 \cdot \hat{r}) - \vec{S}_1 \cdot \vec{S}_2 \right) + \beta \vec{S} \cdot \vec{N} \quad (3.3)$$

where $\vec{S}_{1,2}$ are the individual electron spins, $\vec{S} = \vec{S}_1 + \vec{S}_2$, \hat{r} is the unit vector between the two electrons, and α, β are coupling constants. Note that we have not explicitly written out the r^{-3} dependence of the magnetic spin interaction, and the spatial average of this interaction term is contained in the α constant. There are two unknowns (α, β): we observe two splittings, and solving this model yields $\alpha = 182.1(1)$ MHz, and $\beta = 16.2(1)$ MHz, where the uncertainty is purely from measurement error.

The $v^* = 11$ NaLi fine structure is similar to O₂, however it has the opposite order for the J states. This difference can be intuitively understood based on the nature of dipole-dipole interactions and the different types of bonding in NaLi compared to O₂. The dipole-dipole interaction is attractive in the head-to-tail configuration, and repulsive in the side-by-side configuration. A triplet state has both electrons pointing in the same direction, and the position of each electron is determined by the bond geometry which is a σ bond in NaLi and a π bond in O₂. This is illustrated in Fig. 3-7, showing that the same spin configuration can have different dipole-dipole interaction energies in the NaLi and O₂ molecule.

Finally, it is worth commenting on the structure of other vibrational states of the $c^3\Sigma^+$ potential and the possibility hyperfine effects. It likely that vibrational states close $v^* = 11$ have a similar $J = 1, 2, 0$ fine structure (Fig. 3-5), but we have not carefully taken spectra with different PA polarizations for these lines and cannot make a definitive identification of quantum numbers. Some lines (such as $v^* = 1$) show similar three pronged structure along with finer doubling. This doubling is likely from hyperfine structure, which we have thus far not considered. Note that we have slight evidence that a similar doubling occurs in the $v^* = 11$ line, having observed a slight doublet structure in the $J = 2$ loss feature when we were probing PA with

also follow spin selection rules [110].

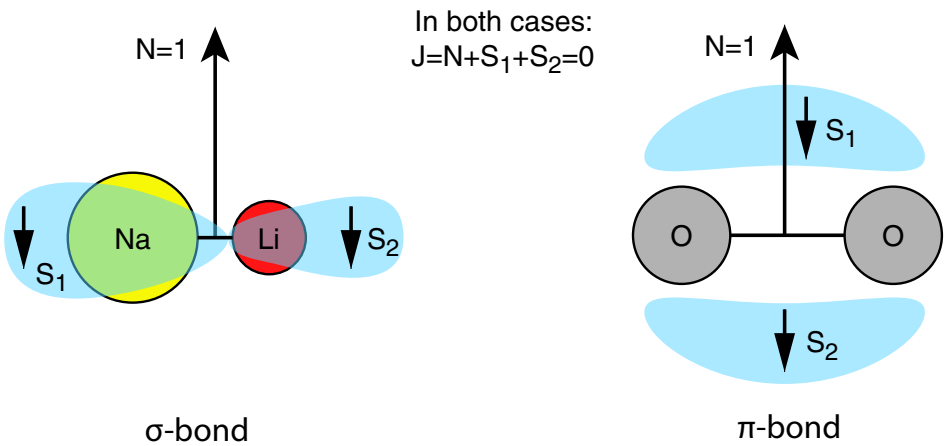


Figure 3-7: Comparison of electronic structures in NaLi and O_2 . Here, we graphically show the electron spin and rotational angular momentum orientations which result in the $J = 0$ state of both triplet NaLi and triplet O_2 . The angular-momentum vectors are drawn for intuition purposes only—they are not well defined and J is the only good quantum number. In NaLi, the σ bond results in repulsive dipole-dipole interactions between the electrons, which explains why the $J = 0$ state has the highest energy (see Fig. 3-6). In O_2 , the π bond results in attractive head-to-tail interactions, which lowers the energy of the $J = 0$ state. Hence, the ordering of the J states in triplet O_2 is opposite to that of triplet NaLi.

π polarization (but we did not take further measurements). Such small splittings are consistent with hyperfine effects. As a point of reference consider the atomic Li excited state hyperfine structure, which is only ~ 5 MHz. We expect similarly small values in the NaLi molecule. One may ask the question: how can we proceed with state-selective STIRAP without a clear determination of the hyperfine structure? The details of the states involved in STIRAP will be discussed in Chapter 5, but the short answer is by choosing the correct polarization of light, we will rely on stretched-state transitions which do not affect the nuclear spins. For example, the initial colliding Na and Li atoms have aligned nuclear spins, and if we perform PA with σ^+ polarized light, we excite the molecule to a $|J = 2, m_J = 2\rangle$ state and expect the nuclear spin state to be the same.

3.4 Line strengths

The PA strength was measured for each found vibrational state in the $c^3\Sigma^+$ potential. This was done by measuring the atom loss under illumination with resonant PA light as a function of PA pulse area. The total atom number density can be solved from eq. 3.1,

$$\begin{aligned}\frac{n(t)}{n(0)} &= \left(\frac{1-R}{1+R}\right) \left(\frac{1+Re^{\alpha It}}{1-Re^{\alpha It}}\right) \\ &= \frac{1}{1+n(0)\bar{K}It}, \quad \text{if } n \equiv n_{\text{Na}}(0) = n_{\text{Li}}(0),\end{aligned}\tag{3.4}$$

where It is the PA pulse area, $R = n_{\text{Na}}/n_{\text{Li}}(0)$ is the density ratio, $\alpha \equiv n_{\text{Na}}(0)(1-R)\bar{K}$, and in the second equality we show that the solution simplifies greatly in the case of equal Na and Li densities¹⁰. $n_{\text{Na}}, n_{\text{Li}}$ refer to average densities, which can be obtained from the atom number and an effective volume $V_{\text{eff}} = N_{\text{Na}}N_{\text{Li}}/\int n_{\text{Li}}n_{\text{Na}}dV$, where $N_{\text{Na}}, N_{\text{Li}}$ are the Na and Li total atom numbers, respectively¹¹. This loss model can be linearized if we assume the PA loss is small,

$$\frac{n(t)}{n(0)} \approx 1 - \frac{2n_{\text{Na}}n_{\text{Li}}}{n_{\text{Na}} + n_{\text{Li}}} \Big|_{t=0} \bar{K}It, \quad \alpha It \ll 1.\tag{3.5}$$

Using these loss models, the PA line strength was measured by tuning the PA laser on resonance and exposing the atoms for a variable pulse area. Fig. 3-8 shows such a measurement for the central feature in the $v^* = 11$ line. The PA loss was fit to eq. 3.4 and eq. 3.5 (for the region where $n(t)/n(0) > 0.7$), to extract the intensity normalized loss coefficient, $\bar{K}(v^*)$. The pulse area was varied by keeping the exposure time constant and ramping up the PA intensity. This procedure is slightly counterintuitive, since Fig. 3-8 “looks” like loss as a function of time, but it is not. The reason for

¹⁰This result is obtained using L'Hôpital's rule on the indeterminate term, $\lim_{R \rightarrow 1} \frac{1-R}{1-R \exp(n_{\text{Na}}(0)(1-R)\bar{K}It)}$. Equivalently, one can easily solve eq. 3.1 with $n_{\text{Na}}(0) = n_{\text{Li}}(0)$.

¹¹This definition accounts for differences in density profiles of the two species to give an effective overlap volume. In this experiment, both species were not quantum-degenerate and the gravitational sag was negligible. Thus to a good approximation $n_{\text{Na}}(\vec{r}) \propto n_{\text{Li}}(\vec{r})$, and $V_{\text{eff}} \approx \frac{N^2}{\int n^2 dV}$ where N, n refers to the number and density of either species.

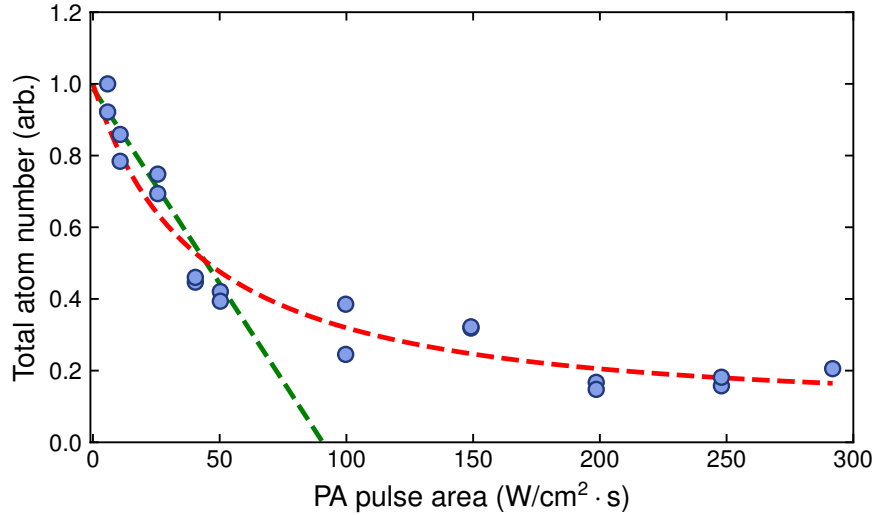


Figure 3-8: $v^* = 11$ PA line strength. The total atom number loss as a function of pulse area was measured with the PA laser on resonance to the $v^* = 11$ excited state. The data is fit to a full two-body model (eq. 3.4, red dashed line) and a linear model (eq. 3.5, green dashed line).

varying the PA intensity rather than exposure time was to sample PA loss at low laser intensities and avoid PA saturation, which can suppress the measured loss rate [111].

Such loss measurements were taken for each observed vibrational state for the central feature in its substructure (i.e. the zero-detuning line as defined in Fig. 3-5), and the results are shown in Fig. 3-9. $K(v^*)$ were measured from the average of the full loss curve (eq. 3.4) and the linear model (eq. 3.5) fits. The uncertainty in the $K(v^*)$ measurements has several contributions: (i) the variance between the two fitting methods, (ii) the inhomogeneous density variation throughout the trap, and (iii) a time-dependent density drop for long (> 3 s) hold times, which was attributed to technical heating of the sample (we suspect this was due to 60 Hz noise on the power supplies which near-resonantly coupled to the axial trap frequencies, $\omega_{z,\text{Na}} = 2\pi \times 25$ Hz and $\omega_{z,\text{Li}} = 2\pi \times 50$ Hz). The density increase from optical dipole trapping from the PA laser was considered in the analysis, but found to be negligible. In the limit of weak PA, the PA Rabi frequency Ω_{PA} can be obtained from the loss rate, $n\bar{K}I = \Omega_{\text{PA}}^2/\Gamma_{\text{PA}}$ where $\Gamma_{\text{PA}} = 2\pi \times 9$ MHz is the measured excited state linewidth.

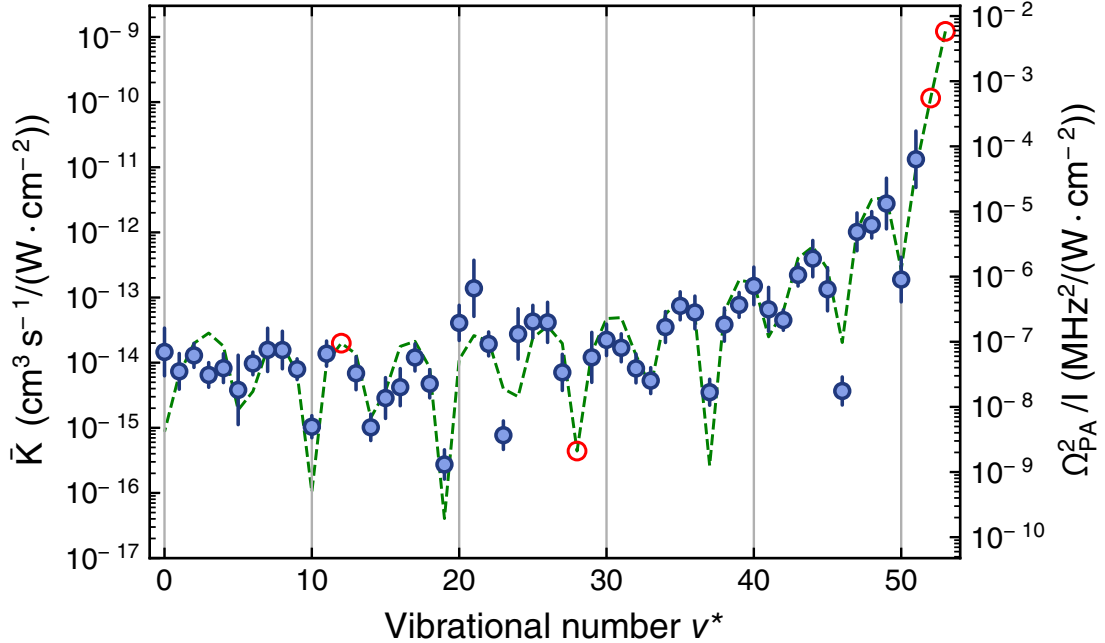


Figure 3-9: PA line strengths for all observed vibrational states. The density normalized PA loss coefficients were measured for each observed vibrational line. Solid blue points indicate measured PA strengths, while hollow red circles show the expected strength of PA lines we were not able to find. The data is fit to Franck-Condon factors calculated from *ab initio* potentials. The free-to-bound Rabi frequency, Ω_{PA} , was calculated from the PA loss coefficients assuming an excited state linewidth of 9 MHz and density of $n = 5 \times 10^{12} \text{ cm}^{-3}$.

Fig. 3-9 shows the expected free-to-bound Rabi couplings for densities of $n = 5 \times 10^{12} \text{ cm}^{-3}$ for both species.

Comparison of the PA strength measurements with theoretical values can be done to various degrees of first-principles rigor. A full treatment of PA theory can be found in [111, 112], with insights closer to experiments in [113, 114]. Here we outline a simple approach, which allows us to use Franck-Condon factors from the *ab initio* potentials to fit the strength data¹². We begin with the PA rate coefficient, which

¹²This allows us to ignore the normalization and thermal averaging of the scattering wavefunction in the free-to-bound transition, as well as the transition dipole matrix element of the molecule which is not trivial to calculate. As will be described, these parameters are all lumped into a single fitting constant.

must be proportional to the square of the coupling matrix element,

$$\begin{aligned}\bar{K}(v^*) &\propto |\langle \psi_{\text{mol}}(v^*) | D(R) | \psi_{\text{sc}}(E) \rangle|^2 \\ &\propto |\langle \psi_{\text{mol}}(v^*) | \psi_{\text{sc}}(E) \rangle|^2 \quad \text{if } D(R) = D_0\end{aligned}\tag{3.6}$$

where $|\psi_{\text{mol}}(v^*)\rangle$ is the excited molecular wavefunction, $|\psi_{\text{sc}}(E)\rangle$ is the ultracold two-body scattering wavefunction, and $D(R)$ is the coupling dipole moment, which varies as a function of internuclear distance in the molecule, R . In the second line of eq. 3.6 we've made the assumption that the dipole moment is a constant D_0 , which allows us to model $K(v^*)$ purely by the Franck-Condon factors, $|\langle \psi_{\text{mol}}(v^*) | \psi_{\text{sc}}(E) \rangle|^2$. Using the *ab initio* potentials, we numerically calculated the free-to-bound Franck-Condon factors and fit the strength data with the proportionality factor in eq. 3.6 as the only free parameter (Fig. 3-9). This simple model produces an excellent fit to the data, being remarkably accurate over 4 orders of magnitude in the PA line strengths. There is a simple interpretation of the PA strengths: The Franck-Condon factors are large for “large” excited molecules near-dissociation which have good overlap to the even larger ground state scattering wavefunction, and the overlap only decreases as the excited state molecules become smaller and more deeply bound. The sharp dips in the PA strengths are from nodes in the scattering wavefunction that overlap with the outer turning point of the excited state molecule, producing a very weak Franck-Condon factor. The Franck-Condon fit deviates slightly at low vibrational quantum number ($v < 6$), which may be explained by our assumption of a constant dipole moment: While the dipole moment $D(R)$ does not vary strongly with internuclear separation (typically by a factor of ~ 2 over all sizes of bi-alkali molecules, $R = 5 - 50 a_0$), the variation is strongest at short R , which exactly corresponds to deeply bound states [106, 115].

Chapter 4

Two-photon spectroscopy

Following the spectroscopy of excited triplet NaLi potentials discussed in the previous chapter, the natural next step was to perform two-photon spectroscopy of the ground $a^3\Sigma^+$ potential. The goal was to spectroscopically find the triplet ro-vibrational ground state ($v_g = 0, N_g = 0$ of the $a^3\Sigma^+$ potential). As with the excited triplet NaLi potentials, the ground potential was never previously observed in conventional photon fluorescence or absorption spectroscopy. Of all the bi-alkali species, NaLi was the only mixture without fluorescence spectra of the triplet ground states [116, 117, 118, 119, 120, 121, 122, 123, 124]. The reason for non-observation of the triplet ground states is once again the inability to prepare a triplet-character initial state in experiments involving hot gases, and the small mixing between triplet and singlet states in NaLi [85] (see Chapter 3). Observations of the triplet potential have been made possible with ultracold atoms experiments. The highest vibrational state of the $a^3\Sigma^+$ potential have been observed through Feshbach resonances to the $v_g = 10$ vibrational state [71, 54, 72]. To reach the next vibrational state with Feshbach spectroscopy ($v_g = 9$) would require fields in excess of 1 Tesla, making Feshbach spectroscopy of deeper bound states experimentally infeasible. Our focus was two-photon spectroscopy, which was the obvious approach given that the end goal was to perform STIRAP.

Although the lack of spectroscopic data was a challenge, spectroscopy and STIRAP to the triplet ground states of NaLi has a number of favorable features. The triplet ground potential is very shallow (~ 6 THz deep) and NaLi is a light molecule

with a low density of states, resulting in only 11 bound vibrational states in the triplet ground potential. Knowing the position of the least bound state from Feshbach spectroscopy, we could use a boot-strapped approach and start near-dissociation as we have done with the PA spectroscopy¹. Another advantage is that we can stay entirely within the triplet manifold, allowing for a simpler choice of intermediate excited state for the two photon spectroscopy (Fig. 4-1 a). Prior STIRAP experiments focusing on the singlet ground state were restricted to excited molecular states with singlet-triplet mixing (detailed discussions in [86, 125, 87]). In triplet NaLi it is much simpler—we choose an excited state which has the strongest Franck-Condon for STIRAP, i.e. with strong overlap to the ro-vibrational triplet ground state. In fact, finding a suitable intermediate state for a potential transfer to the *singlet* ground state of NaLi could be difficult. NaLi vibrational level spacings are large and the spin-orbit coupling is the weakest among the bi-alkalis, making “accidental” degeneracies between a singlet and triplet molecular states rare².

With our interest focused only on the triplet ro-vibrational ground state, we used *ab initio* calculations to determine that the $v^* = 11$ state of $c^3\Sigma^+$ was the ideal intermediate state for STIRAP. This choice of intermediate state will be discussed in more detail in Sec. 4.2, after a brief overview of the experiment setup.

4.1 Experimental approach

Experimentally, two-photon spectroscopy was a simple modification of the PA experiment described in Chapter 3. All of the experimental parameters (temperature, density, trap geometry, etc.) are the same, except we introduce another laser beam, known as the “downleg” laser, to search for bound-to-bound molecular transitions (Fig. 4-1). The entrance collisional state, an excited molecular state $|v^*\rangle$, and the a ground vibrational state $|v_g\rangle$ make a three-level system. There are two kinds of mea-

¹Note that the ground molecular states are so small in size that Leroy-Bernstein fits are not technically valid. This will be discussed further in Sec. 4.3

²Rare, but not forbidden. It is possible to use the improved potentials obtained in this thesis to look for singlet-triplet mixed excited states, though I have not made such an effort.

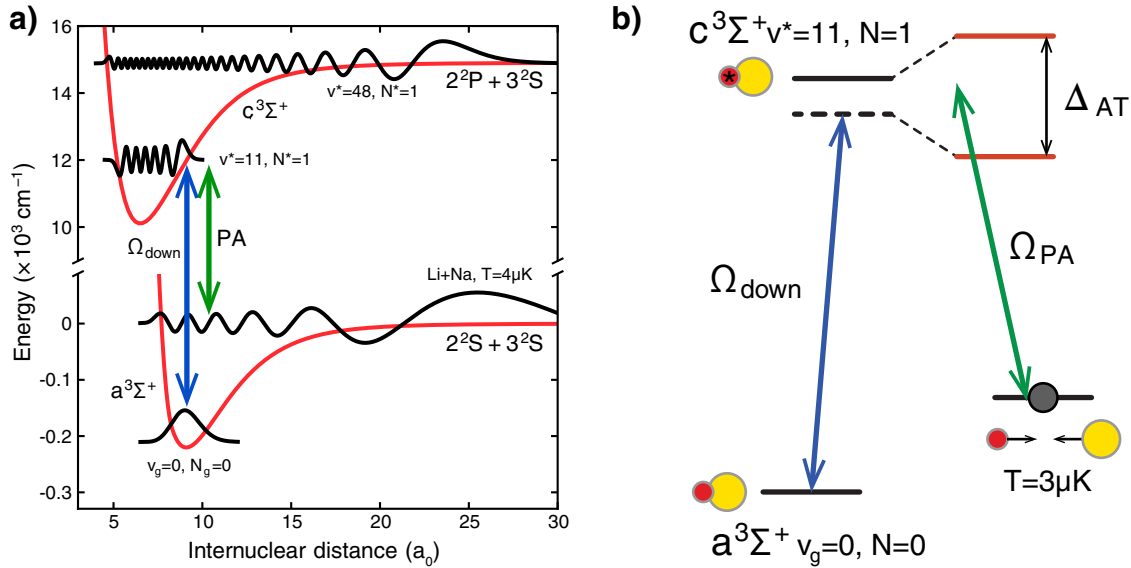


Figure 4-1: Molecular potential energy level diagram for two-photon spectroscopy. a) The relevant molecular potentials for spectroscopy of the triplet $a^3\Sigma^+$ potential. Drawn are the Na and Li ultracold collisional wavefunction, the excited intermediate wavefunctions, and the ro-vibrational triplet ground state wavefunction. b) An example three level system formed by the collisional state, the $v^* = 11$ intermediate state, and the ro-vibrational ground state. The downleg coupling dresses the intermediate state into two levels, resulting in an Autler-Townes splitting. This three-level system is qualitatively the same for other combinations of intermediate and ground vibrational states.

surements we performed on this system: (i) “dark-resonance” spectroscopy, which was most useful in spectroscopically finding the ground vibrational levels, and (ii) Autler-Townes spectroscopy, which was most useful in characterizing the bound-to-bound transition strengths.

Dark-resonance spectroscopy consists of keeping the PA laser on resonance with a known free-to-bound PA transition, and sweeping the downleg laser in search for a two-photon resonance. When the downleg laser is not resonant, we observe atom loss from the resonant PA laser coupling to $|v^*\rangle$. However, when the downleg laser comes close to a bound-to-bound resonance, it causes an AC Stark shift to the excited state $|v^*\rangle$, pushing it away from PA resonance (Fig. 4-1 b). This causes a suppression of PA which is observed as a rise in atom number at a particular downleg laser frequency, and in turn signals that we have found a bound-to-bound transition. This is known

as “dark-resonance” because the collisional state becomes dark to the PA light³. The binding energy of the ground molecular state is the difference between the PA and downleg laser frequencies on resonance. The width of the dark-resonance spectrum is proportional to the downleg laser intensity ($\text{Width} \propto I/\Gamma$), which is discussed in more detail in Sec. 4.4.

An Autler-Townes spectrum is the opposite configuration, where the downleg laser is kept on resonance and the PA laser frequency is swept. In this case the effect of the downleg laser is no longer a perturbative AC Stark shift, but rather a dressing of the excited state into two levels, $|v_g\rangle \pm |v^*\rangle$, which are split by the Rabi frequency Ω_{down} (Fig. 4-1). If $\Omega_{\text{down}} \gg \Gamma$, the PA laser frequency can be swept to probe these dressed states and find two distinct loss features. The spacing between the two loss features is exactly Ω_{down} (if the downleg is exactly on resonance), making for a clear measurement of the downleg Rabi frequency.

Dark-resonance and Autler-Townes spectra are two spectroscopic methods to probe the same physics of a three-level system. This connection is shown in Fig. 4-2, where the steady-state optical Bloch equations for a three-level system were numerically solved for various PA and downleg coupling strengths and detunings⁴ [126]. The excited molecular state undergoes rapid decay to unobserved states, thus the numerical solution for the excited state population also determines the loss lineshapes. Both the dark-resonance and Autler-Townes spectra can be understood by taking appropriate cuts through Fig. 4-2 a. The electromagnetically induced transparency (EIT) feature of Fig. 4-2 b will be experimentally discussed in Sec. 4.5.2 and in Chapter 5 with an initial state of Feshbach molecules. Note that these steady-state solutions used a slightly different excited state decay model than the one in our system: For a non-zero steady state solution to exist, the optical Bloch equations of [126] use a closed system which has an excited state that decays back to the two ground states

³This is the opposite spectroscopic signal compared to PA experiments, where a loss in atoms indicated resonance.

⁴The master equation in [126] has the form $\dot{\rho} = \frac{1}{i\hbar} [H, \rho] - D$ where ρ is the density matrix, H is the Hamiltonian, and D is the Lindblad form dissipation term. The steady-state solutions correspond to solving for ρ when $\dot{\rho} = 0$.

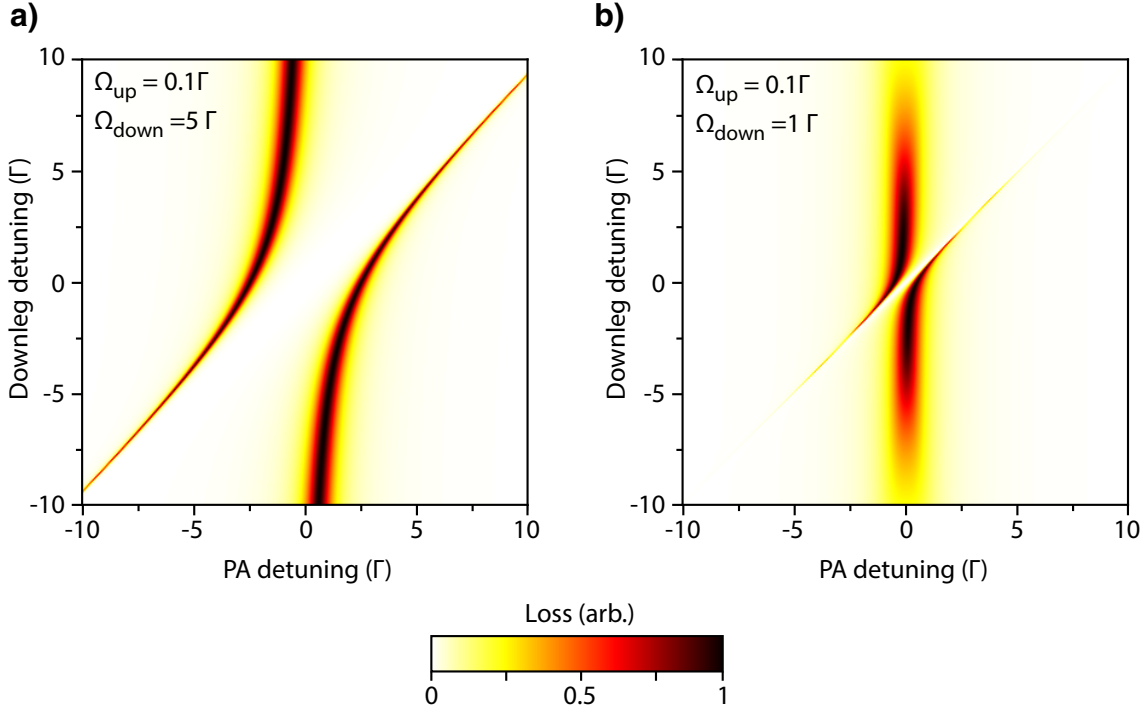


Figure 4-2: Simulated dark-resonance and Autler-Townes spectra. The excited (intermediate) state population is plotted as a function of PA and downleg detunings. Since the molecular excited state rapidly decays to unobservable states, the excited state population is proportional to loss. All detunings and Rabi frequencies are in units of Γ . a) The loss spectra for large downleg couplings. The dark-resonance feature is visible when varying the downleg detuning while the PA is on resonance. The Autler-Townes doublet is visible when varying the PA detuning while keeping the downleg on resonance. b) The loss spectra for small downleg couplings, showing a narrow suppression of loss on two-photon resonance corresponding to the formation of a coherent dark state between the collisional state and ground molecular state. This narrow suppression of loss is also known as electromagnetically induced transparency (EIT).

of the three level system. In our two-photon molecule spectroscopy experiment this is *not* the case, since the excited molecular state typically decays to other unobserved molecular states. This results in slight deviations between the simulation and our observations; for example, Fig. 4-2 b shows a slight decrease in loss for resonant PA at large downleg detunings, which corresponds to optical pumping into $|v_g\rangle$ in a closed system. This does not happen in the experiments, as resonant PA would result in complete loss of the atomic sample at steady-state.

The majority of two-photon spectra were taken in the dark-resonance configura-

tion, in order to find the 11 bound vibrational states. It is also possible to determine line strengths from the dark-resonance spectra, and this is discussed in more detail in Sec. 4.4. The downleg laser was an additional Ti:Sapphire (either at ~ 820 nm or ~ 670 nm depending on which intermediate state was used) which shared the same optical fiber and beampath as the PA laser, hence it had the same spot size ($250\ \mu\text{m}$ waist). The PA laser was the Ti:Sapphire laser (used in Chapter 3) when using an intermediate state near $v^* = 11$ (833 nm), and an ECDL (Toptica DL100) when using an intermediate state near $v^* = 48$ (670 nm). The simultaneous exposure to PA and downleg light had similar durations as in the PA spectroscopy, typically a few hundred milliseconds, until 50 % resonant PA loss was observed. The downleg laser was linearly polarized to allow for both σ^+ and σ^- selection rule transitions. The rotational selection rules for $\Sigma \leftrightarrow \Sigma$ potential transitions are $\Delta N = 1$, hence from a $N^* = 1$ rotational state it is possible to access both $N_g = 0, 2$ ground states. (As a reminder, the PA light only couples to $N^* = 1$ states from an initial $N = 0$ *s*-wave scattering wavefunction.)

4.2 Choosing a pathway to the ground state

Prior to performing two-photon spectroscopy, we used *ab initio* potentials to identify potential STIRAP pathways to the triplet ground state. We required an intermediate excited state with strong coupling to both the Feshbach molecules and to the triplet ground states. Fig. 4-3 shows the Franck-Condon factors calculated from *ab initio* potentials for different excited states of the $c^3\Sigma^+$ potential coupled to the ro-vibrational ground state and the Feshbach state. Since the ro-vibrational ground state wavefunction is a small Gaussian-like wavepacket (see Fig. 4-1), its Franck-Condon factors to excited states exhibit a very sharp peak. The Feshbach Franck-Condon factors show less drastic variations due to the large size of a Feshbach molecule, and look qualitatively the same as the previously studied PA strengths⁵ (Fig. 3-9). In a two-photon

⁵This similarity makes intuitive sense, as both the Feshbach state and a collisional state wavefunction look very similar at short range.

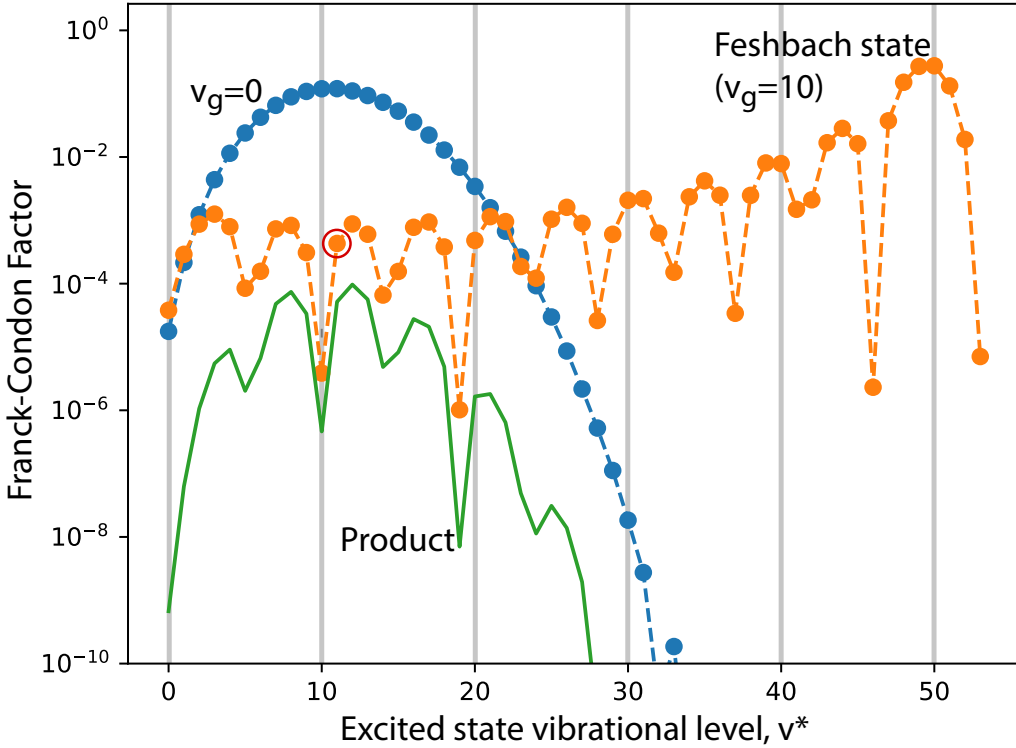


Figure 4-3: Franck-Condon factors for optimal STIRAP transfer. *Ab initio* potentials were used to calculate bound-to-bound Franck-Condon factors from the Feshbach molecule (orange) and the ro-vibrational triplet ground state (blue) to excited vibrational states of the $c^3\Sigma^+$ potential. The two-photon Rabi coupling is proportional to the product of these two Franck-Condon curves, and is shown in green.

process involving the Feshbach molecules, an intermediate excited state, and the ro-vibrational ground state, the two-photon coupling strength would scale as the product of the individual Franck-Condon couplings, $\Omega_{\text{two-ph}}^2 \propto |\langle \psi_{\text{mol}}(v_g=0) | \psi_{\text{mol}}(v^*) \rangle|^2 |\langle \psi_{\text{mol}}(v^*) | \psi_{\text{mol}}(v_g=10) \rangle|^2$, which is also shown in Fig. 4-3. The two-photon coupling is dominated by the sharpness of the $v_g=0 \leftrightarrow v^*$ transition strength. By inspection of Fig. 4-3, we chose the $v^*=11$ as the most likely candidate for STIRAP⁶, and for this reason the $v^*=11$ state is extensively used throughout this chapter.

⁶ $v^*=12$ was also a good choice, however we never found this state during PA. See Fig. 3-5.

4.3 Dark-resonance spectra: line positions

We found all 11 vibrational states of the $a^3\Sigma^+$ potential using dark-resonance spectroscopy, all with molecular rotational quantum number $N_g = 0$. We used a similar search method as with PA spectroscopy, first looking for weakly bound states and then moving down the potential. The $v^* = 48$ intermediate state was used to take spectra of states $v_g = 9, 10$, and the $v^* = 11$ state was used for spectra of $v_g = 0 - 9$. Fig. 4-4 shows sample dark-resonance spectra for the least bound state $v_g = 10, N_g = 0$ and the ro-vibrational ground state $v_g = 0, N_g = 0$. In all dark-resonance spectra we

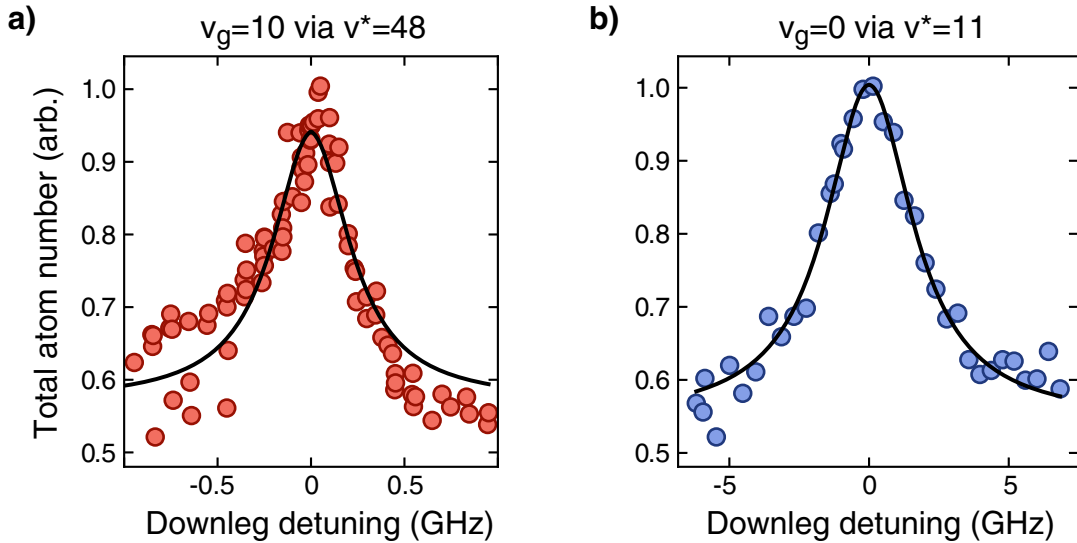


Figure 4-4: Sample dark-resonance spectra. The total atom number was monitored during resonant PA excitation, and a suppression of PA is observed when a downleg vibrational transition is found. a) A sample dark resonance spectrum for the least bound vibrational state. b) A sample dark-resonance spectrum for the ro-vibrational ground state. Both plots are fit to the lineshape model of eq. 4.4. The center of the fit determined the vibrational binding energy, and the width can be used to determine bound-to-bound transition strength (Sec. 4.4).

observed only one feature without any substructure. For spectra using the lower intermediate state, $v^* = 11$, we knew the angular momentum state of the PA transition to be $J = 2, m_J = 2$ (see Sec. 3.3.1), thus it made sense that only the corresponding stretched ground state $N_g = 0, J = 1, m_J = 1$ is coupled by the downleg laser, resulting

in only one dark-resonance feature⁷. For measurements using the higher intermediate state $v^*=48$, we did not make a careful determination of the PA substructure and cannot conclusively determine why only one dark-resonance feature was observed in the $v_g=9, 10$ spectra. This did not concern us, since our primary goal was to uncover the vibrational states of the $a^3\Sigma^+$ potentials and understand the $v_g=0$ state.

Table 4.1 gives the laser frequencies on two-photon resonance for each observed vibrational state, as well as its binding energy. The vibrational quantum numbers v_g

v_g	PA Frequency (THz)	Downleg Frequency(THz)	Binding Energy (GHz)
10	446.32951	446.33886	9.35(1)
9	446.32951	446.40187	72.36(1)
8	359.99798	360.23086	232.88(4)
7	359.99798	360.51511	517.13(3)
6	359.99798	360.93362	935.64(3)
5	359.99798	361.48861	1490.63(3)
4	359.99798	362.17836	2180.38(6)
3	359.99798	363.00098	3003.00(4)
2	359.99798	363.95290	3954.92(6)
1	359.99798	365.03180	5033.82(3)
0	359.99798	366.23614	6238.16(1)

Table 4.1: NaLi $a^3\Sigma^+$ vibrational state binding energies. The uncertainty stems from fitting dark-resonance features. In the case of $v_g = 10, 9, 0$, Autler-Townes spectra (see text) were used in binding energy determination. Autler-Townes spectra produce much narrower features, thus the uncertainty is limited by the wavemeter to 10 MHz.

were assigned based on comparisons with the *ab initio* potential, and all of our binding energy observations were within 3 % of the theoretical predictions [85]. We also searched below the ro-vibrational ground state without finding any dark-resonance, confirming that we observed the vibrational ground state⁸, $v_g=0$. The only prior measurement of the $a^3\Sigma^+$ potential was with Feshbach spectroscopy, which observed the least bound state at a binding energy of 9.35335(50) GHz, in agreement with our observation [72]. Selection rules on the downleg transitions allowed for angular

⁷This is only approximately correct. I mentioned earlier that both PA and downleg lasers have linear ($\sigma^+ + \sigma^-$) polarizations, hence the PA should also couple to the non-stretched $J=2, m_J=0$ state with σ^- polarization. However, in our measurements we found the σ^- transition to be much weaker than the stretched state transition (which is consistent with Clebsch-Gordon coefficients), thus I ignore this effect here.

⁸This search was 200 GHz wide, centered around the extrapolated line position based on a

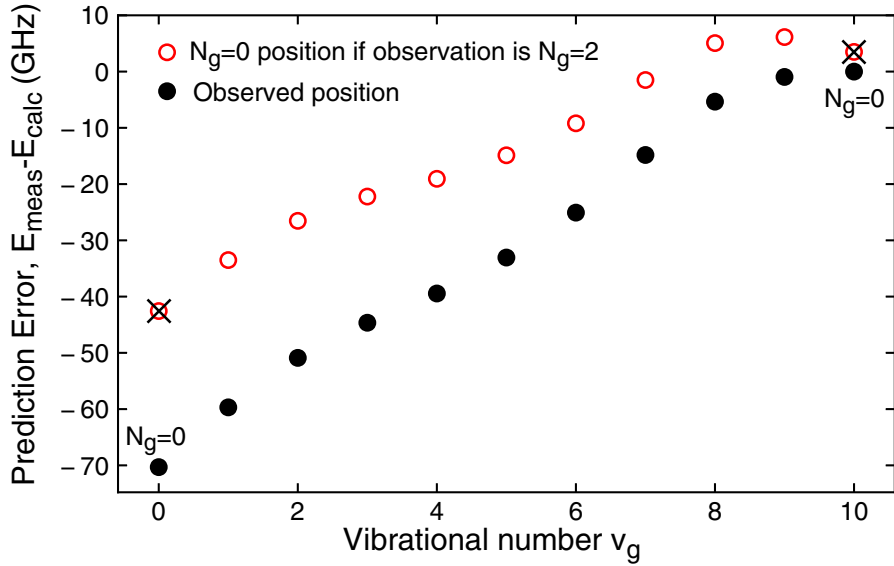


Figure 4-5: Comparison of $a^3\Sigma^+$ vibrational binding energies to theoretical calculations from the *ab initio* potential. Plotted is the difference between measured binding energy and theoretical binding energy, $E_{\text{meas}} - E_{\text{calc}}$, showing that the theoretical predictions generally predicted deeper bound states compared to the observations. Solid black circles show the observed line positions. The rotational quantum number $N_g = 0$ is certain for $v_g = 0, 10$. Hollow red circles show the *hypothetical* position of the $N_g = 0$ rotational state if one of the observations was a $N_g = 2$ state (the crossed out data points for $v_g = 0, 10$ indicate they cannot be true). Based on the smoothness of the observed data (solid black), we conclude that all of our observations are $N_g = 0$ states. (Consider the contrary by “swapping” a hypothetical and observed for a given v_g —this would result in a significant kink in the resulting black curve.) The rotational splittings here are calculated from the *ab initio* potential by adding an $N_g = 2$ centrifugal barrier to the potential.

momentum states of $N_g = 0, 2$. In NaLi, the $\Delta N_g = 2$ rotational splitting is $\sim 0.4\%$ of the binding energy, which is much too small to directly rely on *ab initio* potentials for quantum number assignment. Instead, N_g was determined as follows: for the least bound state $v_g = 10$, we knew $N_g = 0$ by comparison with Feshbach resonance spectra [72]. For the vibrational ground state, $v_g = 0$, we explicitly found the $N_g = 2$ state using dark-resonance spectra above the $N_g = 0$ state (discussed in the following section). For all other vibrational states in-between ($v_g = 1 - 9$), we inferred that $N_g = 0$ by comparing their binding energy to the *ab initio* prediction, and *not* observing any

harmonic-oscillator fit of the bottom of the $a^3\Sigma^+$ potential, i.e. at ~ 7.4 THz binding energy.

discontinuous jumps in the prediction error (Fig. 4-5).

Using the measured binding energies of these vibrational states, we constructed an improved potential curve using a full fitting procedure, described in [59]. Unlike the potential fitting of the excited $c^3\Sigma^+$ potential in Chapter 3, the Leroy-Bernstein near-dissociation fits are not a valid model for the states in the $a^3\Sigma^+$ potential because all of the vibrational states are too tightly bound. The Leroy radius gives a short-range length scale beyond which near-dissociation expansions become invalid (see Chapter 3). For NaLi, the Leroy radius is $25a_0$, and the only state larger than this in the $a^3\Sigma^+$ potential is the least-bound state with an outer turning point of $27a_0$. Even though there aren't enough states for a "proper" near-dissociation fit, the Leroy-Bernstein formula (eq. 3.2) was nonetheless useful as a fitting function during initial stages of two-photon spectroscopy, however the resulting values of v_D and C_6 were unphysical⁹.

4.3.1 Rotational splittings

We performed dark-resonance spectroscopy on the lowest vibrational state in the $a^3\Sigma^+$ potential to explicitly observe the rotational ground state ($N_g=0$) and the rotationally excited $N_g=2$ state. Fig. 4-6 shows the dark-resonance spectrum of the rotating molecule. As opposed to the rotational ground state dark-resonance spectrum, multiple features spanning 200 MHz were observed. This is to be expected from the extra multiplicity in an $N_g=2$ rotational state, which is likely complicated by $S \cdot N$ and $S_1 \cdot S_2$ coupling in a triplet molecule as observed in the excited states (Sec. 3.3.1). We attempted to identify the quantum numbers in the ground state by using different rotational states of the $v^*=11$ intermediate state, and observing the resulting observed ground states in accordance with selection rules. The results are thus far inconclusive¹⁰. The data is presented as-is for the benefit of future work with NaLi molecules, which may require a thorough understanding of the rotational

⁹It's likely we could have used any fitting function with reasonable success, but it was nice to use a function with some physical reasoning behind it. For example, in Fig. 4-5 the *ab initio* prediction error was on occasion fit to a power series to predict positions of neighboring vibrational levels.

¹⁰There is no fundamental reason for this—simply further work is required.

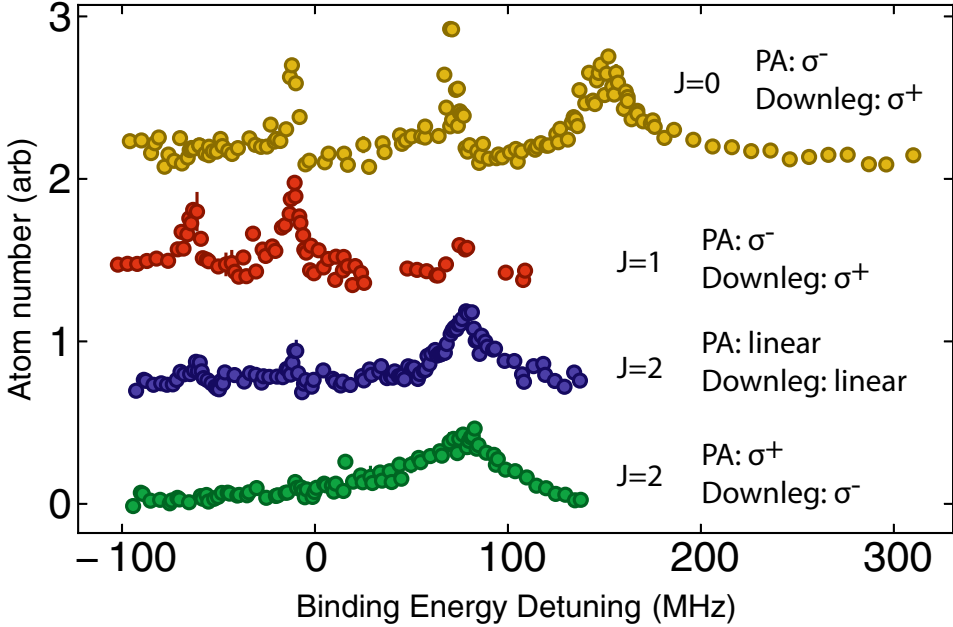


Figure 4-6: Dark-resonance spectrum of rotationally excited NaLi, $v_g = 0$, $N_g = 2$. Different angular momentum (J) states of the $v^* = 11$ intermediate state (see Fig. 3-6) were used in attempting to determine the quantum numbers of the $N_g = 2$ ground state. Different laser polarizations were used; linear refers to $\sigma^+ + \sigma^-$ polarization. The spectra show only the small step-size “fine” scans, and in the bottom three spectra no structure was observed where there are no datapoints (i.e. at detunings > 100 MHz). Zero detuning corresponds to 27.7 GHz above the $N_g = 0$ state, and higher detuning means lower molecule binding energy.

splittings to polarize the molecule dipole moment using a resonant microwave field [127, 128, 129].

Even without a clear understanding of the fine structure in the $v_g = 0, N_g = 2$ state, we can estimate the rotational constant of the molecule. The splitting between the $N_g = 0$ and $N_g = 2$ state is measured to be 27.7(1) GHz, in agreement with the *ab initio* prediction of 27.74 GHz. The error in our measurement stems from the spread of the fine structure in the $N_g = 2$ spectra and the inability to properly define a center-of-mass position without knowing the quantum numbers involved. This splitting can be used to determine the rotational constant in a simple rigid rotor model, $E_{\text{rot}} = BN(N + 1)$, from which we obtain $B = 4.63(2)$ GHz for this $v_g = 0$ state.

4.4 Line strengths

4.4.1 Autler-Townes spectra

We have so far discussed the spectroscopic positions of the two-photon dark-resonance spectra. Fits of the dark-resonance lineshapes can also be used to measure the bound-to-bound downleg transition strengths. Before moving forward with careful analysis of the dark-resonance lineshapes, it is worth considering the other spectroscopic configuration possible in a three-level system: observation of the Autler-Townes splitting by holding the downleg laser on resonance and varying the PA laser frequency (Fig. 4-1 b). When the downleg laser is resonant, the Autler-Townes splitting is exactly the downleg Rabi frequency. This makes for a very straight-forward method of measuring bound-to-bound coupling strengths. Furthermore, the limiting case of Autler-Townes spectroscopy with a weak downleg laser can result in EIT, which we will discuss in the next section.

Fig. 4-7 shows a sample Autler-Townes spectrum of the ro-vibrational ground state for various powers of the downleg laser. The downleg coupling splits the original PA

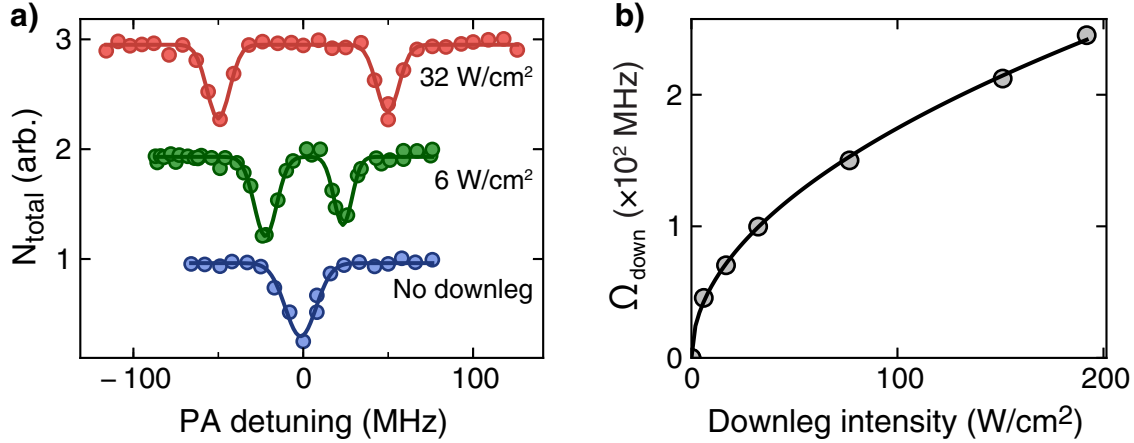


Figure 4-7: Autler-Townes spectrum of the ro-vibrational ground state. a) Shown are PA spectra of the central feature in the $v^* = 11$ vibrational state, using different intensities of downleg light resonant to the $v_g = 0 \leftrightarrow v^* = 11$ transition. The presence of downleg coupling splits the PA feature into two loss features separated by the Rabi coupling Ω_{down} . b) The Autler-Townes splitting as a function of downleg laser intensity, fitted to $\Omega_{\text{down}} \propto \sqrt{I_{\text{down}}}$, where I_{down} is the intensity of the downleg laser.

feature into two, corresponding to the two diagonalized states of the bound-to-bound system $|v^*\rangle \pm |v_g\rangle$. The states are split by the downleg Rabi frequency, which is proportional to the square root of the downleg laser intensity, $\Omega_{\text{down}} \propto \sqrt{I_{\text{down}}}$ as shown in Fig. 4-7 b. The Rabi splitting achieved in the $v_g=0 \leftrightarrow v^*=11$ transition are on the scale of hundreds of MHz with only a few mW of laser power. This large splitting is to be expected, as we've specifically chosen the $v^*=11$ intermediate state for its high Franck-Condon overlap to the ro-vibrational ground state. Such Autler-Townes spectra were taken only for the $v_g=0, 9, 10$ states. Aside from measuring the downleg Rabi frequency, they also allowed for a more precise determination of the vibrational state binding energies. Any downleg detuning would show up in the Autler-Townes splitting as a generalized Rabi frequency, $\Omega_{\text{gen}} = \sqrt{\Omega_{\text{down}}^2 + \Delta_{\text{down}}^2}$ and also cause a slight asymmetry in the Autler-Townes splitting relative to the original single PA feature (Fig. 4-7 a shows the resonant symmetric splitting, but off-resonance the Autler-Townes peaks simply move left or right relative to the original PA feature, as can be seen in the simulated spectra of Fig. 4-2). By changing the downleg frequency until this asymmetry disappeared, we could more precisely determine the vibrational binding energies compared to the broad dark-resonance spectra. This precision is reflected in the uncertainties in Table 4.1 for $v_g=0, 9, 10$, which is limited only by the wavemeter performance¹¹ to ± 10 MHz. The reason Autler-Townes spectra were more precise than dark-resonance spectra in determining the molecular binding energies is purely technical. The dark-resonance spectra were taken with the highest possible downleg intensity (large Ω_{down}) to maximize the probability of finding a ground vibrational state, hence the dark-resonance lineshapes were very broad ($\sim \Omega_{\text{down}}^2/\Gamma$) in comparison to the two Autler-Townes features with widths of Γ . In principle the same level of precision could be achieved with dark-resonance spectra if a smaller downleg coupling was used (as in the narrow feature of Fig. 4-2 b).

¹¹As will be discussed in the next section, an Autler-Townes spectrum with very small downleg coupling can yield kHz level resolution of the ground state, however this is only *relative* precision, and we are still reliant on the wavemeter when reporting absolute values.

4.4.2 Dark-resonance lineshapes

While Autler-Townes spectra provide an elegant perspective into the physics of three-level systems, such spectra can only be studied when all of the resonant transition frequencies are known. Since our primary work was to discover these *unknown* transition frequencies, most of the collected data was in the dark-resonance configuration¹². We now turn our attention to determining Ω_{down} from a dark-resonance spectrum. In this case, the PA laser provides a loss mechanism which is suppressed by the AC Stark shift in the $v_g \leftrightarrow v^*$ transition. The loss induced by PA has been discussed in Sec. 3.4; with balanced Na and Li densities and weak PA loss, we use the linearized PA loss model, eq. 3.5, to get:

$$\frac{n(t)}{n(0)} \approx 1 - n(0)Kt, \quad (4.1)$$

where $K \equiv \bar{K}I$ is the density normalized loss coefficient, and $n(t) = n_{\text{Na}} = n_{\text{Li}}$ is the atom number density. The PA loss coefficient is given by [111]

$$K \propto \frac{\Gamma\Omega_{\text{PA}}}{\Delta_{\text{PA}}^2 + [(\Omega_{\text{PA}} + \Gamma)/2]^2} \approx \frac{1}{\Delta_{\text{PA}}^2 + (\Gamma/2)^2} \quad (4.2)$$

where Ω_{PA} , Δ_{PA} are the PA Rabi frequency and detuning, respectively, and Γ is the excited state linewidth (measured in Chapter 3 to be $\Gamma = 2\pi \times 9$ MHz). We have made the approximation that the PA Rabi frequency is well below saturation ($\Omega_{\text{PA}} \ll \Gamma$), which is justified by the PA line strength results of Sec. 3.4, where typically $\Omega_{\text{PA}} \approx 2\pi \times 1$ kHz¹³. The PA is tuned on-resonance making Δ_{PA} zero. However, we now consider a downleg coupling which causes an AC Stark shift to the PA transition,

$$\Delta_{\text{PA}} = \frac{1}{2} \left(\sqrt{\Delta_{\text{down}}^2 + \Omega_{\text{down}}^2} - \Delta_{\text{down}} \right) \approx \frac{\Omega_{\text{down}}^2}{4\Delta_{\text{down}}} \quad (4.3)$$

¹²Taking Autler-Townes spectra for all vibrational lines was a time-consuming possibility, but our focus was on studying the ground state and we chose to move on.

¹³One doesn't need the exact results of Sec. 3.4 to see this. Fermi's golden rule applied to PA predicts a loss rate of $\Omega_{\text{PA}}^2/\Gamma$, and typical experiments show loss in ~ 100 ms, yielding $\Omega_{\text{PA}} = 2\pi \times 1$ kHz.

where Ω_{down} , Δ_{down} are the downleg Rabi frequency and detuning, respectively. In the second step we've assumed $\Omega_{\text{down}} \ll \Delta_{\text{down}}$; even though our downleg Rabi frequencies are quite large (typically 100 MHz), the range of the dark-resonance spectra is even larger (a few GHz, as in Fig. 4-4), which makes this assumption valid¹⁴. Putting together eq. 4.3, eq. 4.2 and eq. 4.1, we get the dark-resonance lineshape fitting function

$$\begin{aligned}\frac{N(t)}{N(0)} &= 1 - \frac{n(0)Kt}{1 + (\Omega_{\text{down}}^2/(2\Delta_{\text{down}}\Gamma))^2} \\ &= \frac{A}{\Delta_{\text{down}}^2 + (\Omega_{\text{down}}^2/(2\Gamma))^2} + B\end{aligned}\quad (4.4)$$

where $N(t)$ is the remaining total atom number and A, B are fitting parameters¹⁵. Thus, the dark-resonance lineshape is a Lorentzian with width $\Omega_{\text{down}}^2/\Gamma$. The dark-resonance spectra for each vibrational state was fit to eq. 4.4 to determine Ω_{down} , as shown for $v_g = 0, 10$ in Fig. 4-4. The bound-to-bound transition strengths for all vibrational states obtained using this dark-resonance fitting procedure as well as the simpler Autler-Townes spectra are shown in Fig. 4-8. The dark-resonance spectra shows good agreement with the Autler-Townes results, verifying the validity of our fitting model.

The strength data is compared to theoretical Franck-Condon fits (the same model as eq. 3.6 in Sec. 3.4) showing good agreement. As expected, using the $v^* = 11$ intermediate state yields the strongest coupling to the ro-vibrational ground state, since the outer turning point of $v^* = 11$ is at the same internuclear separation as the $v_g = 0$ ground state. Interestingly, the coupling strength to the next state, $v_g = 1$, is 100 times weaker. This effect has a very satisfying explanation: the $v_g = 1$ state wavefunction is anti-symmetric with a single-node, therefore producing a very small overlap integral with the outer-turning point of the excited $v^* = 11$ state. Another interesting feature in the strength data is the sharp drop in Franck-Condon factor for the $v_g = 8$ state

¹⁴The purpose of this assumption is to have a simpler expression in eq. 4.4. Numerically, the exact form of eq. 4.3 doesn't significantly change the fitting results.

¹⁵More precisely in eq. 4.4, $A = n(0)Kt \left(\frac{\Omega_{\text{down}}^2}{2\Gamma} \right)^2$, and $B = 1 - n(0)Kt$, but we let these parameters float.

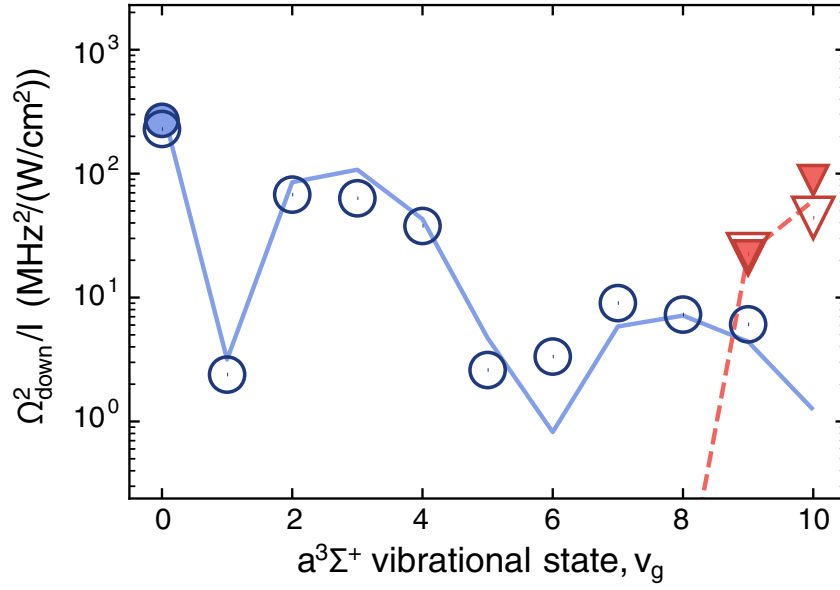


Figure 4-8: Bound-to-bound line strengths between vibrational states in $a^3\Sigma^+$ and $c^3\Sigma^+$. Hollow circles (triangles) show the coupling strengths measured from dark-resonance spectra with the $v^* = 11$ ($v^* = 48$) intermediate state by fitting with eq. 4.4. Solid circles (triangles) show line strengths measured by Autler-Townes spectroscopy. The dashed lines are fits from *ab initio* calculations of Franck-Condon factors. Note that the *ab initio* calculations are drawn as continuous lines for visual clarity, and they do not have any meaning for non-integer v_g .

using the $v^* = 48$ intermediate state, which explains why our attempts to observe the $v_g = 8$ state using the ~ 670 nm transition failed, necessitating the use of the deeper bound $v^* = 11$ intermediate state.

The line strength data from both dark-resonance and Autler-Townes spectra confirmed our hypothesis that the $v^* = 11$ state of the $c^3\Sigma^+$ potential was a good candidate for STIRAP. Moving forward, we knew that using a weak (mW) downleg laser and a strong upleg¹⁶ laser (300 mW) we could produce Rabi frequencies on the order of 10 MHz, which is more than sufficient for STIRAP transfer within a few dozen μ s (see Sec. 2.4.2 for STIRAP pulse time considerations).

¹⁶No longer called the “PA” laser, since the Feshbach-to- $(v^* = 11)$ transition is bound-to-bound.

4.5 Alternative paths to the triplet ground state

Within this chapter we have charted the course to the NaLi triplet ground state. In the next chapter, we apply this knowledge to coherently transfer Feshbach molecules into the ro-vibrational ground state, a technique which has become a sort of industry standard in ultracold molecules [35, 34]. But before moving forward, it is worth considering other methods of reaching the triplet ground state using our new found knowledge of NaLi triplet potentials and transition strengths.

4.5.1 Pumping

One possible method of forming triplet ground state NaLi is by optical pumping, i.e. using a photoassociation excitation followed by uncontrolled spontaneous decay, with the hope that some fraction decays into the ro-vibrational ground state. Such schemes have been successfully used in dual-species MOTs to form singlet ground state RbCs [124, 130], LiCs [131], NaCs [132], KRb [133] molecules and triplet RbCs [134] with formation rates of $\sim 10^4$ molecules \cdot s $^{-1}$ at temperatures of ~ 100 μ K. A unique variant of these experiments was the use of PA-pumping to access a highly excited vibrational state followed by STIRAP to the ro-vibrational ground state [135], thus avoiding the use of a Feshbach resonance. In all cases the ground state molecules were detected using resonantly enhanced two-photon ionization (REMPI) with a microchannel plate detector. These experiments offer the simplicity of working directly out of a MOT (no evaporative cooling, no Feshbach molecules) and the use of only one molecule formation laser (the PA beam). Their disadvantage is “cleanliness”: all ground state molecules are produced in an untrapped state surrounded by a cloud of atoms in the MOT. This makes it difficult to isolate a pure sample of single-state molecules, and hence the experiments typically report steady-state formation rates rather than trapped molecule number or lifetimes (since both of those quantities are very small).

In any case, it is intriguing to estimate the performance of triplet NaLi in such an experiment. Due to the light mass of NaLi and the shallow nature of the triplet $a^3\Sigma^+$ potential, there are only 11 triplet vibrational states. Thus a spontaneous decay from

a randomly chosen excited molecular state has a $\sim 10\%$ chance of falling into the $v_g=0$ state we're interested in. Of course, we can be more precise given the content of this chapter: careful inspection of Fig. 4-8 shows a vibrational branching ratio of $b=50\%$ from the $v^*=11$ excited molecular state to $v_g=0$. The total ground state molecule formation rate using PA excitation can be estimated from

$$R(v_g=0) = bn^2IV\bar{K}(v^*=11), \quad (4.5)$$

where R is the molecule formation rate, $b=0.5$ is the downleg branching ratio, n is the MOT density¹⁷, I is the laser intensity, V is the volume over which the laser illuminates the MOT, and $\bar{K}(v^*=11)$ is the PA rate coefficient which is given in Fig. 3-9. One must remember the temperature dependence of PA, $\bar{K} \propto T^{-1/2}$, and that the data in Fig. 3-9 was taken at $T=4 \mu\text{K}$. Assuming a MOT density of $n=10^{10} \text{ cm}^{-3}$, $T=100 \mu\text{K}$, a 1 W PA laser with a 0.5 cm diameter MOT¹⁸, we find the ground state production rate to be $R(v_g=0)=5\times 10^4 \text{ s}^{-1}$, on par with previous experiments using a MOT.

We can also estimate the formation rate if we employed the same pumping scheme but with an initial near-quantum degenerate Na and Li mixture used throughout this thesis. In this case the total atom number is $N=10^7$, the density is $n=5\times 10^{12} \text{ cm}^{-3}$, $T=4 \mu\text{K}$, and we suppose a 1 W PA beam illuminating a cigar shaped cloud with a $30 \mu\text{m}$ waist and 0.5 mm length. This yields a formation rate of $R(v_g=0)=2\times 10^8 \text{ s}^{-1}$, which would deplete the atomic sample in 20 ms to form 5×10^6 molecules. While this seems promising, it does not solve the problem of creating an impure molecular sample. Indeed, if we consider the typical universal loss rates (see Chapter 5 for details) for collisions of NaLi molecules with Na or Li to be $K_{\text{loss}}\approx 5\times 10^{-10} \text{ cm}^3/\text{s}$, the molecule lifetime would be ~ 3 ms, which poses an obvious problem for such a formation scheme. This illustrates the importance of having a clean molecular sample, and highlights why coherent, *state-selective* techniques such as Feshbach formation

¹⁷There are two MOTs involved, hence an overlap density would be required for a more exact calculation.

¹⁸The laser beam size drops out of the equation, since $IV = PL$ where P is the laser power and L is the length of the MOT.

followed by STIRAP are desired. Nonetheless, the discussion presented here serves as a starting point in considering new molecule formation schemes in which the problem of forming a clean molecular sample needs to be addressed.

4.5.2 Free-to-bound STIRAP

Chapter 5 will discuss in detail the use of Feshbach molecule formation and STIRAP to reach the NaLi triplet ro-vibrational ground state. Here, we briefly take the time to question one step of this process: is Feshbach molecule formation necessary? Feshbach formation provides a crucial coupling between free atoms and a molecular bound state, but why not simply use photoassociation? The short answer is that Feshbach molecule couplings and lifetimes are much more favorable compared to PA (Table 4.2). Comparing the free-to-bound coupling strength to the molecular state linewidth Ω/γ

	Feshbach formation	Photoassociation
Coupling Strength (Ω)	~ 1 MHz typical (e.g. [136]) 10 kHz in NaLi [54]	≤ 100 kHz (See Fig. 3-9)
Molecular State Lifetime (γ^{-1})	1 ms	10 ns
$\frac{\Omega}{\gamma}$	10^3 (10 in NaLi)	0.01

Table 4.2: Comparison of Feshbach resonances to PA. The Feshbach state lifetime is taken to be a typical value in a molecular sample *containing other atoms*, which is the kind of environment in which free-to-bound formation would be performed. Isolated Feshbach molecules have significantly longer lifetimes in accordance with the universal loss rate [43].

makes it clear that coherent formation is typically easier using a Feshbach resonance (here, Ω is the free-to-bound coupling matrix element and γ is a limiting decoherence linewidth). However, the technique of STIRAP transfers population between ground states of a three level system while *avoiding* the short-lived excited state. Thus the relevant decoherence timescale is no longer limited by the short spontaneous decay of an electronically excited molecular state, but is likely much longer, $\gamma^{-1} \gg 10$ ns.

Determining the decoherence limit γ is not an obvious procedure¹⁹, but it makes plausible the prospect of coherent control ($\Omega/\gamma > 1$) using PA in a STIRAP scheme.

Eliminating the use of Feshbach resonances using such a PA-STIRAP scheme would greatly simplify many experiments. Finding strong Feshbach resonances for molecular formation among different atomic species is a bit of a lottery: homonuclear ^6Li exhibits a 300 G wide resonance around which 100 % molecule formation is possible [137]. $^{23}\text{Na}^{40}\text{K}$ has a 30 G resonance with 15 % molecule formation efficiency [136]. NaLi had the unfortunate luck-of-the-draw to have 2 mG wide resonances, with formation efficiencies of only 5 % (the narrowest resonances used to make molecules to date [54]). Alkaline-earth species have no Feshbach resonances in their ground state²⁰, and Feshbach resonances using a meta-stable atomic state exhibit loss too rapid for any practical use [92]. A PA-STIRAP scheme gives freedom to choose an excited intermediate state, which could allow PA-STIRAP to be more widely applicable to other atomic species compared to Feshbach association.

This experimental simplicity of the PA-STIRAP scheme was appealing, despite the weak coupling strengths of PA. Even if poor molecule formation efficiencies of 0.1 % were achievable, this would correspond to the formation of 10^4 molecules, on par with Feshbach experiments. Recently such a PA-STIRAP scheme was demonstrated in a BEC of Sr, where the high densities in a BEC allowed for significantly improved Rabi frequencies ($\Omega_{\text{PA}} = 2\pi \times 3$ MHz) and a Sr_2 molecule formation efficiency of 9 % [138]. Another method to improve strength of the PA coupling is to produce very tight confinement for two atoms using an optical lattice, forcing the free atoms to within a small volume and increasing the free-to-bound Franck-Condon factor [139].

With all these considerations in mind, we decided to attempt a PA-STIRAP transfer to $v_g = 0$ using the $v^* = 11$ intermediate state. By this time we had already constructed the ULE cavity setup that locked the PA and downleg lasers to < 1 kHz

¹⁹Identifying the source of decoherence in a one-photon PA process is simple, since spontaneous decay is orders of magnitude faster than any other process. In a two-photon STIRAP process things become more complicated, as ground state molecular lifetimes and other decoherence processes such as magnetic-field jitter, sample temperature, laser linewidth, etc. all have similar timescales on the order of kHz.

²⁰This is not from any kind of lottery: Their ground state is a singlet 1S_0 state, which exhibits no magnetic tunability.

relative linewidth (see Sec. 2.4.1). With this high degree of coherence between the two lasers, the Autler-Townes spectra (Fig. 4-7) could be taken with very low down-leg couplings, $\Omega_{\text{down}} < \Gamma$ (here, Γ is the excited state linewidth, 9 MHz as measured with PA spectroscopy), resulting in electromagnetically induced transparency (EIT) [140]. Fig. 4-9 shows one such EIT spectrum using PA. The narrow feature indicates the formation of a coherent superposition of the triplet ro-vibrational ground state and the collisional scattering wavefunction, $\cos \theta |\psi_{\text{sc}}\rangle - \sin \theta |\psi_{\text{mol}}\rangle$ where the mixing angle is given by $\tan \theta = \Omega_{\text{PA}}/\Omega_{\text{down}}$ (see Sec. III D of [140]). Assuming infinitely

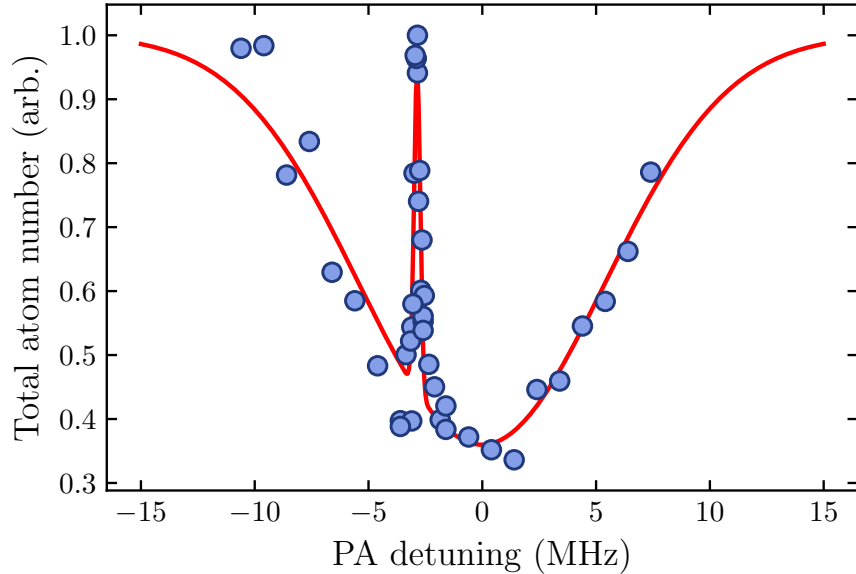


Figure 4-9: Free-to-bound electromagnetically induced transparency. A PA spectrum of $v^* = 11$ using a PA power of 300 mW (500 W/cm^2) and downleg power of 5 μW (0.01 W/cm^2). A sharp EIT feature with 200 kHz FWHM is observed. Note the feature is off-center from the PA loss minimum simply because the downleg laser was not exactly on resonance in this particular dataset. In this way we could determine relative detunings in our system down to the kHz level.

narrow lasers and a long ground state molecule lifetime, the width of the EIT feature is given by $(\Omega_{\text{down}}^2 + \Omega_{\text{PA}}^2)/4\Gamma$ [141]. In Fig. 4-9, the couplings are estimated to be $\Omega_{\text{down}} = 2\pi \times 2 \text{ MHz}$ (from measurements in Fig. 4-8), and $\Omega_{\text{PA}} = 10 \text{ kHz}$ (from measurements in Fig. 3-9), resulting in an expected EIT width of 100 kHz, roughly consistent with the measured width of 200 kHz in Fig. 4-9. This implies the forma-

tion of a coherent state, $|\psi_{\text{sc}}\rangle - 0.005|\psi_{\text{mol}}\rangle$, which corresponds to a population of $N_{\text{mol}} = N_{\text{atoms}} \cdot (0.005)^2 = 250$ ground state molecules.

Efforts to increase the molecular fraction were not successful. 300 mW was the maximum PA power available which limited the PA Rabi frequency to 10 kHz, and further reducing the downleg coupling only resulted in the disappearance of the EIT feature. Attempts at forward and reverse STIRAP pulses (discussed in more detail in Sec. 5.4) using a wide range of pulse durations and powers did not show any evidence of molecule formation. With a maximum PA coupling of 10 kHz, we expected to use STIRAP pulses longer than 1 ms for adiabatic transfer, although we also attempted shorter pulses where non-adiabatic inefficiencies in the STIRAP process were expected. It is possible that an unidentified source of decoherence limited the STIRAP pulse length; as will be discussed in Chapter 5, the STIRAP pulse lengths using Feshbach molecules were limited to at most 200 μs for reasons we have not fully understood. Another important consideration in PA-STIRAP is that the reverse STIRAP transfer from a molecular state to free atoms follows a Wigner threshold law from the continuous density of collisional states, and thus the reverse STIRAP pulse necessary for molecule detection is not 100 % efficient [138]. This is significantly different in molecules formed using a Feshbach resonance, which can be dissociated to free atoms with perfect efficiency because the dissociation process is a non-coherent, *spontaneous* process. Thus it is possible that 1 % molecule formation with PA-STIRAP is undetectable due to a compounded 1 % (or worse) reverse-transfer efficiency.

With all of these open questions regarding PA-STIRAP, we chose to move forward with Feshbach formation followed by STIRAP. In this way, we hoped to learn how to perform STIRAP in a bound-to-bound system, and perhaps in the future come back to the less intuitive case of free-to-bound STIRAP.

Chapter 5

Formation of triplet ground state molecules

In the last two chapters, we have discussed experiments to spectroscopically identify a two-photon pathway from Feshbach molecules to the ro-vibrational triplet ground state of NaLi. The Feshbach molecules themselves were an ongoing project when I joined the Ketterle group in 2010, with successful formation in 2012 [54]. In this chapter, all of these pieces are put together to make a pure sample of ultracold triplet ground state NaLi molecules. Fig. 5-1 shows the relevant molecular potentials and states used in coherently forming the molecules. Sec. 5.2 describes the formation of weakly bound Feshbach molecules, where we discovered a longer-than-expected Feshbach molecule lifetime. These molecules were then coupled to the ro-vibrational ground state with two-photons: an “upleg” laser (replacing the PA transition of the last two chapters) up to the $v^* = 11$ intermediate state, and a “downleg” laser down to the ro-vibrational ground state. The upleg and downleg laser frequencies are discussed in Sec. 5.3, where the spectroscopic results of Chapter 2 and 3 are applied to the specific case of Feshbach molecules at high magnetic fields. In Sec. 5.4 we describe the transfer and detection of molecules in the triplet ro-vibrational ground state.

Sec. 5.5 will delve into studying properties of the new molecular system we’ve created. Triplet ground state NaLi molecules are fermionic with a non-zero magnetic

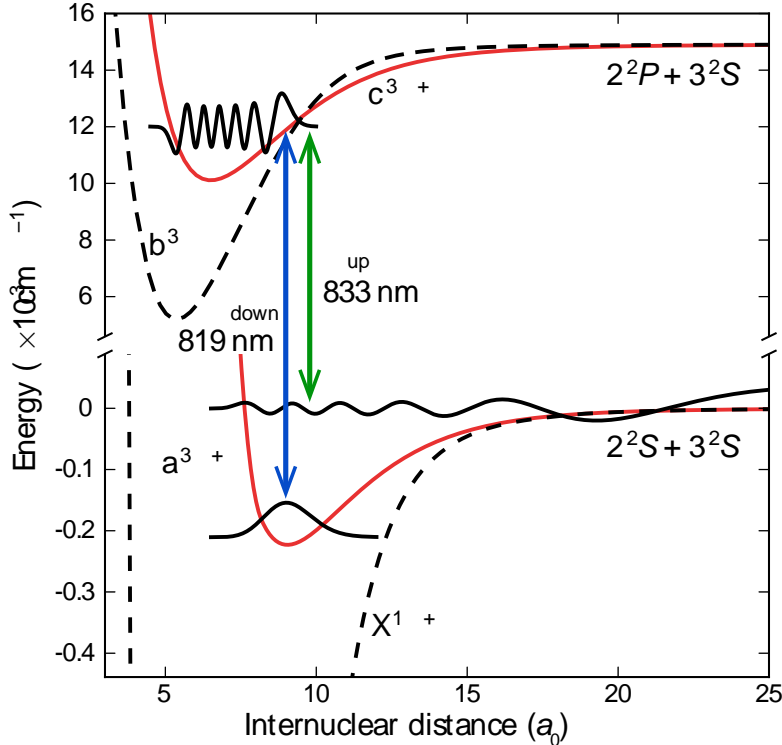


Figure 5-1: Molecular potentials and transitions for formation of NaLi triplet ground state molecules. The $a^3\Sigma^+$ ground potential and $c^3\Sigma^+$ excited potential are shown in red. The wavefunctions of Feshbach molecules, the electronically excited intermediate, and the triplet ground state are drawn, along with the laser transitions employed for STIRAP.

moment of $2\mu_B$ and an electric dipole moment of 0.2 D [23, 44]. Since the triplet NaLi is both reactive with itself and not in the absolute ground state, the lifetime of a molecular sample will be of particular interest: Sec. 5.5.1 and 5.5.2 will describe the details of trapping the molecules on the timescale of several seconds, and compare our results to a universal collision model. Lastly, Sec. 5.5.3 will demonstrate the novel feature of a magnetic dipole moment in an ultracold molecule by performing electron spin resonance spectroscopy (ESR).

5.1 Experimental approach

In contrast to the PA and two-photon spectroscopy, the experiments presented here were performed in a single beam optical dipole trap (ODT). This is necessary because

Feshbach resonances exist only between non-magnetically trappable states of atomic Na and Li, necessitating the use of optical confinement. The starting point of all experiments performed in this chapter are an ultracold Na and Li mixture in their lowest Zeeman sub-levels¹, confined in an ODT at a bias field of $B_z = 745.55$ G (see Fig. 2-2). The cloud has a cigar-shaped geometry similar to that of experiments performed in the magnetic trap (Fig. 5-2). The radial confinement is produced by

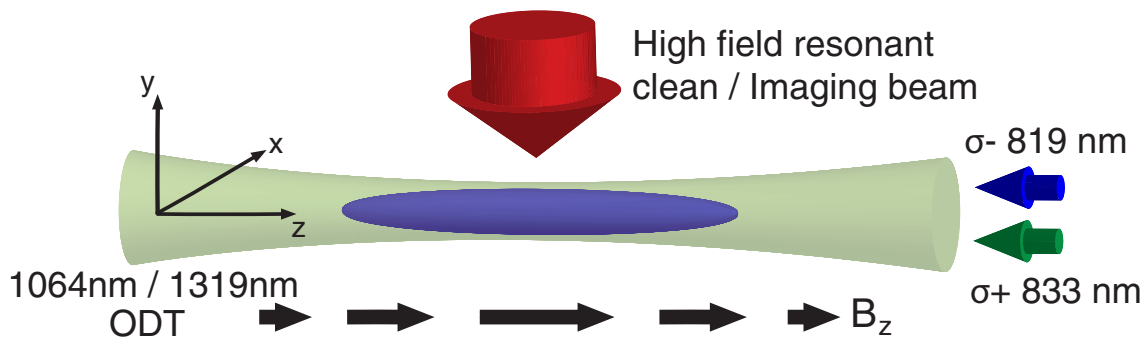


Figure 5-2: Optical dipole trap geometry at high magnetic fields. The dual species Na and Li mixture was held in a single beam ODT formed by a far off-resonant laser at 1064 nm or 1319 nm. The radial confinement was produced by the ODT, and axial confinement was produced by both the ODT and the magnetic field curvature of the Feshbach coils (producing a field maximum). The STIRAP beams were co-axial to the ODT beam. A transverse two-color beam resonant with free Na and Li atoms was used for both imaging the atoms and removing them from the trap when isolation of molecules was desired.

the ODT, with a trapping frequency of $\omega_{r, \text{Na}} = 500$ Hz for Na. The axial confinement is primarily from the Feshbach coils which produce a field maximum to confine the high-field seeking Na and Li $|1\rangle$ states, with a trapping frequency of $\omega_{z, \text{Na}} = 13$ Hz. Note that all of the molecules we discuss in this chapter are *low* field seeking, and are axially anti-trapped by the magnetic field. This will be particularly important when attempting to measure molecular lifetimes beyond timescales of $\omega_{z, \text{Na}}^{-1}$ (Sec. 5.5.1). Typical atom numbers were 1×10^6 of each Na and Li at temperatures of $2 \mu\text{K}$, with densities of $\sim 3 \times 10^{12} \text{ cm}^{-3}$ for both species. The corresponding peak densities were $n_{\text{Na}} = 4 \times 10^{12} \text{ cm}^{-3}$ and $n_{\text{Li}} = 3 \times 10^{12} \text{ cm}^{-3}$.

Another important distinction in this experiment compared to those discussed

¹I.e. the $|1\rangle$ states.

in prior chapters is how molecule formation is detected. The PA experiments in Chapter 3 showed molecule formation by observing atomic loss originating from the uncontrolled spontaneous emission following PA to an excited molecular state. Conversely, all molecule formation experiments in this chapter were performed with state-selective and reversible methods. In an ultracold mixture of atoms and molecules, the molecules were isolated by illuminating the sample with resonant light to “clean” away free atoms (while leaving the molecules unaffected²), and then counted by reversing the molecule formation procedure and imaging the dissociated atoms (see Fig. 5-3 a). Thus all measurements of molecule number in this chapter are from measurements of their constituent free atoms. Since the molecules of interest here are dimers, a sample of dissociated molecules should yield equal amounts of Na and Li. While we did observe this to be true, in many measurements the dissociated Li number alone was used to count molecule number. This was because the free-atom imaging was done at high magnetic fields, in which Li exhibits a much higher-quality cycling imaging transition compared to Na³, which results in better signal-to-noise in images of Li.

5.2 Feshbach molecules revisited

Feshbach resonances provide a means of coherently forming weakly bound molecules from free atoms [142]. Formation of NaLi Feshbach molecules was first achieved in our group in 2012 [54, 55]. In comparison to other bi-alkali species, NaLi has very narrow (\sim mG) resonances at high fields (> 700 G), and using these resonances for molecule formation is experimentally difficult. The narrow widths of these Feshbach resonances are due to a weak spin-orbit coupling between the scattering and molecular states, which flips the electronic spins on the colliding Na and Li pair ($\Delta S = 2$) while forming a rotating ($N_g = 2$) molecule [72]. For a number of years this coupling mechanism was

²As will be discussed in the next section, the Feshbach molecule state in particular was not entirely transparent to the atom clean-out light, and it was important not to over-illuminate the sample with clean-out light to avoid adverse effects.

³Imaging the $|1\rangle$ state of either Na or Li at low fields is never a cycling transition due to ground state hyperfine coupling. High magnetic fields reduce this effect, however since Li has a much lower hyperfine constant than Na, it exhibits a cycling transition even at ~ 700 G, while Na needs significantly higher fields.

poorly understood [143, 72], and consequently the formation of NaLi molecules was a difficult, multi-year effort [73]. In the following, I describe our brief re-visit of experiments in formation of Feshbach molecules as a stepping stone towards reaching the triplet ground state.

Our approach was to replicate the experiment of our prior report [54]. The experimental sequence is shown in Fig. 5-3 a. The Feshbach coils were used to produce a large bias field of 745.55 G, just above the Feshbach resonance. A small shim coil was used to lower the bias field and perform a Landau-Zener sweep to form Feshbach molecules. We found optimal Feshbach molecule formation efficiency with a 300 mG/ms sweep for 1 ms, which resulted in formation of 3×10^4 Feshbach molecules, corresponding to a formation efficiency of 3 %⁴.

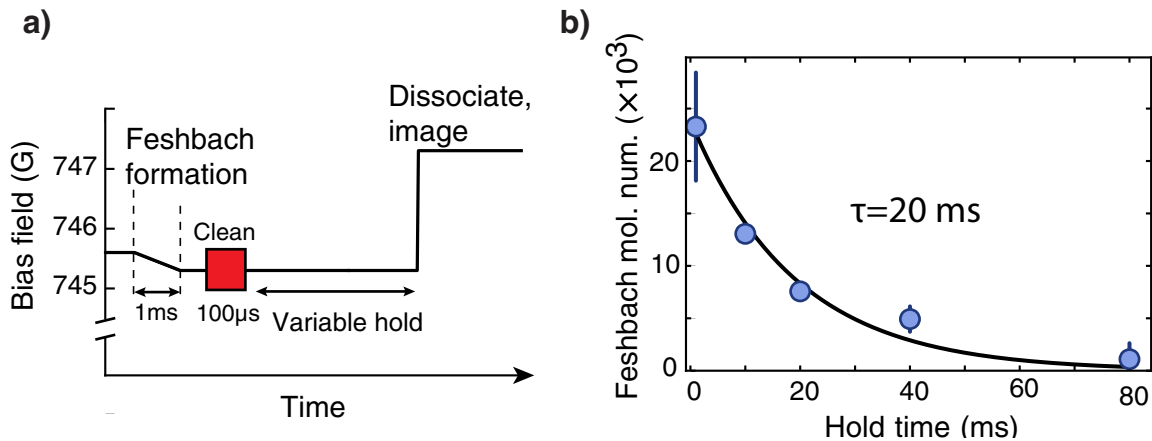


Figure 5-3: Feshbach molecule formation and lifetime. a) A schematic of the Feshbach molecule formation and detection sequence. A Landau-Zener formation sweep was followed by resonant clean-out of the free atoms to isolate the Feshbach molecules. Raising the field back above the Feshbach resonance results in dissociation of the molecules to free atoms, which could then be imaged. b) The Feshbach molecule lifetime measured with such a sequence, showing a 20 ms lifetime.

Our prior work with Feshbach molecules reported very fast loss timescales (< 1 ms) if the remaining free-atoms were not quickly removed from the sample. We used a 300 μ s resonant “clean-out” light pulse to remove the $|1\rangle$ state Na and Li atoms, with intensities of $I_{\text{Na}} = 80 \mu\text{W}/\text{cm}^2$, $I_{\text{Li}} = 15 \mu\text{W}/\text{cm}^2$. The clean-out pulse adversely

⁴Our prior work [54] found a slightly higher formation efficiency of 5 %. It is likely we could optimize the Feshbach molecule formation efficiency by varying the density, however our primary focus was to move on with STIRAP.

affects the Feshbach molecules, and it is crucial that the clean-out beam is perpendicular to the long axis of the cigar-shaped cloud (Fig. 5-2). In this geometry the beam illuminates a low optical density of atoms, allowing for the use of low laser beam intensities. Our initial attempts to form Feshbach molecules used an axial clean-out beam with considerably higher intensities ($\sim 1 \text{ W/cm}^2$) that were necessary to “punch through” the high axial optical density within a few hundred μs , but this beam also destroyed the Feshbach molecules themselves. The clean-out pulse is *not* perfect, and leaves approximately 5 % of the atoms in the trap in a Zeeman dark state—the effects of this will be further described in Sec. 5.5.1 during the measurement of the ground state molecule lifetime.

Feshbach molecule lifetimes were measured by holding the molecules for a variable duration before dissociating and imaging. If the molecules were kept in the presence of either species (i.e. the clean-out pulse was applied at the *end* of the variable hold in Fig. 5-3 a), a short $< 0.5 \text{ ms}$ lifetime was observed in agreement with our prior report [54]. However, we found the isolated Feshbach molecule lifetime to be 20 ms (Fig. 5-3 b), a factor of 20 longer than we had previously observed⁵. We suspect the reason for this discrepancy was the 1064 nm Nd:YAG laser used in the 2012 experiment to produce the ODT was unknowingly producing multi-mode, broad ($\sim 2 \text{ nm}$) spectrum light which resonantly excited a bound-to-bound transition in the Feshbach molecules⁶. This laser has since been repaired and its single-mode spectrum confirmed using the 60 MHz resolution wavemeter. Without optical excitation of the Feshbach molecules from the ODT, they now exhibited a lifetime that was limited by collisions with the remaining free-atoms left from the imperfect clean-out pulse. Observation of a 20 ms Feshbach molecule lifetime was a fortuitous surprise. Although we were prepared to work with 1 ms lifetimes⁷, the extended lifetime provided some breathing room in case the experiments did not go according to plan.

Having discussed the formation of Feshbach molecules, we now briefly discuss

⁵Of course, lifetime measurements depend on the number density in the sample, but in this case we were careful to replicate the same density as in our prior experiment.

⁶This was a difficult problem to diagnose, since the multi-mode laser worked very well for trapping the atomic species and only disturbed molecular states.

⁷STIRAP is a relatively fast procedure, requiring only a few hundred μs .

their properties pertaining to two-photon STIRAP. As previously mentioned, NaLi Feshbach molecules are unique among the bi-alkalis in that they are rotating with quantum numbers $v_g = 10$, $N_g = 2$, $m_N = -2$ [72]. This means the polarizations of the two photons used in STIRAP must be chosen to remove the two units of angular momentum from the molecule to place it in the rotational ground state (discussed in the following section). Another relevant consideration is the effect of molecular rotation on transition strengths. The two-photon spectroscopy of Chapter 4 studied only the $v_g = 10$, $N_g = 0$ state which has a binding energy of only 9.35 GHz. The Feshbach state $N_g = 2$ has a binding energy of 5.85 GHz, which is more than a mere perturbative shift of the $N_g = 0$ state, prompting the question of how might centrifugal distortion change the Franck-Condon factors. Fig. 5-4 shows the result of numerically solving for the least bound ($v_g = 10$) wavefunction using *ab initio* potentials with and without an $N_g = 2$ centrifugal barrier. The results show negligible differences between the Feshbach wavefunction and the $N_g = 0$ state, thus we did not expect any significant changes to the transition strengths measured with two-photon spectroscopy in Chapter 4.

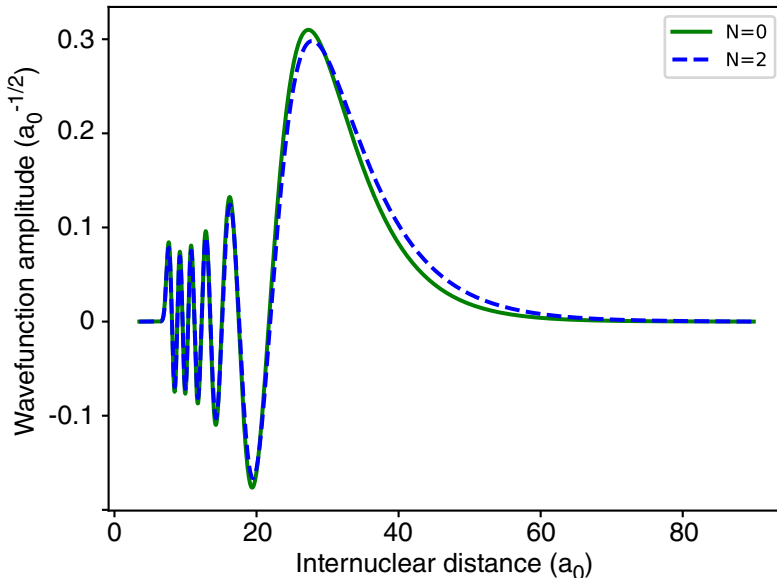


Figure 5-4: Centrifugal distortion of the Feshbach molecule wavefunction. The Feshbach molecule wavefunction as calculated from *ab initio* potentials for $N_g = 0, 2$ rotational states, showing only a minor effect from centrifugal distortion.

5.3 Molecular spectroscopy at high magnetic fields

The spectroscopy of Chapters 3 and 4 were performed with an initial collisional state of Na $|8\rangle$ and Li $|6\rangle$ atoms at a bias field of $B_z = 1.2$ G. In Sec. 4.2 we concluded that the $v^* = 11$ state of the $c^3\Sigma^+$ potential was the ideal intermediate state for STIRAP. In this section, we applied these findings to perform spectroscopy from an initial Feshbach molecule state at a bias field of $B_z \approx 745$ G. Note that we will ignore the effect of nuclear spins (hyperfine coupling), until a brief discussion at the end of this section.

First, we consider the effect of the magnetic field on the intermediate state $v^* = 11$ which was discussed in detail in Sec. 3.3.1. The Hamiltonian for the excited state structure is given by eq. 3.3 with an additional electronic spin Zeeman term, which we re-write here for clarity

$$\begin{aligned} H_{\text{exc}} &= H_{\text{d-d}} + H_{\text{spin-rot}} + H_{\text{Zeeman}} \\ &= (182.1 \text{ MHz}) \left(3(\vec{S}_1 \cdot \hat{r})(\vec{S}_2 \cdot \hat{r}) - \vec{S}_1 \cdot \vec{S}_2 \right) + (16.2 \text{ MHz}) \vec{S} \cdot \vec{N} - \mu_B S_z B_z \end{aligned} \quad (5.1)$$

where we've inserted the measured coupling strengths (see Sec. 3.3.1), and have ignored any rotational magnetic coupling terms of the form $\vec{N} \cdot \vec{B}$ as this coupling is typically weak. Fig. 5-5 shows the results of numerically diagonalizing eq. 5.1: At magnetic fields above 200 G, the excited state structure splits into three diverging manifolds, corresponding to the three projections of the triplet electronic molecular states onto the magnetic field axis. This separation of energy scales between the increasing electronic Zeeman interaction and constant terms $H_{\text{d-d}}$ and $H_{\text{spin-rot}}$ is analogous to the Breit-Rabi formula for hyperfine effects in alkali atoms (see for example Fig. 2-2). The high-field rotational quantum numbers are deduced by conservation of angular momentum along the magnetic field axis ($m_{\text{total}} = m_S + m_N$ is conserved). Unlike the Breit-Rabi solution, the high-field ordering of the m_N states in Fig. 5-5 is much less intuitive due to the electrons' dipole-dipole coupling, $H_{\text{d-d}}$.

Having understood the Zeeman splittings in the excited molecular state, we now turn our attention to laser spectroscopy of the Feshbach molecules. Fig. 5-6 shows the

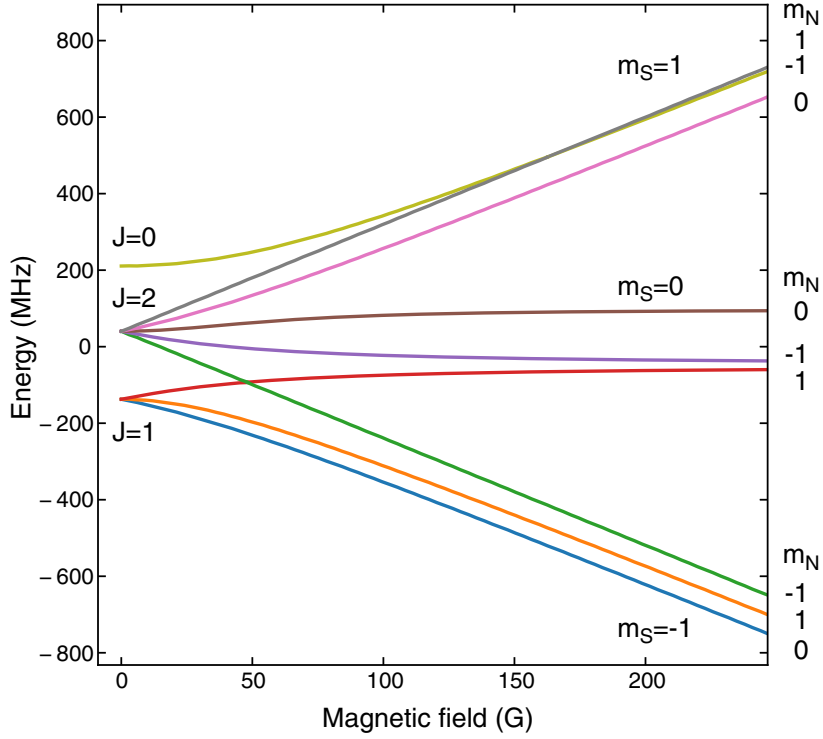


Figure 5-5: Zeeman splitting of the $c^3\Sigma^+$, $v^* = 11$ excited molecular state. The excited states split into three manifolds due to the total electronic spin alignment relative to the external magnetic field, and are further split by the weaker dipole-dipole and spin-rotation coupling in the molecule. The angular momentum projection quantum numbers are deduced from angular momentum conservation.

relevant states in a transition from the Feshbach molecules to the excited $v^* = 11$ state at various magnetic fields. The Feshbach molecule splittings were carefully studied by the Tiemann group [72], and here we use their results without explicitly solving their coupling Hamiltonian. Molecular electric dipole transition selection rules between Σ states in Hund's case (b) require the molecular rotation to change by $\Delta N = \pm 1$, $\Delta m_N = \pm 1, 0$. Thus the initial Feshbach state at 745 G with quantum numbers $v_g = 10$, $m_S = 1$, $N_g = 2$, $m_N = -2$ can only couple to the excited $v^* = 11$, $m_S = 1$, $N^* = 1$, $m_N = -1$ state with σ^+ polarized light. The laser frequency of this transition can approximately deduced from the PA transition to the $v^* = 11$, $J = 2$ low-field excited state at 359.99798 MHz measured in Chapter 3 and adding the additional Feshbach molecule binding energy of 5.85 GHz, yielding an expected upleg transition

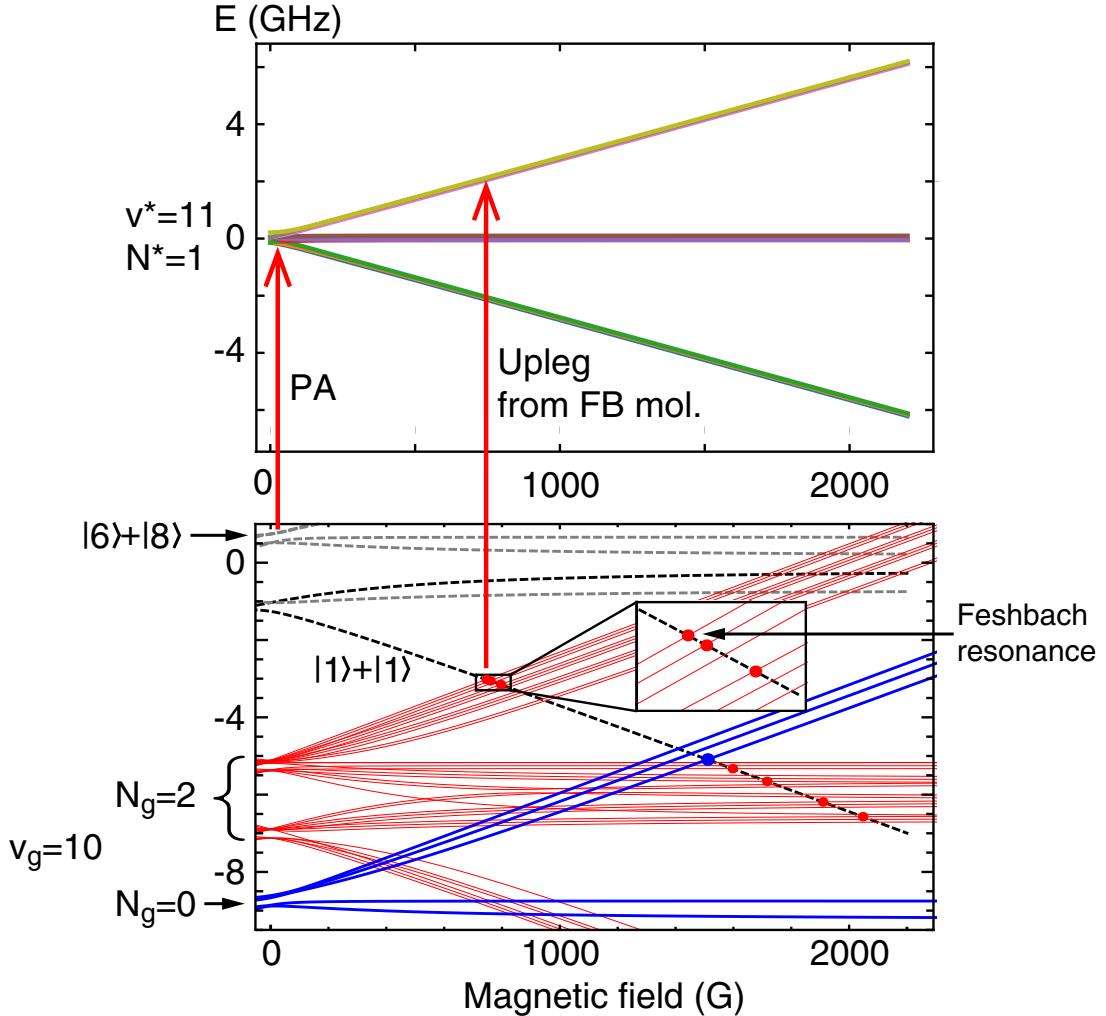


Figure 5-6: Transition diagram between the Feshbach state ($a^3\Sigma^+$, $v_g = 10$) and intermediate excited state ($c^3\Sigma^+$, $v_g = 11$) at high magnetic fields. (Top) The excited state Zeeman splitting of Fig. 5-5 is shown at high magnetic fields. (Bottom) The free atom Zeeman shifts (dashed lines) and the $a^3\Sigma^+$, $v_g = 10$ molecular Zeeman shifts (red lines for hyperfine states of $N_g = 2$, blue lines for $N_g = 0$) are shown (adapted from Fig. 3 of [72]). The free-to-bound PA transitions studied in Chapter 3 and the bound-to-bound transition starting with Feshbach molecules are shown with red arrows. The large number of lines in the bottom diagram are from hyperfine states which were considered in the analysis of [72]. Such hyperfine effects in the excited state (top diagram) would be too small to see on the scale of these figures.

frequency of 360.0038 THz⁸. Since both the Feshbach and excited state molecules are

⁸In this simple explanation I've ignored the ~ 200 MHz splitting between the $v^* = 11$, $J = 0, 2$ states in Fig. 5-5, however this is inconsequential since the high field states $m_S = 1$, $m_N = \pm 1$ end up nearly degenerate. In any case, a careful examination of Fig. 5-5 and Fig. 5-6 will give the expected

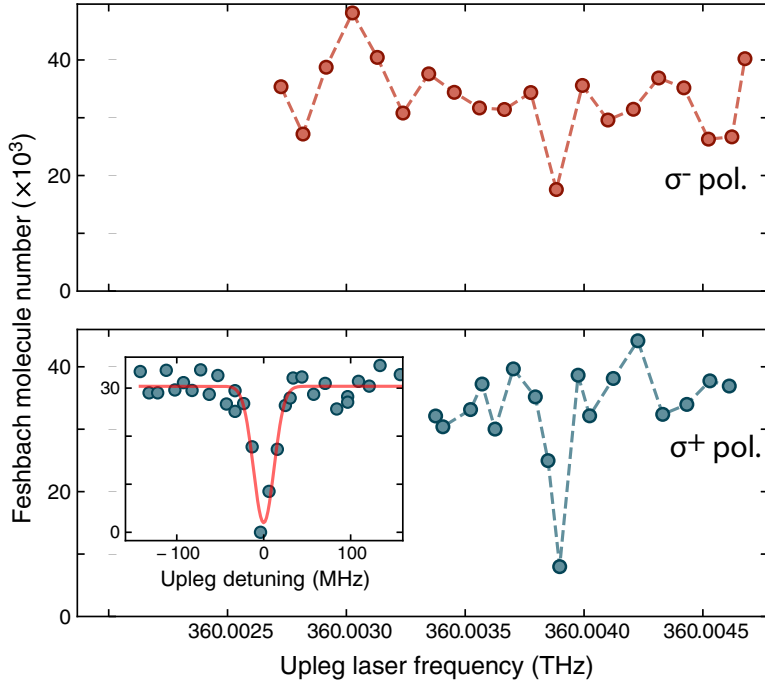


Figure 5-7: Upleg transition spectroscopy at 745 G. (Top) Feshbach molecule spectrum after a 50 mW, 200 μ s exposure to the upleg laser with σ^- polarization, showing no significant loss features. (Bottom) Feshbach molecule spectrum after a 2 mW, 200 μ s exposure to the upleg laser with σ^+ polarization, showing a clear loss feature. The inset shows a finer scan (4 μ W, 300 μ s exposure), revealing only a single loss feature. Note that the σ^- spectrum shows a slight resonant dip, however this is simply due to polarization imperfections in the excitation beam and the use of higher power upleg laser light.

in the $m_S = 1$ electronic state, the large Zeeman shifts are common mode.

Fig. 5-7 shows the results of upleg spectroscopy performed with Feshbach molecules at 745 G. As with PA spectroscopy, loss of Feshbach molecules due to uncontrolled spontaneous decay from the excited state signals the finding of a bound-to-bound resonance. As expected, we found only one spectroscopic line in the upleg spectroscopy at 360.00381(1) THz, which responds only to σ^+ polarization. In contrast to the PA spectroscopy, the upleg transition strength was significantly stronger due to the bound-to-bound transition. Typical upleg laser powers were μ W with exposure times of only a few hundred μ s, which are a factor of 10^9 smaller pulse areas than used in the PA spectroscopy.

upleg at a frequency of 360.0038 THz.

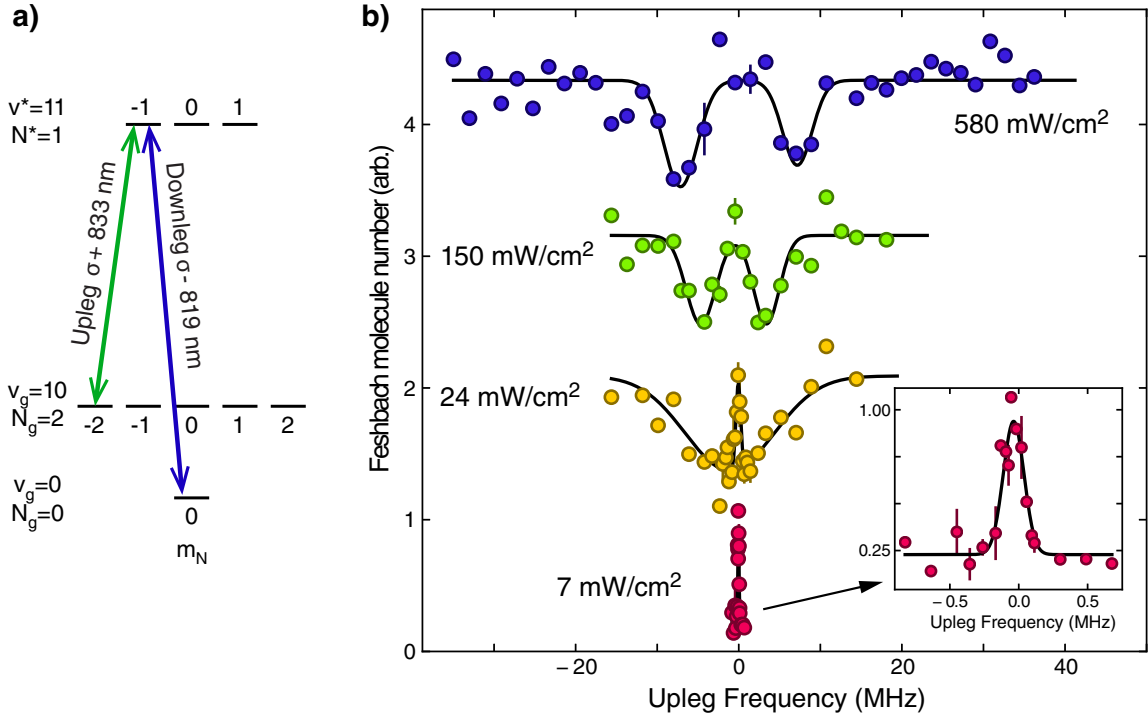


Figure 5-8: Two-photon spectroscopy using Feshbach molecules. a) An energy level diagram showing the molecular rotation angular momentum states. b) An Autler-Townes spectrum of the ro-vibrational ground state, taken at various downleg powers with a $100 \mu\text{s}$ exposure time and 17 mW/cm^2 upleg power. At low downleg intensities a narrow EIT feature is observed (red data points) with a width of 75kHz.

Using this intermediate transition we performed two-photon spectroscopy to find the downleg transition frequency to the ro-vibrational triplet ground state, $v_g = 0$, $N_g = 0$. The laser frequency of the downleg transition at high magnetic fields was expected to be very similar to the result of low-field two-photon spectroscopy (Chapter 4), once again due to the common-mode Zeeman shifts in the $m_S = 1$ electronic state. We found the downleg transition to the ro-vibrational ground state at a laser frequency of $366.23611(1)$ THz⁹. Fig. 5-8 shows the Autler-Townes spectrum of this three-level system and the transition to a sharp EIT feature. This two-photon spectroscopy required σ^- polarized downleg light, which is consistent with a $m_N = -1 \rightarrow 0$

⁹This is 30 MHz lower than the measured frequency in Sec. 4.3, which is explained by the slight fine-structure difference between the excited $m_S = 1, m_N = -1$ state and the $m_S = 1, m_N = 1$ state at 745 G (as shown in Fig. 5-5, although the x-axis does not extend to 745 G). Recall that the $m_S = 1, m_N = 1$ is exactly the stretched $J = 2, m_J = 2$ state used for the two-photon spectroscopy at low field in Chapter 4.

transition from the excited state down to the ro-vibrational ground state (Fig. 5-8 a).

Lastly, we mention the effect of hyperfine coupling. In all of the aforementioned molecular transitions (including magneto-association around the Feshbach resonance), the nuclear spin states of the Na and Li nucleii are $m_{I,\text{Na}} = 3/2$, $m_{I,\text{Li}} = 1$, respectively. As described in the previous section, NaLi Feshbach molecule formation uses a magnetic coupling between the electron spins and the orbital angular momentum which does not affect the nuclear spins. In the case of the one- and two-photon molecular spectroscopy discussed here, small excited state hyperfine splittings on the order of $\sim \text{MHz}$ surely exist¹⁰. While these splittings are small, they would be easily resolvable at low magnetic fields since an EIT spectrum provides $< 100 \text{ kHz}$ resolution (Fig. 5-8 b). However, the use of a high magnetic field environment decouples the hyperfine interaction, and thus the nuclear spins are unaffected during photonic transitions. This is a subtle point, as the non-observation of hyperfine splittings in the two-photon spectroscopy experiments in Chapter 4 was obviously *not* due to high-magnetic fields, but rather the use of stretched angular momentum states. Thus, for one reason or another, we have been able to conveniently ignore nuclear spin states and hyperfine couplings. As we move the discussion forward towards the triplet ground state NaLi molecule, it should be noted that hyperfine effects in electronic ground states are significantly larger than in electronic excited states, and these effects will become the focal point of Sec. 5.5.3.

5.4 STIRAP transfer to the ro-vibrational ground state

The procedure of stimulated Raman adiabatic passage (STIRAP) was pioneered for systems of ultracold molecules in KRb [35] and Cs₂ [34], and has since been applied to a number of heteronuclear bi-alkali combinations [45, 46, 48, 47]. STIRAP itself is a widely applicable technique of coherently transferring between quantum states

¹⁰This energy scale is estimated from the hyperfine splittings of free an excited free atomic Li, which is the dissociation limit of excited NaLi $c^3\Sigma^+$ potential.

while avoiding spontaneous emission [75]. One may ask why a two-photon transfer is even necessary—why not simply couple the Feshbach and ground states directly with a single photon? There are two issues with this approach. The primary limitation is that despite the non-zero electric dipole moment of the NaLi molecule, the dipole transition is small due to the poor wavefunction overlap between the Feshbach and ground states, though in this case the Franck-Condon-type matrix element contains a dipole moment operator, i.e. $\langle \psi_{\text{Fesh}} | \vec{d}_{\text{nuc}} | \psi_{\text{gnd}} \rangle \propto \langle \psi_{\text{Fesh}} | \vec{R} | \psi_{\text{gnd}} \rangle$, where the nuclear dipole moment operator, \vec{d}_{nuc} , is proportional to the internuclear separation, \vec{R} (see eq. 2.12 of [55]). The second limitation is technological: strong coherent radiation sources at the 6 THz resonant transition frequency do not exist¹¹. Therefore to transfer molecules between different vibrational states in the same electronic potential we must employ an intermediate excited state and the frequency difference of two infrared lasers in a two-photon transition.

In our case, STIRAP allows for coherent transfer of Feshbach molecules to the triplet ground state via the $v^*=11$ excited state, which has a short spontaneous decay lifetime of ~ 30 ns. The excited state is never populated and the system stays in the dark eigenstate (assuming zero two-photon detuning)

$$|\psi_{\text{dark}}\rangle = \cos \theta |\psi_{\text{Fesh}}\rangle + \sin \theta |\psi_{\text{gnd}}\rangle \quad (5.2)$$

where the mixing angle is given by the ratio of upleg and downleg couplings, $\tan \theta = \Omega_{\text{up}} / \Omega_{\text{down}}$ (for a derivation, see Sec. III D of [140]). By changing the relative upleg and downleg couplings, we can move the population from purely in the Feshbach state ($\Omega_{\text{up}}=0$) to purely in the ro-vibrational ground state ($\Omega_{\text{down}}=0$). By considering these limiting cases we find that STIRAP requires a somewhat peculiar pulse sequence, where transfer to the ground state is achieved by first turning on the downleg followed by increasing the upleg intensity as in Fig. 5-9 b (this is the opposite pulse order as one would intuitively expect when sequentially transferring $|\psi_{\text{Fesh}}\rangle \rightarrow |\psi_{\text{exc}}\rangle \rightarrow |\psi_{\text{gnd}}\rangle$, hence it's been colloquially called the “counter-intuitive”

¹¹THz sources are an active field of research. For recent developments in the 1-6 THz band, see [144].

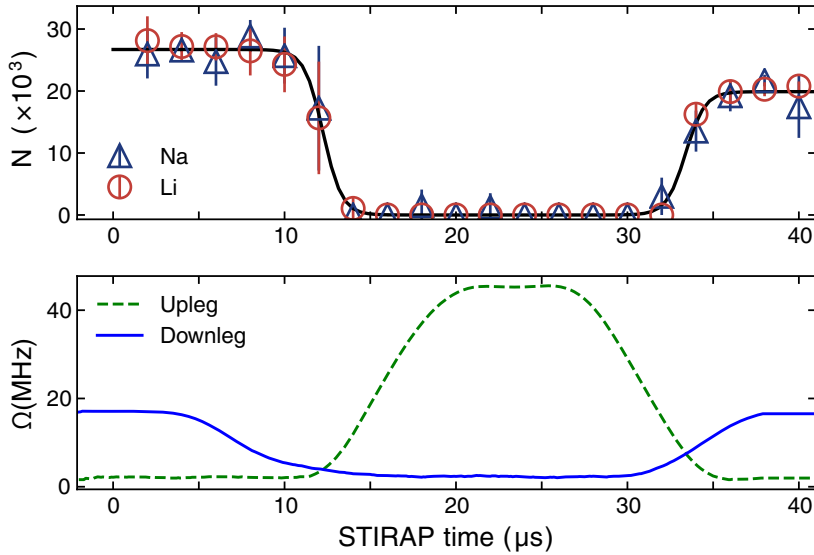


Figure 5-9: STIRAP from Feshbach molecules to the ro-vibrational ground state. The Feshbach molecule number is shown at various points during a forward and reverse STIRAP pulse sequence. The disappearance and re-appearance of the Feshbach molecules indicates a reversible transfer to the ro-vibrational ground state.

pulse sequence). Changes to the upleg and downleg coupling must be done slowly ($\tau_{\text{pulse}} \gg \Omega_{\text{up}}^{-1}, \Omega_{\text{down}}^{-1}$) to keep the transfer adiabatic and not excite any population in the short-lived excited state.

We applied the counter-intuitive (STIRAP) pulse sequence to our sample of Feshbach molecules with the upleg and downleg lasers on two-photon resonance to within 10 kHz (as determined by the EIT spectrum). Since the STIRAP process is coherent and reversible, a successful STIRAP transfer to the ground state was confirmed by the disappearance of Feshbach molecules and a later re-appearance if the pulse sequence was reversed (we call this “forward” and “reverse” STIRAP transfer). This effect is shown in Fig. 5-9.

We found optimal transfer using a 40 μs round-trip forward and reverse STIRAP pulse for which 74 % of the initial Feshbach molecules were recovered, corresponding to an 86 % one-way transfer efficiency. The pulse sequence was only crudely optimized by varying pulse durations and initial laser intensities. The pulse-shapes were intended to be linear ramps in laser intensity, however technical control limitations of laser

intensity on short (μs) timescales resulted in the pulses of Fig. 5-9.

The upleg and downleg Rabi frequencies were calibrated by upleg loss measurements and Autler-Townes spectra, respectively (as in Chapters 3 and 4). The entirety of the STIRAP transfer happened in a $\sim 5 \mu\text{s}$ time window at a Rabi frequency crossing $\Omega_{\text{down}} \approx \Omega_{\text{up}} \approx 5 \text{ MHz}$, which satisfied the adiabatic criteria with $5 \mu\text{s} \gg \Omega^{-1} \approx 0.03 \mu\text{s}$. Increasing the STIRAP pulse duration only worsens the transfer efficiency (Fig. 5-10), further indicating that the transfer efficiency is not limited by adiabaticity.

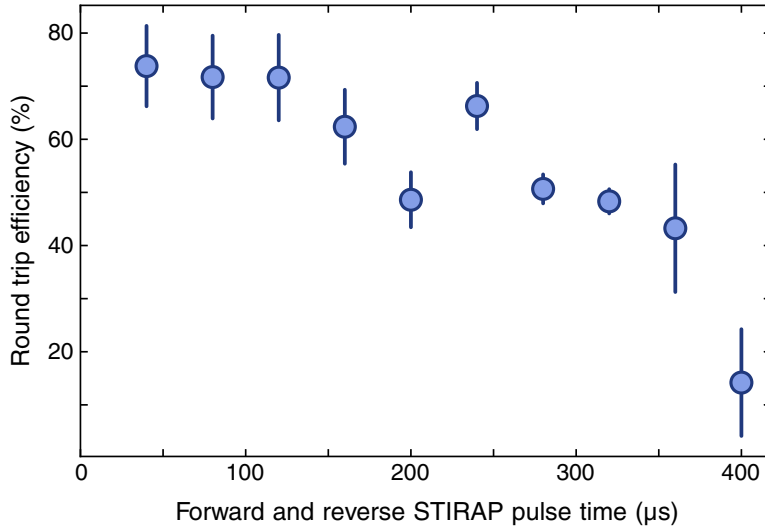


Figure 5-10: STIRAP efficiency as a function of pulse duration. The STIRAP efficiency only decreased with longer pulse durations, possibly revealing a timescale for uncontrolled decoherence.

The cause of decreased STIRAP efficiency for longer pulses is likely some form of uncontrolled decoherence. The relevant time-scale for this decoherence is the transfer duration (i.e. when $\Omega_{\text{up}} \approx \Omega_{\text{down}}$), which we can see from Fig. 5-9 is approximately 1/8th of the total forward-reverse pulse time. Thus it seems there are issues maintaining coherence at times in excess of $50 \mu\text{s}$ corresponding to a 3 kHz broadening. We have not made a careful study of this decoherence, and here I present a brief discussion of possible effects that may limit the transfer duration:

- The laser linewidths are an obvious suspect, and using a number of different estimation methods (see Chapter 2, or [80]) we expect the relative laser linewidth

to be < 1 kHz. This timescale limit is only a factor of 3 away from the observed decoherence, thus the laser linewidths are the primary suspect in limiting the STIRAP coherence time.

- A slim possibility is magnetic field noise: the triplet state transitions considered here have mostly common mode Zeeman shifts, with the exception of a ~ 10 kHz/G transition shift from fine structure effects. But even a conservative estimate of field stability of 30 mG RMS (see Chapter 2) would only result in 300 Hz of broadening.
- The lifetimes of either the Feshbach state or ro-vibrational ground state could in principle impose a transfer time limit. However, as measured in Sec. 5.2 the Feshbach molecule lifetime was in excess of 20 ms, and as will be discussed in the following section the ro-vibrational ground state lifetime was similarly long in the 1064 nm ODT.
- The ultracold sample temperature, $T \approx 2$ μK , corresponds to a 40 kHz Zeeman broadening and a 25 kHz Doppler broadening for NaLi molecules. However, both of these effects should be common mode: As in the case of magnetic field noise, all Zeeman broadening is common to the molecular states with an $m_S = 1$ projection of the triplet state. The Doppler shifts are common to both upleg and downleg laser beams (since they are co-propagating), thus they do not significantly affect the two-photon detuning during STIRAP and should also be negligible.

This decoherence effect notwithstanding, the 86 % efficiency obtained with a 20 μs pulse was easily sufficient to study the ground state molecules with reasonable signal-to-noise (SNR). Fig. 5-11 shows a typical image of “NaLi ground state molecules”, which were detected by imaging free atoms after Feshbach association, forward and reverse STIRAP, and Feshbach dissociation. Two possible imaging geometries were used: bottom and side imaging. The bottom images showed faint traces of atoms, however numerical integration of the image along the axial trap direction revealed

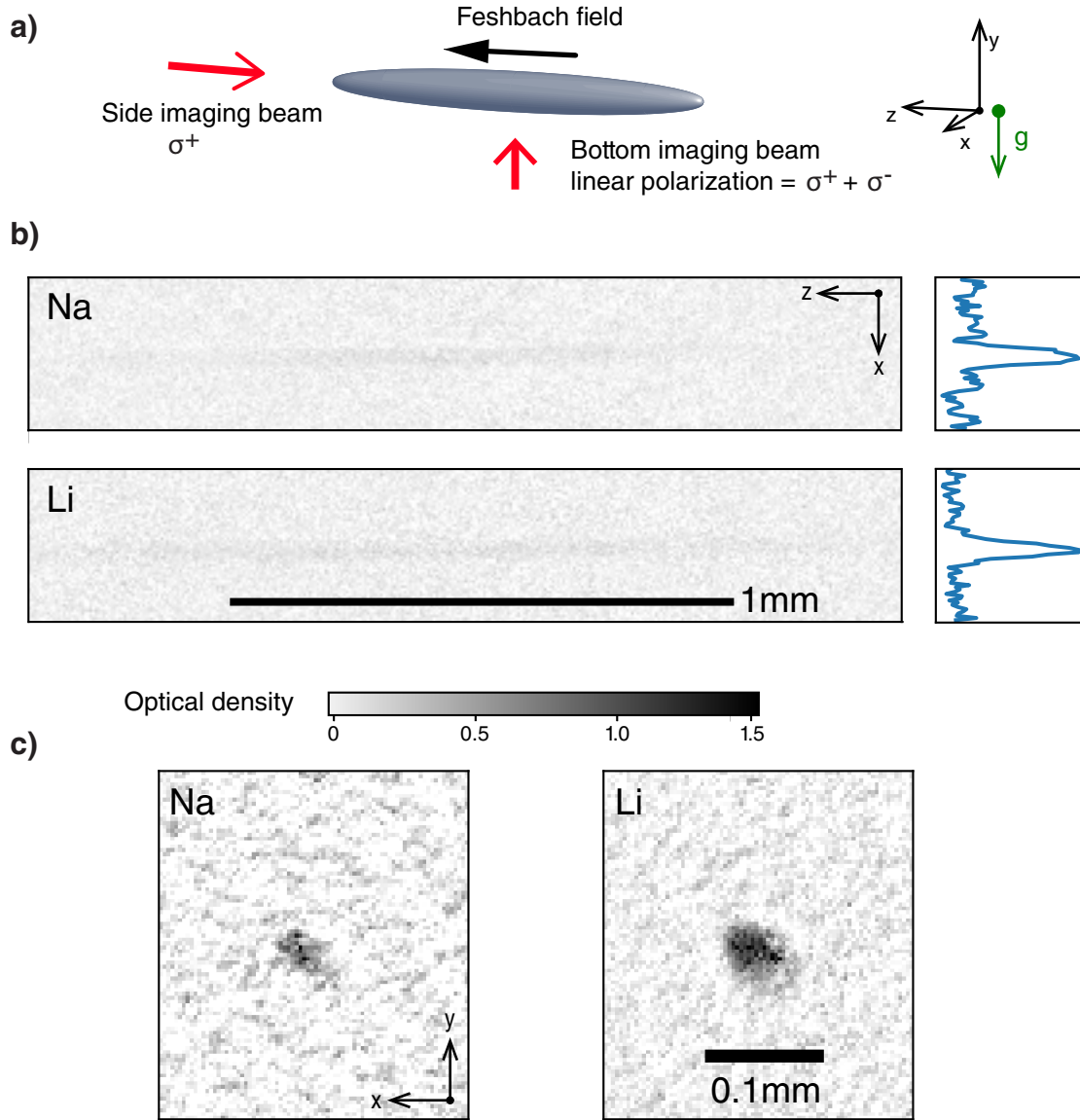


Figure 5-11: Imaging molecules after free atom dissociation. a) Two possible imaging geometries were used; bottom and side imaging. b) Bottom images, showing a faint signal in both Na and Li atom number, which can be numerically integrated and fitted to Gaussian profiles to accurately count molecule number. c) Side images, which clearly show the molecular signal in both Na and Li. All images were taken at 745 G. Note that these particular images are after a round-trip STIRAP to the triplet ground state, however images of Feshbach molecules (without ground state transfer) were of similar appearance.

clear Gaussian peaks. Side imaging allowed the imaging light to naturally observe a higher optical density and produce clearer images. Although both Li and Na images contained the same atom number, Li images typically produced a clearer signal due

to its better quality cycling transition at 745 G. Single-axis integrated bottom images and side images both yielded similar SNR, typically ~ 20 .

5.5 Studies of ultracold NaLi triplet ground state molecules

5.5.1 Lifetime and trapping

Measurement of the lifetime of triplet ground state NaLi molecules was the first definitive test of whether these molecules would be of any practical use. Long lifetimes make for an experimentally usable system and ultimately determine what kind of physics can be studied with the NaLi molecule.

NaLi is a fermionic molecule with exothermic two-body reactions, thus from the outset we expected the lifetime to be limited by the universal inelastic collision rate [43], which is approximately¹² $K_{\text{univ}} \approx 10^{-11} \text{ cm}^3/\text{s}$. With an initial atomic density of 10^{12} cm^{-3} and a $\sim 1\%$ ground state molecule formation efficiency, we expected molecule densities of $n_{\text{mol}} \approx 10^{10} \text{ cm}^{-3}$ and lifetimes of $(n_{\text{mol}} K_{\text{univ}})^{-1} \approx 10 \text{ s}$. The rest of this section will describe the experimental adventure to verify this simple calculation.

The molecular lifetime measurement was performed by simply adding a variable hold time between the forward and reverse STIRAP pulses. This experimental sequence and corresponding lifetime measurement are shown in Fig. 5-12. The measured lifetime, 28 ms, was considerably shorter than the expected 10 s, but there were a number of issues with the experimental sequence. First, the clean-out pulse was imperfect, and would optically pump the Na and Li to other hyperfine Zeeman states. This optical pumping effect was particularly bad for Na since at 745 G its imaging/cleaning transition is not cycling. This left approximately 5×10^4 Na atoms in the upper $F = 2$ Zeeman manifold (see Fig. 2-2), which were discovered by direct

¹²A detailed discussion of universal collisions will be given towards the end of this section. For now, we follow only rough calculations to give insight into the experimental procedure.

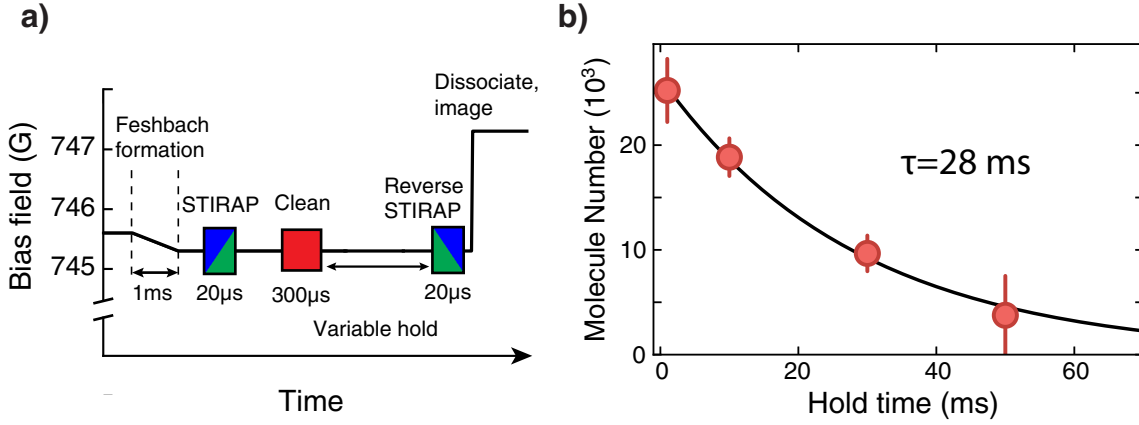


Figure 5-12: Initial measurements of the NaLi ground state lifetime. a) The experimental sequence to form triplet ground state molecules and measure their lifetime. Note that we waited until forming ground state molecules before removing free atoms with clean-out light. The ground state molecules were not at all affected by clean-out light, thus allowing for a longer duration clean-out pulse. b) The measured triplet ground state lifetime with such an experimental procedure, showing an unusually short lifetime of 28 ms.

absorption imaging at low magnetic fields after a clean-out pulse. These leftover Na atoms would remain in the optical trap and result in bad collisions with the NaLi molecules.

The clean-out issue was fixed by suddenly turning off the magnetic field and adding a secondary 15 ms clean-out pulse using the Li and Na laser cooling (MOT) light. The advantage of this approach was that it was thorough; we could be confident that no free atoms would be able to hide in dark states from the high-intensity MOT light at low magnetic fields. The disadvantage was that the sudden field drop of $\sim 800 \text{ G}$ gave a kick to the magnetically sensitive molecules, and furthermore the Feshbach field would have to be later turned back on to perform reverse STIRAP for detection¹³. Despite this disadvantage, lowering the field would have been necessary to keep the NaLi molecules trapped, as they were in low field seeking states and the Feshbach bias

¹³Another technical disadvantage to switching an inductive coil with 200 A of current off and on rapidly was that this caused some pretty serious voltage spikes which seemed to affect a lot of other electronics in the lab due to grounding issues. The computer monitors would slightly flicker during the field shutoff. These spikes also thoroughly tested the high-voltage capability of the magnetic field stabilization circuit described in Chapter 2.

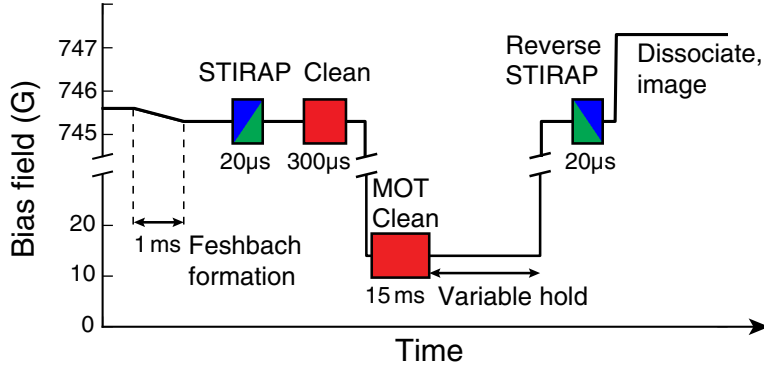


Figure 5-13: NaLi triplet ground state molecule formation sequence with thorough free atom clean-out. After STIRAP to the ground state and a clean-out pulse at 745 G, the magnetic field was immediately dropped to 13 G and the sample was further cleaned of free atoms with MOT light. The lifetime of the molecules was measured at low field using a variable hold time. Detection of molecules required the reversal of STIRAP and Feshbach dissociation.

field produces an axial field maximum¹⁴. This full clean-out and field-drop sequence is shown in Fig. 5-13.

Even with this improved lifetime measurement sequence, the NaLi molecule lifetime was extended to only 100 ms, which brings us to the second lifetime limitation: the 1064 nm ODT laser. Although 1064 nm is not enough excitation energy to reach the $c^3\Sigma^+$ potential studied in Chapter 3, *ab initio* calculations indicate that the 1064 nm ODT could drive excitations to the significantly deeper $b^3\Pi$ potential. Fig. 5-14 shows the calculated Franck-Condon factors for transitions to the $b^3\Pi$ potential for both the NaLi ro-vibrational ground state and Feshbach state. *Ab initio* calculations reveal that 1064 nm is 1 THz detuned from driving the NaLi triplet ground state ($v_g=0$) to the $v^*=16$ state of the $b^3\Pi$ potential. A rough calculation using the ODT parameters of 0.3 W and a 30 μm waist gives a scattering rate of 5 Hz¹⁵, consistent with the measured lifetime. Fig. 5-14 also shows that the Franck-Condon factor drops off rapidly towards longer wavelength, and with this in mind we decided to switch

¹⁴An alternative would be to use a crossed-optical dipole trap for axial confinement, an idea we toyed with but ultimately abandoned because of lack of ODT laser power.

¹⁵In the limit of large detuning, the scattering rate is $R = (\text{FCF}) \frac{\Gamma}{2} \frac{I/I_{\text{sat}}}{4(\Delta/\Gamma)^2}$, where $\Gamma = 2\pi \times 6 \text{ MHz}$, the detuning is $\Delta = 1 \text{ THz}$, $I = 0.3 \text{ W}/(30 \mu\text{m})^2$, $I_{\text{sat}} = 6 \text{ mW}/\text{cm}^2$, and the Franck-Condon Factor near the 1064 nm transition can be read off of Fig. 5-14 to be $(\text{FCF}) = 5 \times 10^{-3}$.

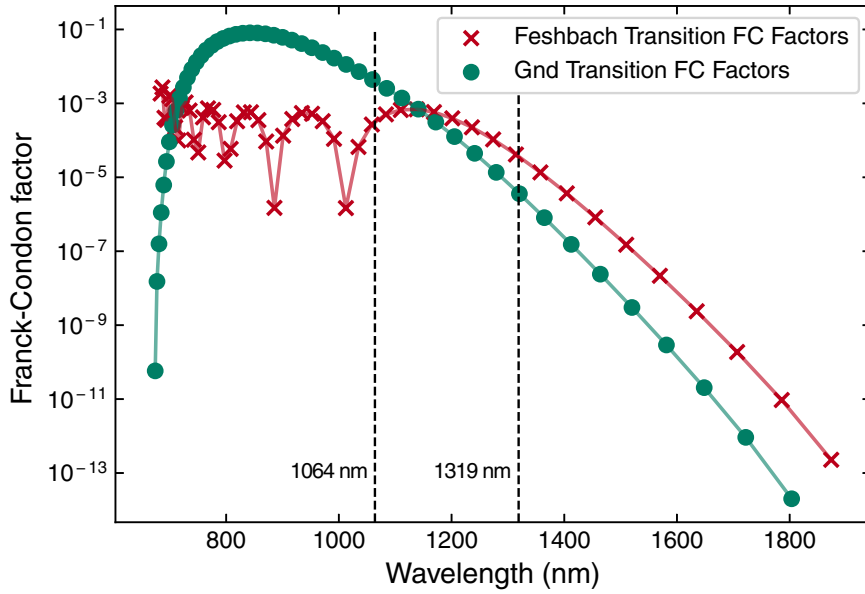


Figure 5-14: Franck-Condon factors for optical excitations to the $b^3\Pi$ potential of the NaLi molecule. *Ab initio* potentials were used to calculate Franck-Condon factors as a function of laser excitation frequency for an initial NaLi molecule in the triplet ground state (green circles) and the Feshbach molecular state (red crosses). The plot indicates that both ground state molecule and Feshbach molecules are susceptible to heating from a 1064 nm ODT. For the ground state molecules, a 10^3 reduction in Franck-Condon factor is possible by using a 1319 nm ODT.

the ODT to a 1319 nm laser¹⁶ which would reduce the bound-to-bound transition rate by a factor of 1000. The experimental sequence still used the 1064 nm ODT for ultracold atomic mixture preparation, but the mixture was transferred to a 250 mW, $32 \mu\text{m}$ waist, 1319 nm ODT before the molecule formation sequence of Fig. 5-13. The resulting NaLi triplet state lifetime in the 1319 nm ODT is plotted in Fig. 5-15. The molecule number exhibited a sharp loss in the first 300 ms due to magnetic kicks from the sudden field shut-off and turn-on in the experimental sequence. These kicks excited a center-of-mass axial sloshing of the molecules in the ODT resulting in a periodic loss pattern with a frequency of 7 Hz, consistent with the axial trapping frequency of the 1319 nm ODT. After this initial loss, the molecule number stabilized and exhibited a long lifetime on the order of seconds. We assumed a two-body

¹⁶There is nothing particularly special about the wavelength 1319 nm. We are lucky to work within the Center of Ultracold Atoms, where an unused 1319 nm laser can be found lying around.

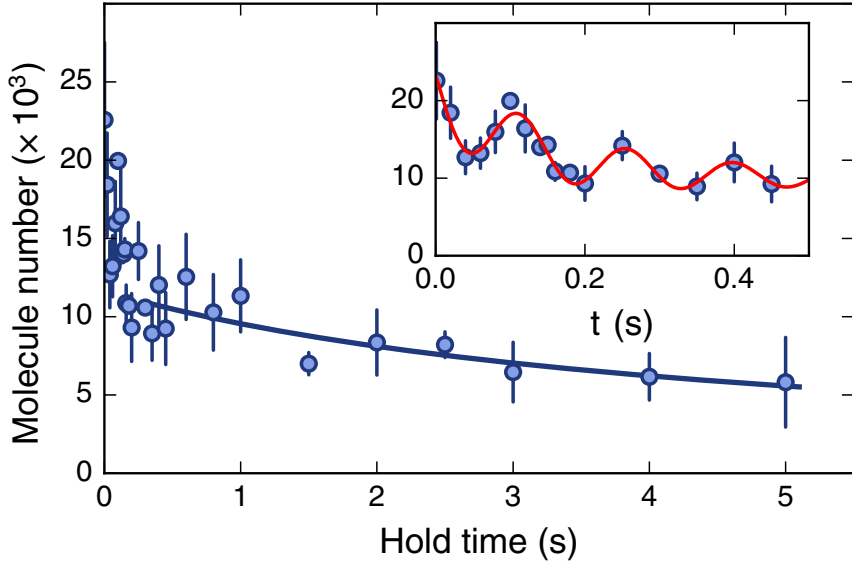


Figure 5-15: Long lifetime in a pure sample of isolated NaLi triplet ground state molecules. After an initial loss of molecules due to the sudden magnetic field drop, the NaLi molecules exhibit a slow decay with a fitted two-body loss timescale of 4.6 s. Inset: At short times (< 0.3 s), the molecule number drops while showing a 7 Hz oscillation, consistent with axial sloshing of the molecules in the single beam ODT.

loss mechanism and used the same fitting function as in PA experiments, eq. 3.4, to extract a loss timescale¹⁷ of $\tau = 4.6$ s.

This long timescale was an exciting result, because it immediately allowed us to probe the molecules for long durations to understand their properties. Not having a short lifetime constraint makes these experiments easy. In the following sections, we will describe the first experiments we performed to discover properties of our new triplet ground state NaLi molecules.

5.5.2 Estimating the loss coefficient

In order to compare our lifetime measurement to theoretical predictions, we must normalize the result by the molecule density. In order to find the molecule density, we must determine the trapping parameters and temperature of the sample. The trap frequency was determined by parametrically modulating the 1319 nm ODT and

¹⁷Use eq. 3.4, with $n_{\text{Na}} = n_{\text{Li}} \equiv n_{\text{mol}}$ and $\tau \equiv (n_{\text{mol}} \bar{K} I)^{-1}$.

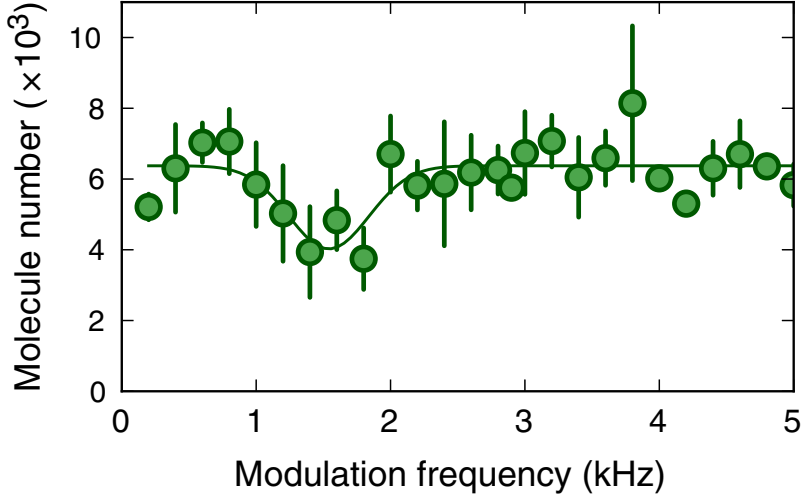


Figure 5-16: Parametric modulation of the 1319 nm ODT to determine molecular trap frequencies. A loss in the molecule number is observed at 1.54 kHz, indicating a radial trapping frequency of 770 Hz for the NaLi molecules.

looking for a loss resonance at twice the radial trapping frequency, $2f_{r,\text{mol}}$. Fig. 5-16 shows the results of modulating the trap for 1 s at 10 % of the trap depth, revealing a radial trap frequency of $f_{r,\text{mol}} = 770$ Hz. This value is consistent with a simple model of NaLi that assumes the molecule to have a single transition with unity oscillator strength at 830 nm and a linewidth 6 MHz, which gives a radial trap frequency of $f_{r,\text{mol}} = 800$ Hz, axial trap frequency of $f_{z,\text{mol}} = 7$ Hz, and trap depth of $U_{\text{mol}} = 21 \mu\text{K}$ (here we have used the well known equations for a Gaussian beam ODT; see eq. 10 and Sec. IV.A of [145]). Such a model is valid since the dominant Franck-Condon factors for the triplet ground state NaLi molecule are at approximately 830 nm transitions (819 nm for $c^3\Sigma^+$ and 840 nm for $b^3\Pi$ potentials, see Fig. 4-3 and Fig. 5-14, respectively), and the Franck-Condon factors obey a sum rule which adds to unity [146]. Since the $c^3\Sigma^+$ and $b^3\Pi$ potentials dissociate to the excited ${}^2P_{1/2}$ and ${}^2P_{3/2}$ transitions in Li, respectively, this simplified molecular transition model assumes the same transition strengths as the combined D_1 and D_2 transitions in a free Li atom. The 7 Hz axial trapping frequency obtained from this analysis is consistent with the oscillations observed in the lifetime measurement (Fig. 5-15, inset).

The temperature of the molecules was measured by imaging time-of-flight (TOF)

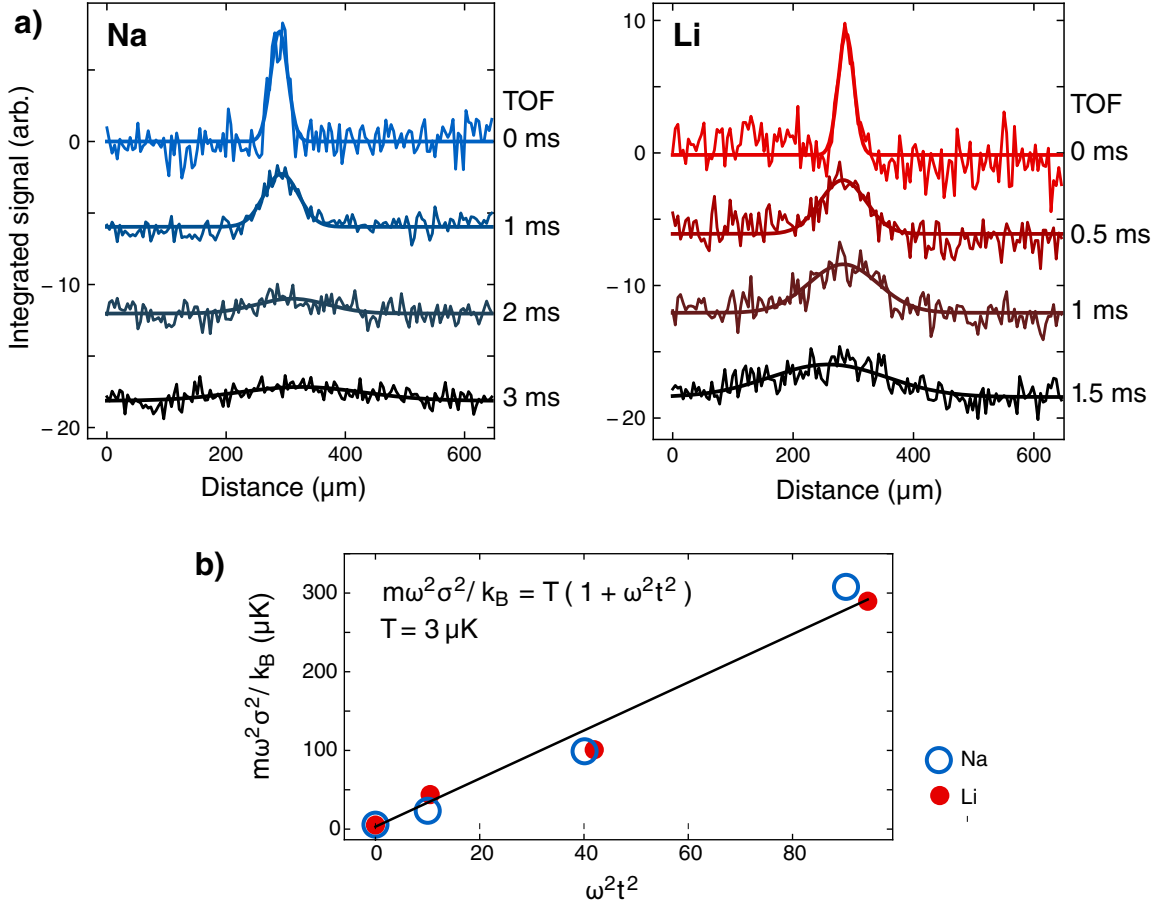


Figure 5-17: Time-of-flight distributions of dissociated molecules. After a 1 s hold time at low field, the molecules were dissociated and allowed to expand in time-of-flight. a) The integrated density distributions of side images of Na and Li at various TOF times. The distributions were fit to Gaussian profiles, as expected for a thermal gas. Note the Li expands faster than Na due to its light mass. b) The Gaussian widths as a function of TOF time used to extract the sample temperature. ω is the radial trapping frequency for the relevant species ($\omega_{\text{Na}} = 0.5 \text{ kHz}$, $\omega_{\text{Na}} = 1 \text{ kHz}$), σ is the measured Gaussian profile radius, and m is the species mass.

distributions of the dissociated atoms to obtain $T_{\text{mol}} = 3 \mu\text{K}$ (Fig. 5-17). This measurement is consistent with the calculated ODT trap depth of $21 \mu\text{K}$ ¹⁸, however one must be careful to consider how the process of molecule dissociation can affect the sample temperature. The STIRAP process is a coherent, single-body effect which only changes the internal (vibrational) degree of freedom, and does not affect molecular motion¹⁹. However, Feshbach dissociation can non-trivially affect the tem-

¹⁸A typical rule-of-thumb is that the sample temperature will be 10 % of the trap depth.

¹⁹The STIRAP beams actually do give the molecules a small momentum kick from absorbing an

perature. Consider an NaLi molecule moving with kinetic energy and temperature $(m_{\text{Na}} + m_{\text{Li}})v^2 = k_B T_{\text{mol}}$, which upon perfect dissociation will leave two free atoms with energies $m_{\text{Li}}v^2 < m_{\text{Na}}v^2 < k_B T_{\text{mol}}$. Thus the TOF measurement of free atoms may be underestimating the molecular sample temperature²⁰. A competing effect is that a diabatic magnetic field jump for Feshbach dissociation can result in coupling the molecules to higher energy scattering states which heats the sample [147, 148]. The molecules may “overshoot” the resonance and add relative kinetic energy between the Na and Li atoms, which in the center-of-mass frame results in more heating of the lighter Li atoms. Our observations show the same temperature for both dissociated Na and Li (Fig. 5-17 b), which could mean the two aforementioned effects cancel one another. We did not pursue a careful study of these effects any further, but rather placed conservative error bounds on the measured temperature $T_{\text{mol}} = 3_{-1.5}^{+3} \mu\text{K}$.

Assuming the NaLi molecules obey a classical thermal in-trap distribution, we can use the measured temperature and trap frequencies to calculate the peak molecule density to be $n_{\text{mol}} = 5(4) \times 10^{10} \text{ cm}^{-3}$, from which we can determine the degeneracy parameter $T/T_F \approx 100$. With these measurements, we find the 4.6 s molecule lifetime corresponds to a density normalized loss coefficient of $K_{\text{meas}} = 1.6 \pm 1.2 \times 10^{-11} \text{ cm}^3/\text{s}$. We have also performed measurements of the atom-molecule lifetimes (by omitting the resonant clean-out pulse for one of the species²¹), resulting in $< 1 \text{ ms}$ lifetimes corresponding to much faster loss coefficients of $K_{\text{meas,atom-mol}} \approx 3 \times 10^{-9} \text{ cm}^3/\text{s}$. The density normalized loss rates can be compared to theoretical predictions, specifically the universal model for ultracold collisions [43]. The universal model assumes a worst-case scenario where each two-body collision has 100 % probability of losing both collision partners at short-range, resulting in a loss rate governed only by the

upleg photon and emitting a downleg photon. However, in our case the beams are co-propagating, and this momentum difference corresponds to negligible added energy of 86 pK.

²⁰If the atomic sample is allowed to thermalize then both species will have the temperature $\frac{1}{2}T_{\text{mol}}$, from an application of the equipartition theorem on two degrees of freedom. But in our experiment we held the sample for 10 ms after dissociation which is not enough time for a mixture of Na and Li at densities of $n \sim 10^{10} \text{ cm}^{-3}$ to equilibrate.

²¹Since the atom-molecule lifetime were so short, we did not need to perform the double clean-out pulse and field drop as we did to measure the long lifetimes. Thus the sequence was similar to Fig. 5-12 a.

strength of the long range (van der Waals) attraction. The universal model is the quantum analogue of the classical Langevin collisional model (commonly used for ion collisions [149]). The density normalized loss coefficients for *s*- and *p*-wave collisional channels are given by

$$K_{L=0} = g \frac{4\pi\hbar}{\mu} \bar{a} \quad K_{L=1}(T) = 1513 \bar{a}^3 k_B T / h \quad (5.3)$$

where $g = 2(1)$ for (non-)identical particles, μ is the reduced mass of the collision partners, and $\bar{a} = (2\pi/\Gamma(1/4)^2)(2\mu C_6/\hbar^2)^{1/4}$ is the van der Waals length. The C_6 values for molecule-molecule and molecule-atom collisions are well approximated by summing over the known C_6 values for the atom-pairs which make up the collision partners (e.g. $C_6^{\text{NaLi+Li}} = C_6^{\text{Na+Li}} + C_6^{\text{Li+Li}}$) as has been previously done in [150, 151] (see Appendix B for specific values of coefficients in the NaLi molecule). There is also a contribution to the C_6 from the dipole-dipole interactions of NaLi, however this is only a $< 1\%$ effect [43]. At the ultracold temperatures considered here, we expect $K_{L=1} \ll K_{L=0}$, since *p*-wave collisional partners must tunnel through the centrifugal barrier before suffering the effects of any short-range loss. This is the primary reason we expected NaLi to have a long lifetime regardless of any possible loss mechanisms: the NaLi molecule is fermionic with the smallest C_6 coefficient of the bi-alkalis, thus exhibiting very slow inelastic collision rates given by $K_{L=1}$.

Fig. 5-18 compares the measured loss coefficients to predictions based on the universal model. The atom-molecule loss coefficients are in close agreement with the universal predictions for *s*-wave collisions, implying that atom-molecule collisions are maximally inelastic. This is expected, since the atoms and molecules are in opposite spin states ($m_S = -1/2$ and $m_S = 1$, respectively), which immediately allows for spin-changing collisions. The molecule-molecule loss rate is significantly lower than the *s*-wave universal rate due to their fermionic nature and Pauli blocking of *s*-wave collisions. The low molecule-molecule loss rate is a confirmation that we have prepared a single-state sample of triplet ground state NaLi molecules. However, the rate is not as low as we would expect, still being a factor of ~ 3 faster than the *p*-wave universal

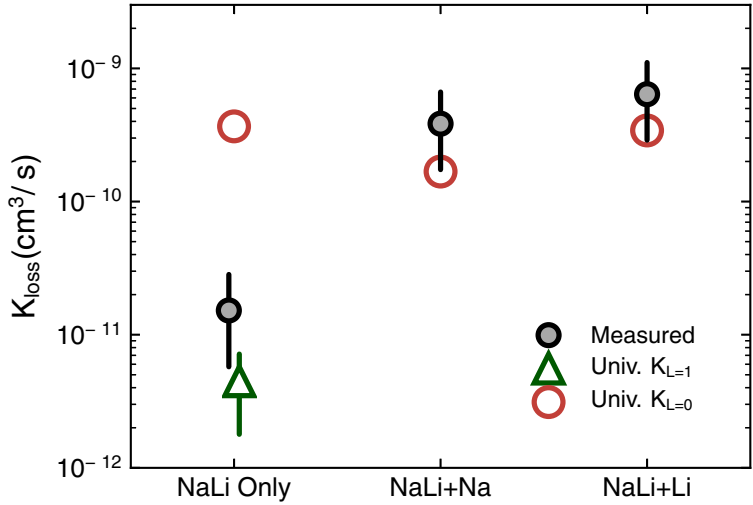


Figure 5-18: Loss coefficients in NaLi collisions. The measured density normalized loss coefficients for molecule-molecule and molecule-atom collisions are shown with black circles. Hollow red circles are the expected universal loss rates for *s*-wave collisions, $K_{L=0}$. The green triangle is the *p*-wave universal rate prediction, $K_{L=1}$. The atom-molecule collisions show a loss rate consistent with the *s*-wave universal prediction. The molecule-molecule collisions exhibit a rate much lower than the *s*-wave universal prediction, indicating Pauli blocking of *s*-wave collisions. The error bars stem from the temperature uncertainty and density averaging in the harmonic trap.

rate. We suspect the higher loss rate is still due to single-body scattering of the 1319 nm ODT. Although the 1319 nm ODT allowed for a factor of 30 improvement in lifetime over the 1064 nm ODT, it may still drive bound-to-bound transitions to the $b^3\Pi$ potential that extends down to 1800 nm transition wavelengths (Fig. 5-14).

5.5.3 Electron spin resonance spectroscopy

The uniqueness of triplet NaLi molecules is their long lifetime while having both electric and magnetic dipole moments. In prior ultracold bi-alkali formation experiments, it was typical to measure the electric dipole moment via Stark spectroscopy [35, 45, 46, 48, 47], which showed good agreement with theoretical predictions. In contrast to these works, here we focus on the aspect of NaLi molecules that has previously not been studied in the world of ultracold bi-alkali molecules: the magnetic dipole moment.

We studied the magnetic dipole transitions of the NaLi molecule by electron spin resonance (ESR) spectroscopy. The ultracold molecular sample was held in the 1319 nm ODT at low field (~ 10 G, during the variable hold in Fig. 5-13) and exposed to radio-frequency (RF) pulses. We knew the initial molecular rotational state to be $N_g = 0$, the spin state to be $|S = 1, m_S = 1\rangle$, and nuclear spin states $|I_{\text{Na}} = 3/2, m_{I,\text{Na}} = 3/2\rangle$ and $|I_{\text{Li}} = 1, m_{I,\text{Li}} = 1\rangle$. As in alkali atoms, we expected these spins to be coupled via hyperfine coupling of the form

$$H_{\text{HF}} = a_{\text{Li},\text{Na}} \vec{S} \cdot \vec{I}_{\text{Li}} + a_{\text{Na}} \vec{S} \cdot \vec{I}_{\text{Na}} \quad (5.4)$$

where $a_{\text{Li},\text{Na}}$ are the hyperfine coupling constants. This Hamiltonian is diagonalized by the total angular momentum eigenstates $F = S + I_{\text{Na}} + I_{\text{Li}}$. Thus our initial molecular state after STIRAP was the stretched state $|F = 7/2, m_F = 7/2\rangle$, and the first transition we probed with ESR spectroscopy was $|F = 7/2, m_F = 7/2\rangle \leftrightarrow |F = 7/2, m_F = 5/2\rangle$ with an expected linear Zeeman shift of ~ 0.8 MHz/G. Fig. 5-19 shows a sample ESR spectrum for this transition in the NaLi molecule. ESR spectra of the free atom Na $|F = 1, m_F = 1\rangle \leftrightarrow |F = 1, m_F = 0\rangle$ transition and the Li $|F = 1/2, m_F = 1/2\rangle \leftrightarrow |F = 1/2, m_F = -1/2\rangle$ transition were used to calibrate the magnetic field²². The ESR spectra were taken using narrow Landau-Zener sweeps of the RF frequency to transfer molecules to the $|F = 7/2, m_F = 5/2\rangle$ state which is not involved in the reverse STIRAP transfer, thus the ESR resonance appears as molecule loss. A wide range of Rabi frequencies, 1-100 kHz, were employed over exposure times of 10-400 ms, depending on the desired spectrum resolution. Fig. 5-19 b shows the measured Zeeman shift of the $|F = 7/2, m_F = 7/2\rangle \leftrightarrow |F = 7/2, m_F = 5/2\rangle$ molecular transition, exhibiting a quadratic deviation from the low-field linear Zeeman shift. By measuring this deviation, we could begin to calibrate the hyperfine constants in numerical diagonalizations of eq. 5.4 and predict the positions of spin-flip transitions to other F states. Fig. 5-20 shows the measured hyperfine structure and spectra to all other

²²The free atom experiments were not done simultaneously with the molecular sample, i.e. they were performed by repeating the full experimental sequence but by omitting the molecule formation and resonant cleaning steps.

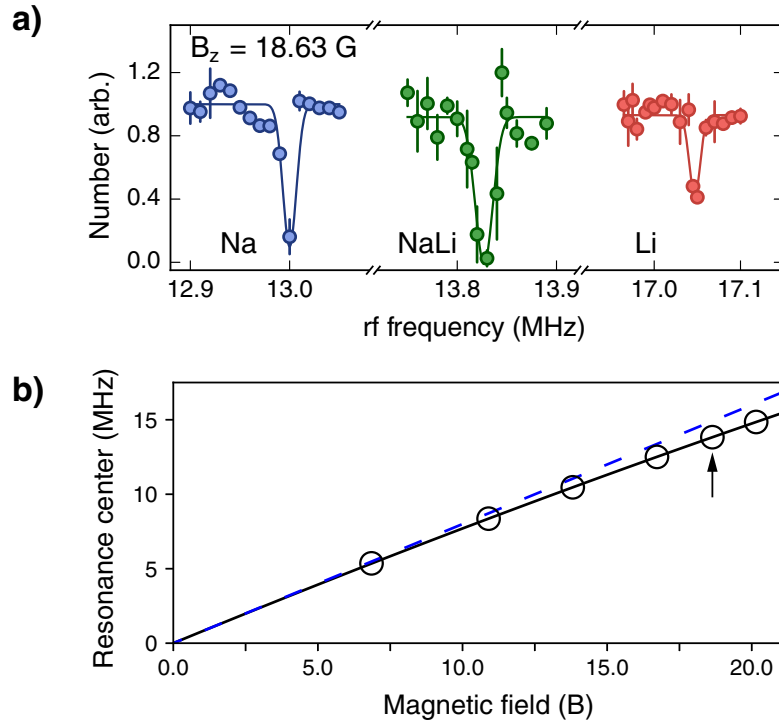


Figure 5-19: Electron spin resonance spectroscopy of the NaLi molecules. a) RF spectra for the Na $|F=1, m_F=1\rangle \leftrightarrow |F=1, m_F=0\rangle$, NaLi $|F=7/2, m_F=7/2\rangle \leftrightarrow |F=7/2, m_F=5/2\rangle$, and Li $|F=1/2, m_F=1/2\rangle \leftrightarrow |F=1/2, m_F=-1/2\rangle$ transitions are shown, revealing a unique resonance which can identify the NaLi molecules. Such spectra were taken at various mangetic fields, and the position of the NaLi resonance in shown in (b). The measured resonance positions (hollow circles) deviate from the linear Zeeman shift (dashed blue lines). The black solid line is the result of numerically solving eq. 5.4, showing excellent agreement with the data.

transitions which were accessible with magnetic dipole selection rules from our initial state. These spectra are well fit using the hyperfine Hamiltonian eq. 5.4 with constants $a_{\text{Li}} = 74.61(3)$ MHz and $a_{\text{Na}} = 433.20(3)$ MHz. Interestingly, these values are almost exactly half of the free atomic value for Na and Li. This is not unexpected, as triplet NaLi is a very weakly bound molecule, thus each of the two electrons is localized to its respective atom and has the same atomic hyperfine interactions. Since we consider the total spin of the two electrons in our hyperfine Hamiltonian, each of the hyperfine constants is half the free-atom value.

The use of RF to directly manipulate the NaLi molecule's magnetic moment is a new technique in the field of ultracold dipolar molecules. Fig. 5-19 a illustrates

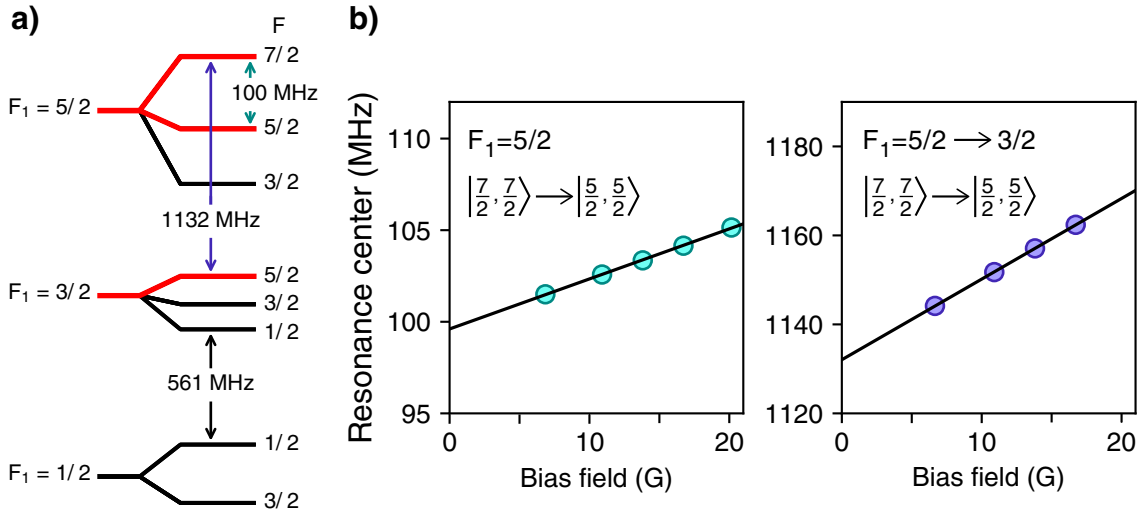


Figure 5-20: Hyperfine structure and transitions in the NaLi triplet ground state molecule. a) Energy level diagram of the NaLi hyperfine states. The states accessible from our initial state $|F=7/2, m_F=7/2\rangle$ are marked in red. b) The Zeeman shifts measured for the two accessible F changing transitions, fit to a numerical diagonalization of the hyperfine Hamiltonian, eq. 5.4.

that the ESR spectra of NaLi can be used to *directly* identify and probe the NaLi molecule. For example, a careful measurement of the width of these spectra at low Rabi frequencies could be used to directly measure the molecule temperature via inhomogeneous Zeeman broadening in a magnetic trap, foregoing the complications of using dissociated atoms (as discussed in the previous section). This scheme is also experimentally simple, allowing for the manipulation of the molecules' hyperfine states without the use of an intermediate state in two-photon RF [129] or optical [48] transitions.

Chapter 6

Summary and outlook

The work of this thesis has described the experimental efforts in spectroscopy and preparation of ultracold samples of NaLi molecules. Using PA spectroscopy, we have mapped out the vibrational states of the NaLi excited $c^3\Sigma^+$ potential. This was the first measurement of the excited triplet states of the NaLi molecule, and the first observation of PA in a Na-Li mixture. By adding a second laser to this experiment, we performed two-photon spectroscopy of the triplet ground ($a^3\Sigma^+$) potential, and spectroscopically identified the triplet ro-vibrational ground state. Building on the prior work with Feshbach molecules in the Ketterle group [54], we formed Feshbach molecules and transferred them to the ro-vibrational triplet ground state using a coherent two-photon STIRAP. Finally, we began to characterize some basic properties of the triplet ground state NaLi molecules, including their lifetime and the novel feature of a magnetic moment in a heteronuclear molecule [60]. We now take the time to reflect on these results, and consider what place NaLi has in the future of ultracold molecules experiments.

6.1 Collisional studies

The most notable property of the NaLi molecule that we have measured is its long lifetime of 5 s at a density of $5 \times 10^{10} \text{ cm}^{-3}$, which is expected to be even a factor of 10 longer if it were not limited by scattering from the trapping laser (as discussed in

Sec. 5.5.1). Such long lifetimes of the triplet NaLi molecule are almost contradictory to its description: The triplet state is highly excited with many energetically allowed singlet decay channels, with even more collisional loss channels available from the reactivity of NaLi molecule collisions. Of course, the long lifetime we have measured does *not* imply the molecules are collisionally stable, but is rather a reflection of the inherently low universal rates in the NaLi molecule, which fundamentally stems from its small C_6 coefficient. Thus the NaLi molecule lifetime is impervious to possible new two-body loss mechanisms, such as the “sticky collisions” which seem to be severely limiting the lifetimes of singlet, non-reactive bi-alkali species [46, 48, 45].

The observation of a long lifetime of the NaLi molecule approaching the universal rate is an interesting result, however the ultimate goal is to observe elastic collisions with the NaLi molecule (i.e. a lifetime longer than the universal limit) which could be used for evaporative cooling. Towards that end, the electric and magnetic dipole moments available in the NaLi molecule can facilitate interesting collisional studies. Consider for example a collisional study of a mixture of triplet NaLi with free Na atoms. In Chapter 5, we have measured the lifetime of this mixture to be quite short (~ 1 ms), however this was using Na atoms with an opposite spin orientation¹ to that of the molecule, thus spin-changing collisions were possible. If a spin-polarized mixture of Na and NaLi was used the results could be quite different: The reaction $\text{NaLi} + \text{Na} \rightarrow \text{Na}_2 + \text{Li}$ is energetically forbidden so long as we consider only molecules in the triplet spin state [44]. While the use of spin-polarization to avoid inelastic collisions to lower-lying spin states has worked well in atomic systems (consider for example, sympathetic cooling of ${}^6\text{Li}$ with ${}^{23}\text{Na}$ [9]), whether this will result in favorable molecule-atom collisions is still an open question. Collisional spin-relaxation in ${}^3\Sigma$ molecules has been previously studied showing that molecules with a large rotational constant have lower inelastic spin-relaxation rates, a result that is favorable considering the light mass of NaLi molecules [152]. Furthermore, it has been calculated that collisional spin-relaxation can be controlled in magnetically

¹The Na was in the $|1\rangle$ state, the lowest Zeeman hyperfine state, and the molecules were in their highest (stretched) Zeeman state.

and electrically dipolar molecules by a careful application of external magnetic and electric fields [153, 52]. With spin-relaxation (theoretically) under control, there is still the question of sticky collisions: Inelastic rates from sticky collisions scale with mass [49], and since the collision $\text{NaLi} + \text{Na}$ involves relatively light masses one would not expect severe losses, however an experimental demonstration is still lacking. If all of these effects—reactivity, spin-relaxation, and sticky collisions—can be brought under control, then sympathetic cooling of triplet NaLi molecules using Na atoms is a real possibility, which would be an enormous step forward to reaching quantum degeneracy with dipolar molecules.

The preceding example is just one possibility of an evaporation scheme unique to the NaLi molecule. Another common proposal is to use a 2D trapping geometry and a transverse electric field to polarize the molecules such that the dipole-dipole interactions are repulsive, which should stabilize against sticky collisions or other short-range loss processes [154]. All such schemes find themselves at the confluence of many different collisional effects which need to be carefully understood. The best-case outcome is a method of evaporative cooling of dipolar molecules, while the worst-case is a series of collisional studies with unfavorable results. Nonetheless, understanding these kinds of collisional properties is a key area of research at the forefront of what every (bi-alkali, directly cooled, etc.) molecules experiment will need to understand in order to reach quantum degeneracy. As illustrated in the example of $\text{NaLi} + \text{Na}$ collisions, the triplet NaLi system—with an electric and magnetic dipole moment—is well suited to study many different effects in cold collisions and quantum chemistry which are relevant to the entire field of cold molecules.

6.2 Simplifying experiments

The difficulty of dealing with molecular collisions is evident in the recent history of the field: The first formation of an ultracold dipolar molecule, KRb , was nearly 10 years ago, and a quantum degenerate sample of dipolar molecules has still not been achieved. Collisional loss is certainly one problem, but another is the sheer complexity

of these experiments. Dual-species quantum degenerate mixtures, Feshbach molecule formation, narrow laser locks for STIRAP—all of these technical burdens build a high entry barrier to dipolar molecule formation experiments². Thus, we turn the discussion towards a different question: Can the NaLi system simplify experiments with molecules?

One experimental advantage of NaLi is in the ultracold atom number prior to molecule formation. The collisional properties of Na-Li mixtures are favorable, and it is typical to form a quantum degenerate Bose-Fermi mixture of 5 million atoms in both species, about a factor of 10 larger than other bi-alkali experiments [155, 136, 156, 157]. These initially large atomic samples allow a competitive number of ground state molecules (typically 3×10^4), despite being bottlenecked by the poor Feshbach molecule formation efficiency of only 3 %. Indeed, the Feshbach resonances in NaLi are narrow and the most difficult to work with among the bi-alkalis. However, as discussed in Sec. 4.5.2, recent experiments in Sr_2 molecule formation have demonstrated the use of STIRAP from an initial collisional state—i.e. without the use of Feshbach molecules [138]. By increasing the upleg coupling using a highly-vibrationally excited state in the $c^3\Sigma^+$ NaLi potential and squeezing the Na-Li mixture to high density, it is possible that free-to-bound STIRAP could form weakly bound NaLi molecules which could then be transferred using the “typical” pathway (Sec. 4.2) to the triplet ground state³. Even if the efficiency of such a process is a few percent, the large initial Na-Li atom number would allow for the formation of $\sim 10^4$ molecules without the technical complexity of using a Feshbach resonance. Furthermore, since triplet NaLi molecules have a magnetic moment and thus magnetically trappable, such a free-to-bound STIRAP could be done entirely in a magnetic trap. The prospect of starting with an ultracold magnetically trapped Na-Li mixture and coherently forming molecules with only a laser pulse would greatly simplify the experiment (compare to

²We have not mentioned the difficulties of direct cooling experiments, but they too have significant technical overhead. For example, see [26].

³Note that the first (free-to-bound) STIRAP would be to a weakly bound vibrational state (with a binding energy on a few GHz), thus making it possible to use frequency shifting elements (such as an electro-optic modulator) for light generation, rather than the burdensome cavity locks described in Chapter 2.

the current molecular production sequence, as was shown in Fig. 5-13).

Another even simpler method for producing triplet NaLi molecules is by optical pumping (described in Sec. 4.5.1). Since the triplet ground potential is so shallow that it only contains 11 vibrational states, PA followed by spontaneous decay has a high probability of decaying to the triplet ro-vibrational ground state. Thus it may be possible to produce triplet ground state NaLi molecules simply by PA in a dual-species MOT [158, 159]. Detection may be possible with direct imaging of molecules on the strong downleg transition ($a^3\Sigma^+$, $v_g=0$ to $c^3\Sigma^+$, $v^*=11$, see Sec. 4.2), a technique already demonstrated in KRb [160]. While such a scheme introduces issues with incoherent production and a “dirty” sample, these problems could be circumvented using a combination of magnetic trapping and resonant clean-out of atoms and unwanted molecular states (as we have done in Sec. 5.5.1).

Thus, we see that there are possibilities for a much simpler experimental realization of triplet NaLi molecules. These techniques are not only applicable in NaLi: Although the technique of pumping is particularly well suited for obtaining ground state triplet molecules, the free-to-bound STIRAP could be employed in any ultracold association experiment (especially those in which the Feshbach resonances are impractical to use [92]). Nevertheless, the large atom numbers achievable in Na-Li mixture experiments provide a unique advantage to any ultracold association scheme.

6.3 Concluding remarks

In the near future, it is clear that triplet NaLi molecules have a place in performing interesting quantum chemistry studies and simplifying the experimental difficulty of molecule production. What about the far future? When will a lattice of dipolar molecules be available for quantum simulation? Here, the answer is much less clear. Collisional issues have been the primary barrier towards forming high filling fractions in optical lattice experiments [38], which highlights the importance of understanding molecule collisions for all experiments going forward. An alternative style to producing a molecule-based quantum simulator is with individual assembly, where the recent

advent of ultracold atom microscopy and high-resolution optical trapping could allow for assembly of a many-body system molecule-by-molecule, thus avoiding collisions altogether [161, 162, 40]. Still, microscopy experiments have their own set of technical challenges, such as how a dipolar molecule may behave at very short distances near a microscope objective.

Though there are clearly great challenges in the field of cold molecules, there is also no shortage of physics to be studied. The NaLi molecule in its triplet state provides a new system and a unique approach to pushing the field forward. The work of this thesis has been only to form these molecules, placing them on the cusp of further scientific discovery.

Appendix A

Magnetic field stability circuit calibration

Constructing the feedback circuit for creating magnetic fields with a relative stability of 10^{-6} required extensive testing of the feedback with different components (details in Chapter 2). Fig. A-1 shows the current modulation bandwidths with using a series IGBT (Mitsubishi CM1000HA-24H) in comparison to a parallel transistor (NTE2541), used in a test circuit similar to Fig. 2-6 but *without* the inductive coil, instead with a non-inductive cable as the load. As expected, the parallel transistor is able to modulate current much faster than the IGBT, however when driving an inductive coil the modulation bandwidth of both devices was limited by LC resonances from the coil and some stray capacitance, limiting the modulation bandwidth to ~ 20 kHz (this limitation is the cause of the servo-bumps in Fig. 2-7). Fig. A-2 shows the performance of the active noise cancellation circuit when tested with injected noise from inductive coupling to another coil. Fig. A-3 and Fig. A-4 compares the noise performance for current sensing using a Hall probe (FW Bell CLN-300 and LEM LF 310-S) and fluxgate magnetometer (LEM UltraStab IT 700-S). We found the fluxgate magnetometer to have far superior noise performance to the Hall probes, and thus the fluxgate sensor was chosen for the noise cancellation circuit. Note that Fig. A-3 shows the noise performance of the CLN-300 Hall probe, but the performance of the LF 310-S probe is similar (-130 dB noise at 1 kHz) and a noise-spectrum can be found on

its datasheet. In all figures, the decibel level is calculated as $20 \log (V_{\text{noise}}/V_{\text{DC}})$ where V_{noise} is the noise spectral density of the measurement device in units of $\text{V}/\sqrt{\text{Hz}}$ and V_{DC} is a *reference* voltage which is given in the figure captions.

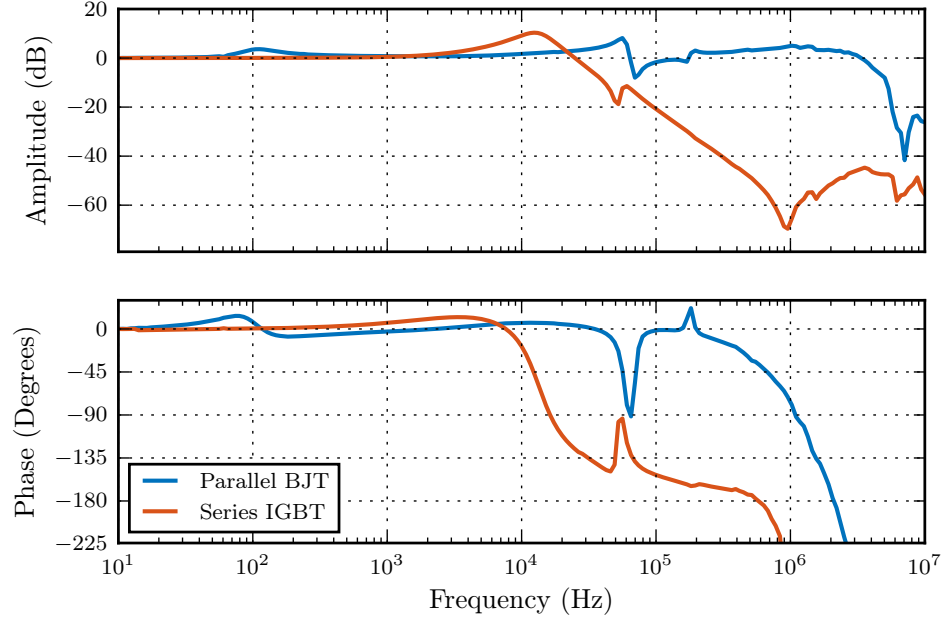


Figure A-1: Modulation bandwidth of series IGBT vs. parallel transistor. The amplitude and phase of the modulation produced by a series IGBT (red) and a parallel transistor (blue) are shown when driving a non-inductive load (i.e., we replaced the coil with a short cable.) The parallel transistor shows a much higher modulation bandwidth up to 10 MHz. The notches in modulation at ~ 50 kHz are of unknown origin, however they were worsened when driving the (inductive) coil. Driving an inductive coil introduced resonances at ~ 20 kHz, severely limiting the modulation performance of the parallel transistor, however we did not debug this issue further.

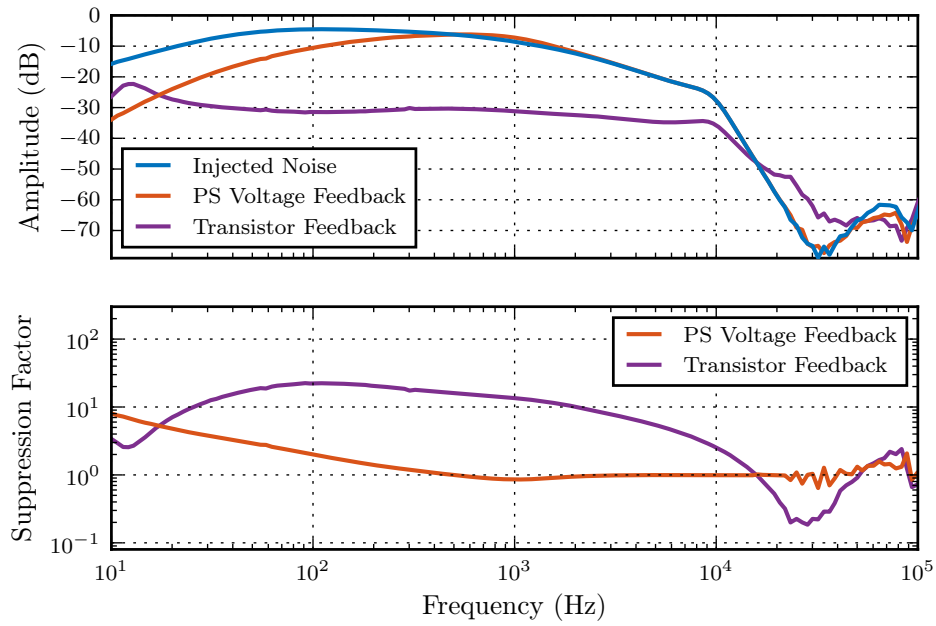


Figure A-2: Magnetic field stabilization test using injected noise. Current modulation was induced in the Feshbach coil using cross-inductive coupling from modulation in the spin-flip bias coil to simulate noise (top, blue curve). The injected modulation was then suppressed using only the slow feedback to the Feshbach power supply voltage control (red curves), and the full feedback utilizing both the slow path and the fast transistor feedback (purple curves). The current was measured using an LEM Ultra-Stab IT 700-S. The top diagram shows the measured relative modulation amplitude, showing injected noise up to 10 kHz. In the top diagram, the reference level for the decibel calculation is arbitrary (it was a reference signal from a network analyzer) and is physically meaningless. The bottom diagram shows the noise suppression factor when using active feedback, calculated from the difference in curves of the top diagram. In the bottom diagram, a servo-bump is visible when using full transistor feedback which worsens noise performance at ~ 30 kHz.

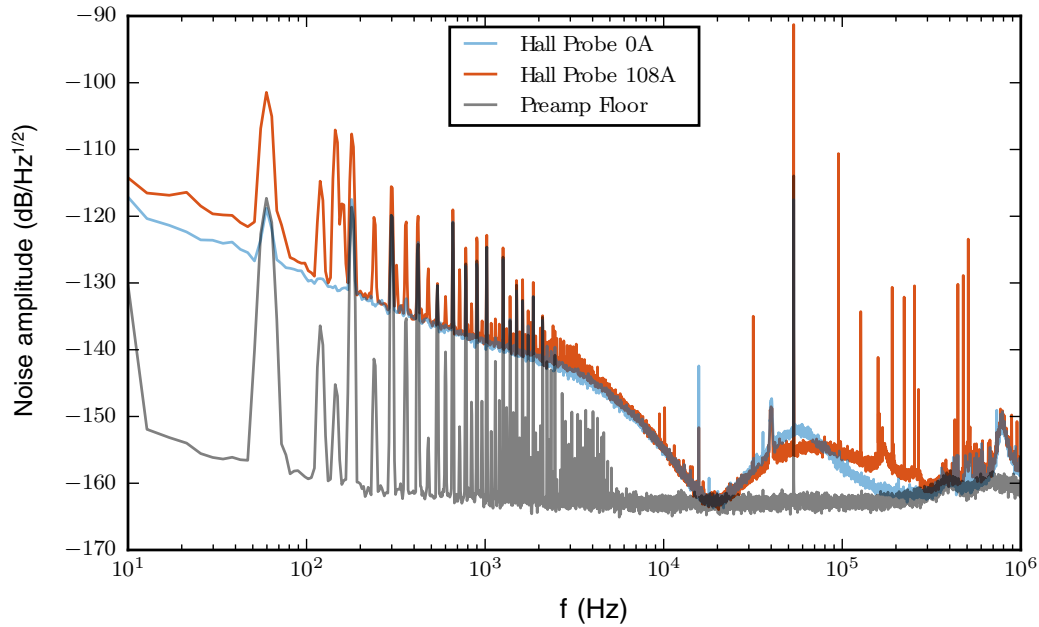


Figure A-3: FW Bell CLN-300 Hall probe noise performance. The noise spectra of the pre-amplifier without a Hall probe connected (gray), with the Hall probe on but measuring zero current (blue), and with the Hall probe measuring 108 A of current (red) are shown. All noise spectra are referenced to the Hall probe signal output when measuring 108 A of current. We see that the noise in the current measurement is dominated by the Hall probe, and any additional noise from the coil power supply is only slightly visible in the Hall sensor.

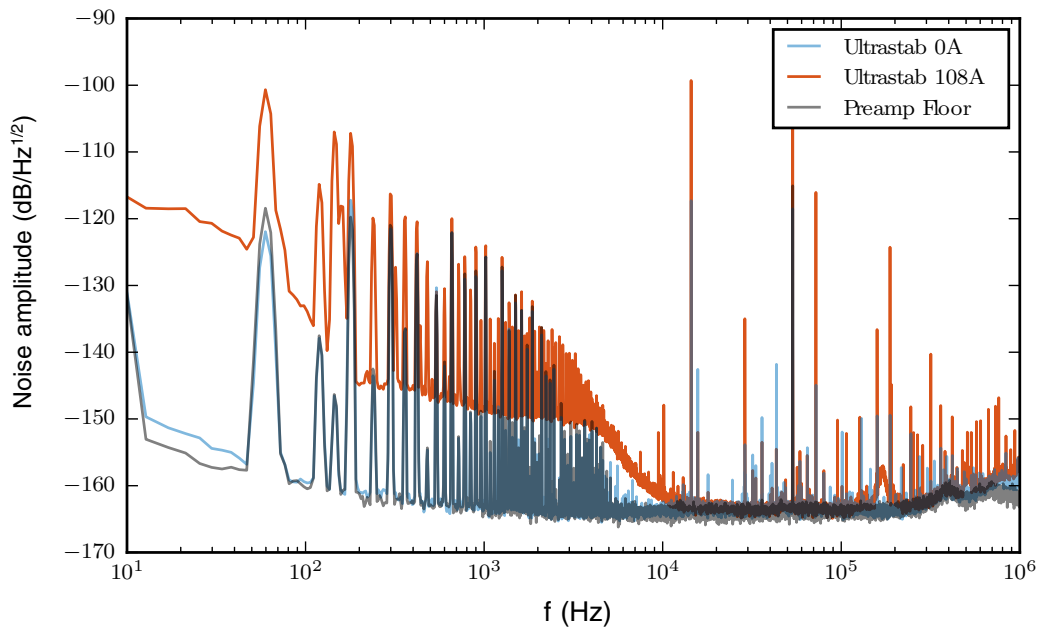


Figure A-4: LEM UltraStab IT 700-S fluxgate magnetometer noise performance. The noise spectra of the pre-amplifier without the fluxgate magnetometer connected (gray), with the fluxgate magnetometer on but measuring zero current (blue), and with the fluxgate magnetometer measuring 108 A of current (red) are shown. All noise spectra are referenced to the fluxgate magnetometer signal output when measuring 108 A of current. In this case the fluxgate magnetometer shows impressive noise performance, barely adding any noise to the system when measuring a perfect (zero) current. When the current is switched to 108 A, the fluxgate magnetometer is able to clearly measure the noise of the coil power supply.

Appendix B

Dispersion coefficients for Na, Li, and the NaLi molecule

The ground state C_6 coefficients from theoretical calculations for Na and Li are $C_{6,\text{Li-Li}} = 1389$ au, $C_{6,\text{Na-Na}} = 1556$ au, $C_{6,\text{Na-Li}} = 1467$ au [50]. The $C_{6,\text{mol}}$ for a molecule has two contributions, from the electronic excitation (similar to atoms), and an additional term originating from rotational excitations of the permanent dipole moment, $C_{6,\text{mol}}^{(\text{el})} + C_{6,\text{mol}}^{(\text{rot})}$. The electronic contribution can be approximated by summing over all pair-wise atomic dispersion coefficients, i.e. $C_{6,\text{mol}} = C_{6,\text{Li-Li}} + C_{6,\text{Na-Na}} + 2C_{6,\text{Na-Li}} = 5879$ au. From second order perturbation theory, the rotational contribution can be approximated as $C_{6,\text{mol}}^{(\text{rot})} = d^4/6B$ where d is the permanent dipole moment and B is the rotational constant [43]. Table B.1 shows some relevant properties of the NaLi molecule with data compiled from literature, *ab initio* potentials, and the aforementioned dispersion coefficient approximations.

$^{23}\text{Na}^6\text{Li}$	$a^3\Sigma^+$	$X^1\Sigma^+$
Dipole moment (Debye)	0.18 [44]	0.5 [23]
Rotational Constant ($v_g = 0$) (GHz)	4.6	11.4
Polarizability (au)	365 [163]	237 [163]
Electronic C_6 (au)	5879	5879
Dipolar (rotational) C_6 (au)	6	144

Table B.1: Properties of the NaLi singlet and triplet ro-vibrational ground states.

Appendix C

Triplet *ab initio* potentials

The work in this thesis heavily utilized theoretical calculations of the NaLi triplet potentials. The ground ($a^3\Sigma^+$) triplet potential is reported in the X -representation analytic form in [85], and it is tabulated for convenience in Table C.1. This potential is based on an *ab initio* calculation slightly corrected for the position of the least bound vibrational (Feshbach) state. Prior to our experiments, the excited triplet states of NaLi were unobserved and thus we relied purely on *ab initio* potentials, also shown in Table C.1. This data was provided to us by Prof. Olivier Dulieu, to whom we are grateful. With the experimental results of Chapter 3 and Chapter 4, we were able to improve upon these potentials, and the resulting potentials and fitting methodology is reported in [58] and [59].

Table C.1: Table of *ab initio* potential values for the lowest three triplet potentials of NaLi. All values are in atomic units.

Internuclear Distance (a_0)	$a^3\Sigma^+$	$b^3\Pi$	$c^3\Sigma^+$
2.20	8.298786028	0.178444959	0.283498199
2.40	4.921037500	0.153316981	0.255513453
2.60	3.041868538	0.131343365	0.229375255
2.80	1.947723817	0.112170707	0.204847433
3.00	1.285362500	0.095472700	0.181869054
3.20	0.870649674	0.080999428	0.160572470
3.40	0.603234445	0.069509551	0.142238783
3.60	0.426266630	0.058019673	0.123905096

Continued on next page

Table C.1 – continued from previous page

Internuclear Distance (a_0)	$a^3\Sigma^+$	$b^3\Pi$	$c^3\Sigma^+$
3.80	0.306424210	0.049221901	0.108827179
4.00	0.223577634	0.042027238	0.095923772
4.20	0.165234976	0.036929826	0.086001547
4.40	0.123454347	0.031832413	0.076079322
4.60	0.093075166	0.028515972	0.068734094
4.80	0.070677026	0.026179881	0.062811473
5.00	0.053951581	0.024680354	0.058100788
5.20	0.041315011	0.023888606	0.054413934
5.40	0.031663974	0.023691731	0.051587457
5.60	0.024219000	0.023990920	0.049480342
5.80	0.018422235	0.024699563	0.047971395
6.00	0.013869604	0.025742048	0.046957101
6.20	0.010265125	0.027052795	0.046349562
6.40	0.007389717	0.028575214	0.046074445
6.60	0.005079631	0.030260658	0.046069069
6.80	0.003211354	0.032067342	0.046280700
7.00	0.001690912	0.033959384	0.046665093
7.20	0.000446231	0.035905955	0.047185228
7.40	-0.000285653	0.037880504	0.047810200
7.60	-0.000528270	0.039860147	0.048514260
7.80	-0.000711634	0.041825100	0.049275983
8.00	-0.000846497	0.043758260	0.050077559
8.20	-0.000941536	0.045644834	0.050904201
8.40	-0.001004219	0.047472096	0.051743649
8.60	-0.001040898	0.049229153	0.052585767
8.80	-0.001056870	0.050906843	0.053422203
9.00	-0.001056517	0.052497640	0.054246118
9.20	-0.001043440	0.053995617	0.055051955
9.40	-0.001020597	0.055396427	0.055835250
9.60	-0.000990410	0.056697295	0.056592483
9.80	-0.000954856	0.057897006	0.057320934
10.00	-0.000915548	0.058995868	0.058018586
10.20	-0.000873788	0.059995637	0.058684025
10.40	-0.000830625	0.060899380	0.059316362
10.60	-0.000786897	0.061711330	0.059915160
10.80	-0.000743263	0.062436660	0.060480370
11.00	-0.000700236	0.063081271	0.061012283
11.20	-0.000658210	0.063651528	0.061511471
11.40	-0.000617479	0.064154033	0.061978744
11.60	-0.000578255	0.064568070	0.062400238
11.80	-0.000540685	0.064982107	0.062821732
12.00	-0.000504865	0.065320280	0.063199892

Continued on next page

Table C.1 – continued from previous page

Internuclear Distance (a_0)	$a^3\Sigma^+$	$b^3\Pi$	$c^3\Sigma^+$
12.20	-0.000470846	0.065615658	0.063550963
12.40	-0.000438646	0.065873512	0.063876380
12.60	-0.000408258	0.066098602	0.064177605
12.80	-0.000379652	0.066295181	0.064456114
13.00	-0.000352785	0.066467020	0.064713369
13.20	-0.000327601	0.066617416	0.064950804
13.40	-0.000304038	0.066749252	0.065169815
13.60	-0.000282025	0.066865038	0.065371740
13.80	-0.000261491	0.066960919	0.065550563
14.00	-0.000242359	0.067056799	0.065729387
14.20	-0.000224556	0.067136240	0.065887457
14.40	-0.000208007	0.067206636	0.066033133
14.60	-0.000192639	0.067269171	0.066167414
14.80	-0.000178379	0.067321875	0.066286411
15.00	-0.000165159	0.067374578	0.066405408
15.20	-0.000152913	0.067419077	0.066510761
15.40	-0.000141577	0.067458999	0.066607995
15.60	-0.000131089	0.067494905	0.066697789
15.80	-0.000121394	0.067527273	0.066780740
16.00	-0.000112435	0.067556518	0.066857416
16.20	-0.000104161	0.067583001	0.066928322
16.40	-0.000096524	0.067605942	0.066991488
16.60	-0.000089477	0.067628883	0.067054655
16.80	-0.000082979	0.067648792	0.067110904
17.00	-0.000076988	0.067666963	0.067163030
17.20	-0.000071466	0.067683578	0.067211358
17.40	-0.000066379	0.067698797	0.067256192
17.60	-0.000061693	0.067712757	0.067297803
17.80	-0.000057378	0.067725583	0.067336440
18.00	-0.000053404	0.067737384	0.067372339
18.20	-0.000049746	0.067748256	0.067405707
18.40	-0.000046377	0.067757904	0.067435661
18.60	-0.000043275	0.067767551	0.067465615
18.80	-0.000040418	0.067775801	0.067491576
19.00	-0.000037803	0.067784051	0.067517537
19.20	-0.000035330	0.067791405	0.067540869
19.40	-0.000033046	0.067798227	0.067562623
19.60	-0.000030934	0.067804563	0.067582241
19.80	-0.000028979	0.067810455	0.067601859
20.00	-0.000027168	0.067815937	0.067619544
20.20	-0.000025489	0.067821045	0.067636069
20.40	-0.000023931	0.067825807	0.067651513

Continued on next page

Table C.1 – continued from previous page

Internuclear Distance (a_0)	$a^3\Sigma^+$	$b^3\Pi$	$c^3\Sigma^+$
20.60	-0.000022484	0.067830250	0.067665959
20.80	-0.000021138	0.067834399	0.067679474
21.00	-0.000019887	0.067838278	0.067692128
21.20	-0.000018722	0.067841907	0.067703980
21.40	-0.000017636	0.067845304	0.067715087
21.60	-0.000016624	0.067848486	0.067725500
21.80	-0.000015680	0.067851470	0.067735270
22.00	-0.000014797	0.067854268	0.067744438
22.20	-0.000013973	0.067856896	0.067753048
22.40	-0.000013202	0.067859152	0.067760440
22.60	-0.000012481	0.067861407	0.067767831
22.80	-0.000011806	0.067863663	0.067775222
23.00	-0.000011173	0.067865918	0.067782614
23.20	-0.000010580	0.067867850	0.067788945
23.40	-0.000010023	0.067869670	0.067794906
23.60	-0.000009501	0.067871384	0.067800521
23.80	-0.000009010	0.067873001	0.067805815
24.00	-0.000008548	0.067874525	0.067810806
24.20	-0.000008115	0.067875964	0.067815515
24.40	-0.000007707	0.067877323	0.067819960
24.60	-0.000007322	0.067878605	0.067824156
24.80	-0.000006960	0.067879817	0.067828120
25.00	-0.000006619	0.067880962	0.067831865
25.20	-0.000006298	0.067882045	0.067835407
25.40	-0.000005994	0.067883043	0.067838667
25.60	-0.000005708	0.067884040	0.067841926
25.80	-0.000005437	0.067884934	0.067844847
26.00	-0.000005182	0.067885828	0.067847768
26.20	-0.000004940	0.067886652	0.067850459
26.40	-0.000004712	0.067887434	0.067853011
26.60	-0.000004495	0.067888105	0.067855196
26.80	-0.000004291	0.067888775	0.067857381
27.00	-0.000004097	0.067889446	0.067859565
27.20	-0.000003913	0.067890116	0.067861750
27.40	-0.000003739	0.067890787	0.067863935
27.60	-0.000003574	0.067891361	0.067865711
27.80	-0.000003418	0.067892045	0.067867486
28.00	-0.000003269	0.067892563	0.067869261
28.20	-0.000003128	0.067893055	0.067870685
28.40	-0.000002994	0.067893524	0.067872108
28.60	-0.000002867	0.067893970	0.067873531
28.80	-0.000002746	0.067894395	0.067874954

Continued on next page

Table C.1 – continued from previous page

Internuclear Distance (a_0)	$a^3\Sigma^+$	$b^3\Pi$	$c^3\Sigma^+$
29.00	-0.000002631	0.067894800	0.067876377
29.20	-0.000002521	0.067895186	0.067877800
29.40	-0.000002417	0.067895553	0.067879003
29.60	-0.000002318	0.067895904	0.067880145
29.80	-0.000002224	0.067896238	0.067881235
30.00	-0.000002134	0.067896557	0.067882275
30.20	-0.000002048	0.067896861	0.067883267
30.40	-0.000001966	0.067897152	0.067884229
30.60	-0.000001889	0.067897429	0.067885120
30.80	-0.000001814	0.067897695	0.067884578
31.00	-0.000001743	0.067897948	0.067885389
31.20	-0.000001676	0.067898190	0.067886164
31.40	-0.000001611	0.067898422	0.067886906
31.60	-0.000001549	0.067898643	0.067887615
31.80	-0.000001490	0.067898855	0.067888293
32.00	-0.000001434	0.067899058	0.067888942
32.20	-0.000001380	0.067899252	0.067889563
32.40	-0.000001329	0.067899437	0.067890158
32.60	-0.000001279	0.067899615	0.067890728
32.80	-0.000001232	0.067899786	0.067891273
33.00	-0.000001187	0.067899949	0.067891796
33.20	-0.000001144	0.067900106	0.067892297
33.40	-0.000001102	0.067900256	0.067892778
33.60	-0.000001063	0.067900400	0.067893239
33.80	-0.000001025	0.067900538	0.067893681
34.00	-0.000000988	0.067900670	0.067894105
34.20	-0.000000953	0.067900797	0.067894511
34.40	-0.000000920	0.067900919	0.067894902
34.60	-0.000000888	0.067901036	0.067895277
34.80	-0.000000857	0.067901149	0.067895637
35.00	-0.000000828	0.067901257	0.067895983
35.20	-0.000000799	0.067901361	0.067896316
35.40	-0.000000772	0.067901461	0.067896635
35.60	-0.000000746	0.067901556	0.067896942
35.80	-0.000000721	0.067901649	0.067897237
36.00	-0.000000697	0.067901737	0.067897521

Bibliography

- [1] F. Papanelopoulou. Louis paul cailletet: The liquefaction of oxygen and the emergence of low-temperature research. *Notes and Records*, 67:355–373, 2013.
- [2] D. van Delft and P. Kes. The discovery of superconductivity. *Physics Today*, 63:38–43, 2010.
- [3] R. J. Donnelly. The discovery of superfluidity. *Physics Today*, 48:30–38, 1995.
- [4] M. H. Anderson, J. R. Ensher, M. R. Matthews, C. E. Wieman, and E. A. Cornell. Observation of bose-einstein condensation in a dilute atomic vapor. *Science*, 269:198–201, 1995.
- [5] K. B. Davis, M. O. Mewes, M. R. Andrews, N. J. van Druten, D. S. Durfee, D. M. Kurn, and W. Ketterle. Bose-einstein condensation in a gas of sodium atoms. *Physical Review Letters*, 75:3969–3973, 1995.
- [6] I. M. Georgescu, S. Ashhab, and Franco Nori. Quantum simulation. *Reviews of Modern Physics*, 86:153–185, Mar 2014.
- [7] S. Giorgini, L. P. Pitaevskii, and S. Stringari. Theory of ultracold atomic fermi gases. *Reviews of Modern Physics*, 80:1215–1274, 2008.
- [8] B. DeMarco and D. S. Jin. Onset of fermi degeneracy in a trapped atomic gas. *Science*, 285:1703–1706, 1999.
- [9] Z. Hadzibabic, C. A. Stan, K. Dieckmann, S. Gupta, M. W. Zwierlein, A. Gör-litz, and W. Ketterle. Two-species mixture of quantum degenerate bose and fermi gases. *Physical Review Letters*, 88:160401, 2002.
- [10] C. Chin, R. Grimm, P. Julienne, and E. Tiesinga. Feshbach resonances in ultracold gases. *Reviews of Modern Physics*, 82:1225–1286, 2010.
- [11] M. J. H. Ku, A. T. Sommer, L. W. Cheuk, and M. W. Zwierlein. Revealing the superfluid lambda transition in the universal thermodynamics of a unitary fermi gas. *Science*, 335:563–567, 2012.
- [12] S. Hüfner, M. A. Hossain, A. Damascelli, and G. A. Sawatzky. Two gaps make a high-temperature superconductor? *Reports on Progress in Physics*, 71:062501, 2008.

- [13] M. Drewsen, C. Brodersen, L. Hornekær, J. S. Hangst, and J. P. Schifffer. Large ion crystals in a linear paul trap. *Physical Review Letters*, 81:2878–2881, Oct 1998.
- [14] C. Trefzger, C. Menotti, B. Capogrosso-Sansone, and M. Lewenstein. Ultracold dipolar gases in optical lattices. *Journal of Physics B: Atomic, Molecular and Optical Physics*, 44:193001, 2011.
- [15] N. R. Cooper and G. V. Shlyapnikov. Stable topological superfluid phase of ultracold polar fermionic molecules. *Physical Review Letters*, 103:155302, 2009.
- [16] M.A. Baranov. Theoretical progress in many-body physics with ultracold dipolar gases. *Physics Reports*, 464:71 – 111, 2008.
- [17] Krzysztof Góral, Kazimierz Rzążewski, and Tilman Pfau. Bose-einstein condensation with magnetic dipole-dipole forces. *Physical Review A*, 61:051601, 2000.
- [18] K. Aikawa, A. Frisch, M. Mark, S. Baier, A. Rietzler, R. Grimm, and F. Ferlaino. Bose-einstein condensation of erbium. *Physical Review Letters*, 108:210401, 2012.
- [19] M. Lu, N. Q. Burdick, S. H. Youn, and B. L. Lev. Strongly dipolar bose-einstein condensate of dysprosium. *Physical Review Letters*, 107:190401, 2011.
- [20] H. Kadau, M. Schmitt, M. Wenzel, C. Wink, T. Maier, I. Ferrier-Barbut, and T. Pfau. Observing the rozensweig instability of a quantum ferrofluid. *Nature*, 530:194–197, 2016.
- [21] G. Pupillo, A. Micheli, M. Boninsegni, I. Lesanovsky, and P. Zoller. Strongly correlated gases of rydberg-dressed atoms: Quantum and classical dynamics. *Physical Review Letters*, 104:223002, 2010.
- [22] J. B. Balewski, A. T. Krupp, A. Gaj, S. Hofferberth, R. Löw, and T. Pfau. Rydberg dressing: understanding of collective many-body effects and implications for experiments. *New Journal of Physics*, 16:063012, 2014.
- [23] M. Aymar and O. Dulieu. Calculation of accurate permanent dipole moments of the lowest ${}^1,{}^3\Sigma^+$ states of heteronuclear alkali dimers using extended basis sets. *The Journal of Chemical Physics*, 122:204302, 2005.
- [24] J. M. Hutson and P. Soldán. Molecular collisions in ultracold atomic gases. *International Reviews in Physical Chemistry*, 26:1–28, 2007.
- [25] R. V. Krems. Cold controlled chemistry. *Physical Chemistry Chemical Physics*, 10:4079–4092, 2008.

- [26] L. Anderegg, B. L. Augenbraun, E. Chae, B. Hemmerling, N. R. Hutzler, A. Ravi, A. Collopy, J. Ye, W. Ketterle, and J. M. Doyle. Radio frequency magneto-optical trapping of caf with high density. *Physical Review Letters*, 119:103201, 2017.
- [27] E. B. Norrgard, D. J. McCarron, M. H. Steinecker, M. R. Tarbutt, and D. DeMille. Submillikelvin dipolar molecules in a radio-frequency magneto-optical trap. *Physical Review Letters*, 116:063004, 2016.
- [28] N. R. Hutzler, H.-I. Lu, and J. M. Doyle. The buffer gas beam: An intense, cold, and slow source for atoms and molecules. *Chemical Reviews*, 112:4803–4827, 2012.
- [29] E. B. Norrgard, D. J. McCarron, M. H. Steinecker, M. R. Tarbutt, and D. DeMille. Submillikelvin dipolar molecules in a radio-frequency magneto-optical trap. *Physical Review Letters*, 116:063004, 2016.
- [30] J. F. Barry, D. J. McCarron, E. B. Norrgard, M. H. Steinecker, and D. DeMille. Magneto-optical trapping of a diatomic molecule. *Nature*, 512:286–289, 2014.
- [31] M. T. Hummon, M. Yeo, B. K. Stuhl, A. L. Collopy, Y. Xia, and J. Ye. 2d magneto-optical trapping of diatomic molecules. *Physical Review Letters*, 110:143001, 2013.
- [32] S. Y. T. van de Meerakker, H. L. Bethlem, N. Vanhaecke, and G. Meijer. Manipulation and control of molecular beams. *Chemical Reviews*, 112:4828–4878, 2012.
- [33] B. K. Stuhl, M. T. Hummon, M. Yeo, G. Quéméner, J. L. Bohn, and J. Ye. Evaporative cooling of the dipolar hydroxyl radical. *Nature*, 492:396 EP –, 2012.
- [34] J. G. Danzl, E. Haller, M. Gustavsson, M. J. Mark, R. Hart, N. Bouloufa, O. Dulieu, H. Ritsch, and H.-C. Nägerl. Quantum gas of deeply bound ground state molecules. *Science*, 321:1062–1066, 2008.
- [35] K.-K. Ni, S. Ospelkaus, M. H. G. de Miranda, A. Pe'er, B. Neyenhuis, J. J. Zirbel, S. Kotochigova, P. S. Julienne, D. S. Jin, and J. Ye. A high phase-space-density gas of polar molecules. *Science*, 322:231–235, 2008.
- [36] S. Ospelkaus, K.-K. Ni, D. Wang, M. H. G. de Miranda, B. Neyenhuis, G. Quéméner, P. S. Julienne, J. L. Bohn, D. S. Jin, and J. Ye. Quantum-state controlled chemical reactions of ultracold potassium-rubidium molecules. *Science*, 327:853–857, 2010.
- [37] M. H. G. de Miranda, A. Chotia, B. Neyenhuis, D. Wang, G. Quemener, S. Ospelkaus, J. L. Bohn, J. Ye, and D. S. Jin. Controlling the quantum stereodynamics of ultracold bimolecular reactions. *Nature Physics*, 7:502–507, 2011.

- [38] B. Yan, S. A. Moses, B. Gadway, J. P. Covey, K. R. A. Hazzard, A. M. Rey, D. S. Jin, and J. Ye. Observation of dipolar spin-exchange interactions with lattice-confined polar molecules. *Nature*, 501:521–525, 2013.
- [39] A. Chotia, B. Neyenhuis, S. A. Moses, B. Yan, J. P. Covey, M. Foss-Feig, A. M. Rey, D. S. Jin, and J. Ye. Long-lived dipolar molecules and feshbach molecules in a 3d optical lattice. *Physical Review Letters*, 108:080405, 2012.
- [40] N. R. Hutzler, L. R. Liu, Y. Yu, and K.-K. Ni. Eliminating light shifts for single atom trapping. *New Journal of Physics*, 19:023007, 2017.
- [41] P. S. Żuchowski, J. Aldegunde, and J. M. Hutson. Ultracold RbSr molecules can be formed by magnetoassociation. *Physical Review Letters*, 105:153201, 2010.
- [42] R. Roy, R. Shrestha, A. Green, S. Gupta, M. Li, S. Kotochigova, A. Petrov, and C. H. Yuen. Photoassociative production of ultracold heteronuclear YbLi* molecules. *Physical Review A*, 94:033413, 2016.
- [43] P. S. Julienne, T. M. Hanna, and Z. Idziaszek. Universal ultracold collision rates for polar molecules of two alkali-metal atoms. *Physical Chemistry Chemical Physics*, 13:19114–19124, 2011.
- [44] M. Tomza, K. W. Madison, R. Moszynski, and R. V. Krems. Chemical reactions of ultracold alkali-metal dimers in the lowest-energy $^3\Sigma$ state. *Physical Review A*, 88:050701, 2013.
- [45] T. Takekoshi, L. Reichsöllner, A. Schindewolf, J. M. Hutson, C. R. Le Sueur, O. Dulieu, F. Ferlaino, R. Grimm, and H.-C. Nägerl. Ultracold dense samples of dipolar RbCs molecules in the rovibrational and hyperfine ground state. *Physical Review Letters*, 113:205301, 2014.
- [46] P. K. Molony, P. D. Gregory, Z. Ji, B. Lu, M. P. Köppinger, C. R. Le Sueur, C. L. Blackley, J. M. Hutson, and S. L. Cornish. Creation of ultracold $^{87}\text{Rb}^{133}\text{Cs}$ molecules in the rovibrational ground state. *Physical Review Letters*, 113:255301, 2014.
- [47] M. Guo, B. Zhu, B. Lu, X. Ye, F. Wang, R. Vexiau, N. Bouloufa-Maafa, G. Quéméner, O. Dulieu, and D. Wang. Creation of an ultracold gas of ground-state dipolar $^{23}\text{Na}^{87}\text{Rb}$ molecules. *Physical Review Letters*, 116:205303, 2016.
- [48] J. W. Park, S. A. Will, and M. W. Zwierlein. Ultracold dipolar gas of fermionic $^{23}\text{Na}^{40}\text{K}$ molecules in their absolute ground state. *Physical Review Letters*, 114:205302, 2015.
- [49] M. Mayle, G. Quéméner, B. P. Ruzic, and J. L. Bohn. Scattering of ultracold molecules in the highly resonant regime. *Physical Review A*, 87:012709, 2013.

- [50] A. Derevianko, J. F. Babb, and A. Dalgarno. High-precision calculations of van der waals coefficients for heteronuclear alkali-metal dimers. *Physical Review A*, 63:052704, 2001.
- [51] A. Micheli, G. K. Brennen, and P. Zoller. A toolbox for lattice-spin models with polar molecules. *Nature Physics*, 2:341–347, 2006.
- [52] E. Abrahamsson, T. V. Tscherbul, and R. V. Krems. Inelastic collisions of cold polar molecules in nonparallel electric and magnetic fields. *The Journal of Chemical Physics*, 127:044302, 2007.
- [53] P. Soldán. Lowest quartet states of heteronuclear alkali-metal trimers. *Physical Review A*, 82:034701, 2010.
- [54] M.-S. Heo, T. T. Wang, C. A. Christensen, T. M. Rvachov, D. A. Cotta, J.-H. Choi, Y.-R. Lee, and W. Ketterle. Formation of ultracold fermionic NaLi feshbach molecules. *Physical Review A*, 86:021602, 2012.
- [55] T. Wang. *Small Diatomic Alkali Molecules at Ultracold Temperatures*. PhD thesis, Harvard University, 2014.
- [56] G. Herzberg. *Molecular Spectra and Molecular Structure: Spectra of diatomic molecules*. Molecular Spectra and Molecular Structure. R.E. Krieger Publishing Company, 1989.
- [57] J.M. Brown and A. Carrington. *Rotational Spectroscopy of Diatomic Molecules*. Cambridge Molecular Science. Cambridge University Press, 2003.
- [58] T. M. Rvachov, H. Son, J. J. Park, P. M. Notz, T. T. Wang, M. W. Zwierlein, W. Ketterle, and A. O. Jamison. Photoassociation of ultracold NaLi. *Physical Chemistry Chemical Physics*, 2018.
- [59] T. M. Rvachov, H. Son, J. J. Park, S. Ebadi, M. W. Zwierlein, W. Ketterle, and A. O. Jamison. Two-photon spectroscopy of the NaLi triplet ground state. *Physical Chemistry Chemical Physics*, 2018.
- [60] T. M. Rvachov, H. Son, A. T. Sommer, S. Ebadi, J. J. Park, M. W. Zwierlein, W. Ketterle, and A. O. Jamison. Long-lived ultracold molecules with electric and magnetic dipole moments. *Physical Review Letters*, 119:143001, 2017.
- [61] A. E. Leanhardt, Y. Shin, A. P. Chikkatur, D. Kielpinski, W. Ketterle, and D. E. Pritchard. Bose-einstein condensates near a microfabricated surface. *Physical Review Letters*, 90:100404, 2003.
- [62] W. Ketterle, D. S. Durfee, and D. M. Stamper-Kurn. Making, probing and understanding bose-einstein condensates. *arXiv:cond-mat/9904034*, 1999.
- [63] W. Ketterle and M. W. Zwierlein. Making, probing and understanding ultracold fermi gases. *arXiv:0801.2500*, 2008.

- [64] A. P. Chikkatur. *Colliding and Moving Bose-Einstein Condensates: Studies of superfluidity and optical tweezers for condensate transport*. PhD thesis, Massachusetts Institute of Technology, 2002.
- [65] T. A. Pasquini. *Quantum Reflection of Bose-Einstein Condensates*. PhD thesis, Massachusetts Institute of Technology, 2007.
- [66] G.-B. Jo. *Quantum Coherence and Magnetism in Bosonic and Fermionic Gases of Ultracold Atoms*. PhD thesis, Massachusetts Institute of Technology, 2010.
- [67] E. W. Streed, A. P. Chikkatur, T. L. Gustavson, M. Boyd, Y. Torii, D. Schneble, G. K. Campbell, D. E. Pritchard, and W. Ketterle. Large atom number bose-einstein condensate machines. *Review of Scientific Instruments*, 77:023106, 2006.
- [68] W. Ketterle, K. B. Davis, M. A. Joffe, A. Martin, and D. E. Pritchard. High densities of cold atoms in a dark spontaneous-force optical trap. *Physical Review Letters*, 70:2253–2256, 1993.
- [69] D. Stamper-Kurn. *Peeking and poking at a new quantum fluid: Studies of gaseous Bose-Einstein condensates in magnetic and optical traps*. PhD thesis, Massachusetts Institute of Technology, 1999.
- [70] P. M. Notz. Development of experimental tools for photoassociation spectroscopy of ultracold lina molecules. Master's thesis, Technissche Universität Darmstadt, 2014.
- [71] C. A. Stan, M. W. Zwierlein, C. H. Schunck, S. M. F. Raupach, and W. Ketterle. Observation of feshbach resonances between two different atomic species. *Physical Review Letters*, 93:143001, 2004.
- [72] T. Schuster, R. Scelle, A. Trautmann, S. Knoop, M. K. Oberthaler, M. M. Haverhals, M. R. Goosen, S. J. J. M. F. Kokkelmans, and E. Tiemann. Feshbach spectroscopy and scattering properties of ultracold Li + Na mixtures. *Physical Review A*, 85:042721, 2012.
- [73] C. A. Christensen. *Ultracold Molecules from Ultracold Atoms: Interactions in Sodium and Lithium Gas*. PhD thesis, Massachusetts Institute of Technology, 2011.
- [74] M.V. Danileiko, V.I. Romanenko, and L.P. Yatsenko. Landau-zener transitions and population transfer in a three-level system driven by two delayed laser pulses. *Optics Communications*, 109:462 – 466, 1994.
- [75] N. V. Vitanov, A. A. Rangelov, B. W. Shore, and K. Bergmann. Stimulated raman adiabatic passage in physics, chemistry, and beyond. *Reviews of Modern Physics*, 89:015006, 2017.

- [76] E. C. Cook, P. J. Martin, T. L. Brown-Heft, J. C. Garman, and D. A. Steck. High passive-stability diode-laser design for use in atomic-physics experiments. *Review of Scientific Instruments*, 83:043101, 2012.
- [77] L. P. Yatsenko, B. W. Shore, and K. Bergmann. Detrimental consequences of small rapid laser fluctuations on stimulated raman adiabatic passage. *Physical Review A*, 89:013831, 2014.
- [78] K.-K. Ni. *A Quantum Gas of Polar Molecules*. PhD thesis, University of Colorado at Boulder, 2009.
- [79] J. W. Park. *An ultracold gas of dipolar fermionic $^{23}\text{Na}^{40}\text{K}$ molecules*. PhD thesis, Massachusetts Institute of Technology, 2016.
- [80] S. Ebadi. Narrow linewidth laser system for creation of NaLi ultracold molecules via stirap. Master's thesis, University of Toronto, 2016.
- [81] G. Di Domenico, S. Schilt, and P. Thomann. Simple approach to the relation between laser frequency noise and laser line shape. *Applied Optics*, 49:4801–4807, 2010.
- [82] L.-S. Ma, P. Junger, J. Ye, and J. L. Hall. Accurate cancellation (to millihertz levels) of optical phase noise due to vibration or insertion phase in fiber-transmitted light. *Proc. SPIE Laser Frequency Stabilization and Noise Reduction*, 2378:165–175, 1995.
- [83] M. M. Hessel. Experimental observation of the NaLi molecule. *Physical Review Letters*, 26:215–218, 1971.
- [84] F. Engelke, G. Ennen, and K.H. Meiwes. Laser induced fluorescence spectroscopy of NaLi in beam and bulk. *Chemical Physics*, 66:391 – 402, 1982.
- [85] M. Steinke, H. Knöckel, and E. Tiemann. (X)1 $^1\Sigma^+$ state of LiNa studied by fourier-transform spectroscopy. *Physical Review A*, 85:042720, 2012.
- [86] J. W. Park, S. A. Will, and M. W. Zwierlein. Two-photon pathway to ultracold ground state molecules of $^{23}\text{Na}^{40}\text{K}$. *New Journal of Physics*, 17:075016, 2015.
- [87] M. "Debatin, T. Takekoshi, R. Rameshan, L. Reichsollner, F. Ferlaino, R. Grimm, R. Vexiau, N. Bouloufa, O. Dulieu, and H.-C. Nägerl. Molecular spectroscopy for ground-state transfer of ultracold rbcs molecules. *Physical Chemistry Chemical Physics*, 13:18926–18935, 2011.
- [88] F. Munchow, C. Bruni, M. Madalinski, and A. Gorlitz. Two-photon photoassociation spectroscopy of heteronuclear YbRb. *Physical Chemistry Chemical Physics*, 13:18734–18737, 2011.
- [89] K. Aikawa, D. Akamatsu, J. Kobayashi, M. Ueda, T. Kishimoto, and S. Inouye. Toward the production of quantum degenerate bosonic polar molecules, $^{41}\text{K}^{87}\text{Rb}$. *New Journal of Physics*, 11:055035, 2009.

- [90] A. Ridinger, S. Chaudhuri, T. Salez, D. R. Fernandes, N. Bouloufa, O. Dulieu, C. Salomon, and F. Chevy. Photoassociative creation of ultracold heteronuclear ${}^6\text{Li}{}^{40}\text{K}^*$ molecules. *Europhysics Letters*, 96:33001, 2011.
- [91] D. B. Blasing, I. C. Stevenson, J. Pérez-Ríos, D. S. Elliott, and Y. P. Chen. Short-range photoassociation of LiRb. *Physical Review A*, 94:062504, 2016.
- [92] W. Dowd, R. J. Roy, R. K. Shrestha, A. Petrov, C. Makrides, S. Kotochigova, and S. Gupta. Magnetic field dependent interactions in an ultracold Li-Yb (3P_2) mixture. *New Journal of Physics*, 17:055007, 2015.
- [93] K. M. Jones, E. Tiesinga, P. D. Lett, and P. S. Julienne. Ultracold photoassociation spectroscopy: Long-range molecules and atomic scattering. *Reviews of Modern Physics*, 78:483–535, 2006.
- [94] N. Mabrouk and H. Berriche. Theoretical study of the NaLi molecule: potential energy curves, spectroscopic constants, dipole moments and radiative lifetimes. *Journal of Physics B: Atomic, Molecular and Optical Physics*, 41:155101, 2008.
- [95] P. D. Lett, K. Helmerson, W. D. Phillips, L. P. Ratliff, S. L. Rolston, and M. E. Wagshul. Spectroscopy of Na_2 by photoassociation of laser-cooled Na. *Physical Review Letters*, 71:2200–2203, 1993.
- [96] H. Wang, P. L. Gould, and W. C. Stwalley. Photoassociative spectroscopy of ultracold ${}^{39}\text{K}$ atoms in a high-density vapor-cell magneto-optical trap. *Physical Review A*, 53:R1216–R1219, 1996.
- [97] U. Schlöder, C. Silber, and C. Zimmermann. Photoassociation of heteronuclear lithium. *Applied Physics B*, 73:801–805, 2001.
- [98] M. Pichler, W. C. Stwalley, and O. Dulieu. Perturbation effects in photoassociation spectra of ultracold Cs_2 . *Journal of Physics B: Atomic, Molecular and Optical Physics*, 39:S981, 2006.
- [99] S. Dutta, J. Lorenz, A. Altaf, D. S. Elliott, and Y. P. Chen. Photoassociation of ultracold LiRb * molecules: Observation of high efficiency and unitarity-limited rate saturation. *Physical Review A*, 89:020702, 2014.
- [100] H. Wang and W. C. Stwalley. Ultracold photoassociative spectroscopy of heteronuclear alkali-metal diatomic molecules. *The Journal of Chemical Physics*, 108:5767–5771, 1998.
- [101] R. J. LeRoy and R. B. Bernstein. Dissociation energy and long-range potential of diatomic molecules from vibrational spacings of higher levels. *The Journal of Chemical Physics*, 52:3869–3879, 1970.
- [102] B. Bussery, Y. Achkar, and M. Aubert-Frécon. Long-range molecular states dissociating to the three or four lowest asymptotes for the ten heteronuclear diatomic alkali molecules. *Chemical Physics*, 116:319 – 338, 1987.

- [103] M. Marinescu and H. R. Sadeghpour. Long-range potentials for two-species alkali-metal atoms. *Physical Review A*, 59:390–404, 1999.
- [104] R. J. LeRoy. Long-range potential coefficients from RKR turning points: C_6 and C_8 for $B(3\Pi_{\text{Ou}}^+)$ -state Cl_2 , Br_2 , and I_2 . *Canadian Journal of Physics*, 52:246–256, 1974.
- [105] D. Comparat. Improved LeRoy-Bernstein near-dissociation expansion formula, and prospect for photoassociation spectroscopy. *The Journal of Chemical Physics*, 120:1318–1329, 2004.
- [106] J. P. Woerdman. A note on the transition dipole moment of alkali dimers. *The Journal of Chemical Physics*, 75:5577–5578, 1981.
- [107] C. J. Sansonetti, C. E. Simien, J. D. Gillaspy, J. N. Tan, S. M. Brewer, R. C. Brown, S. Wu, and J. V. Porto. Absolute transition frequencies and quantum interference in a frequency comb based measurement of the ${}^{6,7}\text{Li}$ D lines. *Physical Review Letters*, 107:023001, 2011.
- [108] H. A. Kramers. Zur struktur der multiplett-s-zustände in zweiatomigen molekülen. i. *Zeitschrift für Physik*, 53:422–428, 1929.
- [109] R. Schlapp. Fine structure in the ${}^3\Sigma$ ground state of the oxygen molecule, and the rotational intensity distribution in the atmospheric oxygen band. *Phys. Rev.*, 51:342–345, 1937.
- [110] C. Long and D. R. Kearns. Selection rules for the intermolecular enhancement of spin forbidden transitions in molecular oxygen. *The Journal of Chemical Physics*, 59:5729–5736, 1973.
- [111] J. L. Bohn and P. S. Julienne. Semianalytic theory of laser-assisted resonant cold collisions. *Physical Review A*, 60:414–425, 1999.
- [112] P. Pellegrini and R. Côté. Probing the unitarity limit at low laser intensities. *New Journal of Physics*, 11:055047, 2009.
- [113] R. Wester, S. D. Kraft, M. Mudrich, M. U. Staudt, J. Lange, N. Vanhaecke, O. Dulieu, and M. Weidemüller. Photoassociation inside an optical dipole trap: absolute rate coefficients and franck–condon factors. *Applied Physics B*, 79:993–999, 2004.
- [114] H. R. Thorsheim, J. Weiner, and P. S. Julienne. Laser-induced photoassociation of ultracold sodium atoms. *Physical Review Letters*, 58:2420–2423, 1987.
- [115] C. W. Johnston and J. J. A. M. van der Mullen. A scaling rule for molecular electronic transition dipole moments: Application to asymptotically allowed and forbidden transitions. *The Journal of Chemical Physics*, 119:2057–2061, 2003.

- [116] H. Salami, A. J. Ross, P. Crozet, W. Jastrzebski, P. Kowalczyk, and R. J. Le Roy. A full analytic potential energy curve for the $a^3\Sigma^+$ state of KLi from a limited vibrational data set. *The Journal of Chemical Physics*, 126:194313, 2007.
- [117] M. Ivanova, A. Stein, A. Pashov, H. Knöckel, and E. Tiemann. The $X^1\Sigma^+$ state of LiRb studied by fourier-transform spectroscopy. *The Journal of Chemical Physics*, 134:024321, 2011.
- [118] P. Staanum, A. Pashov, H. Knöckel, and E. Tiemann. $X^1\Sigma^+$ and $a^3\Sigma^+$ states of LiCs studied by fourier-transform spectroscopy. *Physical Review A*, 75:042513, 2007.
- [119] E. J. Breford and F. Engelke. Laser-induced molecular fluorescence in supersonic nozzle beams: Applications to the NaK D $^1\Pi \rightarrow X^1\Sigma^+$ and D $^1\Pi \rightarrow a^3\Sigma^+$ systems. *Chemical Physics Letters*, 53:282 – 287, 1978.
- [120] O. Docenko, M. Tamanis, R. Ferber, H. Knöckel, and E. Tiemann. Singlet and triplet potentials of the ground-state atom pair Rb + Cs studied by fourier-transform spectroscopy. *Physical Review A*, 83:052519, 2011.
- [121] O. Docenko, M. Tamanis, J. Zaharova, R. Ferber, A. Pashov, H. Knöckel, and E. Tiemann. The coupling of the $X^1\Sigma^+$ and $a^3\Sigma^+$ states of the atom pair Na + Cs and modelling cold collisions. *Journal of Physics B: Atomic, Molecular and Optical Physics*, 39:S929, 2006.
- [122] D. Wang, E. E. Eyler, P. L. Gould, and W. C. Stwalley. State-selective detection of near-dissociation ultracold KRb $X^1\Sigma^+$ and $a^3\Sigma^+$ molecules. *Physical Review A*, 72:032502, 2005.
- [123] R. Ferber, I. Klincare, O. Nikolayeva, M. Tamanis, H. Knöckel, E. Tiemann, and A. Pashov. $X^1\Sigma^+$ and $a^3\Sigma^+$ states of the atom pair K + Cs studied by fourier-transform spectroscopy. *Physical Review A*, 80:062501, 2009.
- [124] A. J. Kerman, J. M. Sage, S. Sainis, T. Bergeman, and D. DeMille. Production and state-selective detection of ultracold RbCs molecules. *Physical Review Letters*, 92:153001, 2004.
- [125] T. Bergeman, A. J. Kerman, J. Sage, S. Sainis, and D. DeMille. Prospects for production of ultracold RbCs molecules. *The European Physical Journal D - Atomic, Molecular, Optical and Plasma Physics*, 31:179–188, 2004.
- [126] M. V. Pack, R. M. Camacho, and J. C. Howell. Electromagnetically induced transparency line shapes for large probe fields and optically thick media. *Physical Review A*, 76:013801, 2007.
- [127] M. Lemeshko, R. V. Krems, and H. Weimer. Nonadiabatic preparation of spin crystals with ultracold polar molecules. *Physical Review Letters*, 109:035301, 2012.

- [128] S. A. Will, J. W. Park, Z. Z. Yan, H. Loh, and M. W. Zwierlein. Coherent microwave control of ultracold $^{23}\text{Na}^{40}\text{K}$ molecules. *Physical Review Letters*, 116:225306, 2016.
- [129] S. Ospelkaus, K.-K. Ni, G. Quéméner, B. Neyenhuis, D. Wang, M. H. G. de Miranda, J. L. Bohn, J. Ye, and D. S. Jin. Controlling the hyperfine state of rovibronic ground-state polar molecules. *Physical Review Letters*, 104:030402, 2010.
- [130] C. D. Bruzewicz, M. Gustavsson, T. Shimasaki, and D. DeMille. Continuous formation of vibronic ground state RbCs molecules via photoassociation. *New Journal of Physics*, 16:023018, 2014.
- [131] J. Deiglmayr, A. Grochola, M. Repp, K. Mörlbauer, C. Glück, J. Lange, O. Dulieu, R. Wester, and M. Weidemüller. Formation of ultracold polar molecules in the rovibrational ground state. *Physical Review Letters*, 101:133004, 2008.
- [132] P. Zabawa, A. Wakim, M. Haruza, and N. P. Bigelow. Formation of ultracold NaCs molecules via coupled photoassociation channels. *Physical Review A*, 84:061401, 2011.
- [133] J. Banerjee, D. Rahmlow, R. Carollo, M. Bellos, E. E. Eyler, P. L. Gould, and W. C. Stwalley. Direct photoassociative formation of ultracold KRb molecules in the lowest vibrational levels of the electronic ground state. *Physical Review A*, 86:053428, 2012.
- [134] C. Gabbanini and O. Dulieu. Formation of ultracold metastable RbCs molecules by short-range photoassociation. *Physical Chemistry Chemical Physics*, 13:18905–18909, 2011.
- [135] K. Aikawa, D. Akamatsu, M. Hayashi, K. Oasa, J. Kobayashi, P. Naidon, T. Kishimoto, M. Ueda, and S. Inouye. Coherent transfer of photoassociated molecules into the rovibrational ground state. *Physical Review Letters*, 105:203001, 2010.
- [136] C.-H. Wu, J. W. Park, P. Ahmadi, S. Will, and M. W. Zwierlein. Ultracold fermionic feshbach molecules of $^{23}\text{Na}^{40}\text{K}$. *Physical Review Letters*, 109:085301, 2012.
- [137] M. W. Zwierlein, C. A. Stan, C. H. Schunck, S. M. F. Raupach, S. Gupta, Z. Hadzibabic, and W. Ketterle. Observation of bose-einstein condensation of molecules. *Physical Review Letters*, 91:250401, 2003.
- [138] A. Ciamei, A. Bayerle, B. Pasquiou, and F. Schreck. Observation of bose-enhanced photoassociation products. *Europhysics Letters*, 119:46001, 2017.

- [139] T. Rom, T. Best, O. Mandel, A. Widera, M. Greiner, T. W. Hänsch, and I. Bloch. State selective production of molecules in optical lattices. *Physical Review Letters*, 93:073002, 2004.
- [140] M. Fleischhauer, A. Imamoglu, and J. P. Marangos. Electromagnetically induced transparency: Optics in coherent media. *Reviews of Modern Physics*, 77:633–673, 2005.
- [141] H. R. Gray, R. M. Whitley, and C. R. Stroud. Coherent trapping of atomic populations. *Optics Letters*, 3:218–220, 1978.
- [142] T. Köhler, K. Góral, and P. S. Julienne. Production of cold molecules via magnetically tunable feshbach resonances. *Reviews of Modern Physics*, 78:1311–1361, 2006.
- [143] M. Gacesa, P. Pellegrini, and R. Côté. Feshbach resonances in ultracold $^{6,7}\text{Li}$ + ^{23}Na atomic mixtures. *Physical Review A*, 78:010701, 2008.
- [144] B. S. Williams. Terahertz quantum-cascade lasers. *Nature Photonics*, 1:517–525, 2007.
- [145] R. Grimm, M. Weidemüller, and Y. B. Ovchinnikov. Optical dipole traps for neutral atoms. *Advances In Atomic, Molecular, and Optical Physics*, 42:95 – 170, 2000.
- [146] R.W. Nicholls. Franck-condon factor sum rules for transitions involving bound and unbound states. *Journal of Quantitative Spectroscopy and Radiative Transfer*, 45:261 – 265, 1991.
- [147] T. Mukaiyama, J. R. Abo-Shaeer, K. Xu, J. K. Chin, and W. Ketterle. Dissociation and decay of ultracold sodium molecules. *Physical Review Letters*, 92:180402, 2004.
- [148] S. Dürr, T. Volz, and G. Rempe. Dissociation of ultracold molecules with feshbach resonances. *Physical Review A*, 70:031601, 2004.
- [149] R. Côté and A. Dalgarno. Ultracold atom-ion collisions. *Physical Review A*, 62:012709, 2000.
- [150] J. Deiglmayr, M. Repp, R. Wester, O. Dulieu, and M. Weidemüller. Inelastic collisions of ultracold polar LiCs molecules with caesium atoms in an optical dipole trap. *Physical Chemistry Chemical Physics*, 13:19101–19105, 2011.
- [151] T. T. Wang, M.-S. Heo, T. M. Rvachov, D. A. Cotta, and W. Ketterle. Deviation from universality in collisions of ultracold $^6\text{Li}_2$ molecules. *Physical Review Letters*, 110:173203, 2013.
- [152] W. C. Campbell, T. V. Tscherbul, H.-I. Lu, E. Tsikata, R. V. Krems, and J. M. Doyle. Mechanism of collisional spin relaxation in $^3\Sigma$ molecules. *Physical Review Letters*, 102:013003, 2009.

- [153] T. V. Tscherbul and R. V. Krems. Controlling electronic spin relaxation of cold molecules with electric fields. *Physical Review Letters*, 97:083201, 2006.
- [154] A. Micheli, Z. Idziaszek, G. Pupillo, M. A. Baranov, P. Zoller, and P. S. Julienne. Universal rates for reactive ultracold polar molecules in reduced dimensions. *Physical Review Letters*, 105:073202, 2010.
- [155] J. J. Zirbel, K.-K. Ni, S. Ospelkaus, T. L. Nicholson, M. L. Olsen, P. S. Julienne, C. E. Wieman, J. Ye, and D. S. Jin. Heteronuclear molecules in an optical dipole trap. *Physical Review A*, 78:013416, 2008.
- [156] T. Takekoshi, M. Debatin, R. Rameshan, F. Ferlaino, R. Grimm, H.-C. Nägerl, C. R. Le Sueur, J. M. Hutson, P. S. Julienne, S. Kotochigova, and E. Tiemann. Towards the production of ultracold ground-state RbCs molecules: Feshbach resonances, weakly bound states, and the coupled-channel model. *Physical Review A*, 85:032506, 2012.
- [157] F. Wang, X. He, X. Li, B. Zhu, J. Chen, and D. Wang. Formation of ultracold narb feshbach molecules. *New Journal of Physics*, 17:035003, 2015.
- [158] W. C. Stwalley, J. Banerjee, M. Bellos, R. Carollo, M. Recore, and M. Mastrianni. Resonant coupling in the heteronuclear alkali dimers for direct photoassociative formation of X(0,0) ultracold molecules. *The Journal of Physical Chemistry A*, 114:81–86, 2010.
- [159] J. Ulmanis, J. Deiglmayr, M. Repp, R. Wester, and M. Weidemüller. Ultracold molecules formed by photoassociation: Heteronuclear dimers, inelastic collisions, and interactions with ultrashort laser pulses. *Chemical Reviews*, 112:4890–4927, 2012.
- [160] D. Wang, B. Neyenhuis, M. H. G. de Miranda, K.-K. Ni, S. Ospelkaus, D. S. Jin, and J. Ye. Direct absorption imaging of ultracold polar molecules. *Physical Review A*, 81:061404, 2010.
- [161] W. S. Bakr, J. I. Gillen, A. Peng, S. Fölling, and M. Greiner. A quantum gas microscope for detecting single atoms in a hubbard-regime optical lattice. *Nature*, 462:74–77, 2009.
- [162] L. W. Cheuk, M. A. Nichols, M. Okan, T. Gersdorf, V. V. Ramasesh, W. S. Bakr, T. Lompe, and M. W. Zwierlein. Quantum-gas microscope for fermionic atoms. *Physical Review Letters*, 114:193001, 2015.
- [163] J. Deiglmayr, M. Aymar, R. Wester, M. Weidemüller, and O. Dulieu. Calculations of static dipole polarizabilities of alkali dimers: Prospects for alignment of ultracold molecules. *The Journal of Chemical Physics*, 129:064309, 2008.